Radiation Effects in Zirconium Alloys

Fabien Onimus, Sylvie Doriot, J.-L. Béchade

F. Onimus, S. Doriot, J.L. Béchade (2020) Radiation effects in zirconium alloys, Chapter 3.01 in: Comprehensive Nuclear Materials, Elsevier, 2nd Ed., R. Konings, R. Stoller Eds, Vol. 3, pp. 1-56.

5.01 Radiation Effects in Zirconium Alloys

F. Onimus, S. Doriot and J.L. Béchade

Commissariat à l'Energie Atomique, Gif-sur-Yvette, France

Abstract

In this chapter, the effects of neutron irradiation on zirconium alloys are described. Irradiation effects on the microstructure are first discussed, describing damage creation, point-defect evolution leading to loop formation and also secondary-phase evolution and alloying elements redistribution under irradiation. Then, in the second part, irradiation effects on postirradiation mechanical behavior and deformation mechanisms, especially during tensile test and also after postirradiation thermal treatment or postirradiation creep tests, are given. Finally, the in-reactor deformation behavior, growth, and irradiation creep, as well as the related deformation mechanisms, are analyzed.

Keywords

Anisotropy

Creep

Damage

Dislocation

Hardening

Irradiation

Irradiation growth

Irradiation loops

Mechanical properties

Point defects

Precipitation

Zr alloys

Abbreviations

BWR Boiling-water reactor

CANDU Canadian deuterium uranium

Dpa displacement per atom

DAD Diffusion anisotropy difference

EAM Embedded atom method

EID Elastic interaction difference

FP-LMTO Full-potential linear muffin-tin orbital

GGA Generalized gradient approximation

hcp Hexagonal close-packed

HVEM High-voltage electron microscope

LDA Local density approximation

MB Many body

MD Molecular dynamics

NRT Norgett–Robinson–Torrens

PKA Primary knocked-on atom

PHWR Pressurized Heavy Water Moderated Reactor

PWR Pressurized water reactor

RBMK Reactor Bolshoy Moshchnosty Kanalny

RXA Recrystallization annealing

SANS Small-angle neutron scattering

SIA Self interstitial atom

SIPA Stress-induced preferential absorption

SIPA-AD Stress preferential induced nucleation-anisotropic diffusion

SIPN Stress preferential induced nucleation

SRA Stress-relieving annealing

TEM Transmission electron microscopy

T_m Melting temperature

UTS Ultimate tensile strength

VVER Vodo-Vodianoï Energuetitcheski Reaktor

YS Yield stress

5.01.1 Use of Zirconium Alloys for Nuclear Applications

5.01.1.1 Reactor components made of zirconium alloys and functions

Zirconium alloys have been chosen as fuel cladding and structural components for light and heavy water nuclear reactor cores mainly because of their low capture cross section to thermal neutrons and their good corrosion resistance. They are now used in almost every thermal neutron reactors using light or heavy water which represent more than 95% of the nuclear reactors worldwide[1]. Most of the elements of PWR, VVER and BWR fuel assemblies (or fuel bundles) are made of zirconium alloys. Indeed, in the case of PWR, the cladding tubes, the guide tubes (or guide thimbles) and the grids are made of zirconium alloys. For VVER reactor, which is an eastern design of pressurized water reactor, the structural components of the fuel assembly (guide thimbles, central tube, rigid angles) and the fuel rod claddings are made of zirconium alloys. In the case of BWR, the cladding tubes and channel boxes are made of zirconium alloys. In the PHWR (Pressurized Heavy Water moderated Reactor), which are CANDU type reactors, originally designed in Canada, zirconium alloys are used for fuel cladding and fuel bundle structures but also for important structural components of the reactor core, especially the pressure tubes and calandria tubes. RBMK type reactors, an early Soviet design, also use zirconium alloys as pressure tube and fuel cladding material.

The main function of the cladding tubes is to contain the radioactive species such as the fuel nuclei and the fission products. A good heat exchange, from the fuel pellet to the coolant, is also required. In the case of PWR, inside the guide tubes, the control rods move to control the chain reaction. As for the grids, they maintain the geometry of the fuel assembly while inducing a turbulent flow in the water thus increasing the heat exchange between the fuel rod and the coolant. The grids also prevent vibration of the fuel rod that could induced abrasion on the cladding tube.
In the case of BWR, the diphasic liquid-vapour water is channeled within the channel box. This box also guides the motion of the control blade to control the chain reaction.

[1] 431 light or heavy water reactors in operation over 448 nuclear reactors in operation worldwide in 2017 (Source IAEA).

Because fuel assembly is consumable, evolutions of the properties of zirconium alloys under irradiation do not limit the lifetime of the reactor, however they may affect the performance of the fuel assembly in normal operating conditions, for instance reducing the burn-up that can be reached by the fuel. Radiation effects are also an issue when the back end cycle of the fuel assembly is considered. Radiation effects may also have some incidence on hypothetical design based accident scenario involving zirconium cladding tube, however, in that situation, this issue is usually considered as second order effect compared to other phenomena, such as the presence of hydrides.

In the case of CANDU type reactors, because the components made of zirconium alloys such as the pressure tubes, are important structural elements of the reactor core, the evolution of the material under irradiation may limit the lifetime of the reactor.

These are the reasons why radiation effects in zirconium alloys have been studied from the early 60's in many countries that started to develop their own nuclear industry. The importance of zirconium alloys in CANDU type reactors also explains the major role played by Canada in this field of research.

5.01.1.2 Reactor grade zirconium alloys

Several zirconium alloys are used for these various applications. Zircaloy-2 (or Zy-2) and Zircaloy-4 (or Zy-4), referred to as Zircaloys, have been used for cladding tubes, respectively for BWR and PWR. Nowadays, advanced alloys, containing niobium without tin, such as M5 and E110, or advanced alloys containing niobium, tin and iron, sometimes referred to as quaternary alloys, such as Zirlo and E635, are used for cladding tubes of PWR and VVER reactors. The chemical compositions of these alloys are given **Table 1**. Concerning BWR cladding tubes, Zircaloy-2 remains the reference material, often used with an inner liner in low alloyed zirconium. These alloys can be found mainly in two different metallurgical states depending on the final heat treatment, which follows the last cold-rolling step: either recrystallization annealing (RXA) or stress-relieving annealing (SRA). In the literature, RXA alloys can also be referred to as fully recrystallized, well annealed or annealed. Whereas SRA alloys may be referred to as CWSR, standing for Cold Worked Stress Relieved, or cold-worked. For pressure tubes of PHWR, an alloy referred to as Zr2.5Nb is used in cold-worked state.

Table 1: Composition of some of the zirconium alloys used in the nuclear industry (in wt% or ppm)

	Sn	Nb	Fe	Cr	Ni	O	S
Zircaloy-2	1.2-1.5	-	0.07-0.2	0.1	0.05	0.12	-
Zircaloy-4	1.2-1.7	-	0.18-0.24	0.1	-	0.1-0.14	-
M5	-	0.8-1.2	<500 ppm	-	-	0.11-0.16	10-35 ppm
E110	-	1	100 ppm	-	-	0.05-0.07	-
Zr2.5Nb	-	2.5-2.7	<650 ppm	-	-	0.12-0.15	-
Zirlo	1	1	0.1	-	-	0.09-0.12	-
E635	1.2	1	0.35	-	-	0.05-0.07	-

In the following, a summary of the understanding of radiation effects in zirconium alloys gathered throughout 60 years of research is presented. Many updates have been made compared to the chapter published in the first edition. Most of the updates concern recent results obtained these past ten years and especially charged particle irradiation, small scale mechanical testing and multi-scale modelling.

5.01.2 Irradiation Damage in Zirconium Alloys

5.01.2.1 Neutron–zirconium interaction

Although zirconium alloys are known to have a low thermal neutron ($E \approx 0.025$ eV) capture cross-section (0.18 barn for zirconium compared to 2.55 barn for iron), under fast neutron ($E > 1$ MeV) irradiation, they are strongly affected, as other metals, by the fast neutron flux. In the case of metallic alloys, the irradiation damage is mainly due to elastic interactions between fast neutrons and atoms of the alloy that displace atoms from their crystallographic sites (depending on the energy of the incoming neutron) and can create point defects without modifications of the

target atom, as opposed to inelastic interactions leading to transmutation, for instance. During the collision between the neutron and the atom, part of the kinetic energy can be transferred to the target atom. The interaction probability is given by the elastic collision differential cross section [1] [2] which depends on both the neutron kinetic energy and the transferred energy. For a typical fast neutron of 1 MeV, the mean transferred energy ($\bar{T}$) of the Zr atom is $\bar{T}$=21.7 keV (taking an atomic mass of 90 for Zr). For low value of the transferred energy, the target atom cannot leave its position in the crystal, leading only to an increase of the atomic vibrational amplitude resulting in simple heating of the crystal. If the transferred energy is higher than a threshold value, the displacement energy (E_d), the knocked-on atom can escape from its lattice site and is called the primary knocked-on atom (PKA). For high transferred energy, as is the case for fast neutron irradiation, the PKA interacts with the other atoms of the alloy along its track. On average, at each atomic collision, half of its current kinetic energy is transferred to the collided atom, since they have equal masses. The collided atoms can then interact with other atoms, thus creating a displacement cascade within the crystal.

5.01.2.2 Displacement energy in zirconium

The displacement energy in zirconium has been measured experimentally using electron irradiations performed at low temperatures (<10 K). The irradiation damage was monitored *in situ* using electrical resistivity changes [3] [4]. The measured minimum displacement threshold energy transferred to the Zr atoms is E_d = 21−24 eV. Measurements of E_d have also been performed using a high-voltage electron microscope (HVEM) to irradiate a Zr thin foil. The values obtained were found to be weakly orientation dependent, between 24 and 27.5 eV, with a mean $\bar{E}_d$ of 24 eV [5].

The displacement energy has also been computed by molecular dynamics (MD) simulations using a many-body (MB) potential based on the Finnis and Sinclair formalism [6]. These authors have found that the displacement energy is significantly anisotropic. Displacement energy was found to be minimum for knocking out in the basal plane, that is, in the $\langle 11\bar{2}0 \rangle$ directions, corresponding to the most favorable direction for replacement collision sequences, and to the direction of development of the basal crowdion. The corresponding displacement energy obtained (E_d = 27.5 eV) is slightly above the experimental values. The value averaged over all the crystallographic directions was found to be 55 eV. The value specified in the norm reference

test standard (Standard E521−89, Annual Book of ASTM Standards, ASTM, Philadelphia, PA, USA) is $\bar{E}_d$=40 eV [7]. This value is close to the spatial means obtained by MD models.

5.01.2.3 Displacement cascades and damage dose measurement

The number of displaced atoms inside the cascade can be simply estimated using the Kinchin−Pease formula [8] or the modified Kinchin−Pease formula from Torrens and Robinson [9] [10] [11]. According to this last model, the number of displaced atoms within the cascade in the case of a 21.7 keV PKA and using a displacement energy of E_d = 40 eV is $n_p = 0.8\bar{T}/(2E_d)$=217 atoms. Because of the large mean free path of fast neutrons (3.8 centimeters for 1 MeV neutrons), it can be considered that only one PKA is created by the incoming neutron going through the Zr cladding used in pressurized water reactors (PWRs) (with a typical thickness of 0.57 mm). Therefore, if the PKA creation rate per unit volume within the cladding is known for a typical fuel assembly in a PWR, the number of displaced atoms per unit volume and per second can be computed. From this value, the overall number of displacements per atom (dpa) and per second can be deduced. A simple calculation can be done by considering a monoenergetic (E = 1 MeV) fast neutron flux of 9.5 × 10^{17} n m^{-2} s^{-1} and a collision cross-section of 6 barns between a 1 MeV neutron and a ^{90}Zr nucleus [1] [2]. The calculation yields to a damage rate of 3.9 dpa per year. This means that each atom of the cladding has been displaced 3.9 times per year on average! This is a striking result since the cladding tube keeps its geometry and its containment property.

The above simple calculation corresponds to 13.0 dpa for a fluence of 10^{26} n/m^2 (E > 1 MeV). The exact calculation must be done by taking into account the PWR neutron spectrum as well as the neutron−atom differential cross section using numerical codes such as SPECTER [12]. Walters et al. [13] have computed the number of dpa corresponding to a fluence of 10^{26} n/m^2 (E > 1 MeV) for zirconium within various types of reactors. It is found that for a cladding tube in a PWR core, a fluence of 10^{26} n/m^2 (E > 1 MeV) yields to 15.43 dpa. Walters et al. [13] also provide the corresponding dpa/fluence values for BWR, which is equal to 16.06 dpa, and for CANDU pressure tube, which is equal to 16.87 dpa. Shishov *et al.* [14] obtained a value of 16.7 dpa for of 10^{26} n m^{-2} (E > 1 MeV) in a PWR, in correct agreement with Walters et al.

Typical fast neutron flux values for PWR range between 6×10^{17} [15] to 10×10^{17} n m^{-2} s^{-1} (E > 1 MeV) [16] depending on the location of the considered fuel rod, its enrichment and its burn-up. Using a value of 9.5×10^{17} n m^{-2} s^{-1} (E > 1 MeV), the typical fluence per year (assuming a full year of operation at full power, which is not usually the case) is 3×10^{25} n m^{-2}, leading to a damage dose of 4.6 dpa per year of operation, using the conversion value provided by Walters et al. [13]. In the case of zirconium alloys, the fast neutron fluence (E> 1 MeV, in $n.m^{-2}$) is usually given rather than the damage dose in dpa. Another unit, the burn-up (BU, in GWd/t), can often be found in the literature for fuel rod cladding tubes. This quantity corresponds to the total energy released per unit mass of heavy elements (U, Pu) in the fuel. According to Shishov et al. [14], one year of operation in a PWR corresponds to a burn-up of 15 GWd/t. From the work of Doriot [15] and Shishov [14] it can be found that the fluence corresponding to 1 GWd/t ranges from 1.7×10^{24} n m^{-2} to 2.0×10^{24}n m^{-2}. Adamson et al. [17] also provide the correspondence between burn-up, fluence and dpa as the following: 50 GWd/t = 10^{26} n/m^2 (E > 1 MeV) = 15.4 dpa, in good agreement with the values stated above. The number of PWR cycles is also often given in the literature as a measure of irradiation dose. However, originally, one PWR cycle lasted approximately one year, but current advanced core managements use 18 months cycle. The duration of the PWR cycle should therefore also be given along with the number of cycles.

The calculation of the number of displacements per atom given above, provides a correct description of the number of displaced atoms during the creation of the cascade (except for the role of replacement sequences). However, it does not consider intracascade elastic recombination that occurs during the cascade relaxation or cooling-down phase [10] [18] [19]. In addition, this approach does not give any information on the form of the remaining damage at the end of the cascade, such as the point-defect clusters that can be created in the cascade.
In order to have a better understanding of the created damage in α-zirconium, several authors have performed Molecular Dynamics (MD) computations also using different types of interatomic potentials. It is shown that, at the end of the cascade creation (<2 ps), the cascade is composed of a core with a high vacancy concentration, and the self-interstitial atoms (SIAs) are concentrated at the cascade periphery [19] [20] [21]. The cascade creation is followed by the athermal cascade relaxation that can last for a few picoseconds. During this phase, most of the displaced atoms quickly reoccupy lattice sites as a result of prompt (less than a lattice vibration

period, 0.1 ps) elastic recombination if a SIA and a vacancy are present at the same time in the elastic recombination volume (with 200 Ω < V_r < 400 Ω, where V_r is the elastic recombination volume and Ω the atomic volume [22]). Wooding *et al.* [21] and Gao *et al.* [7] have shown that at the end of the cascade relaxation the number of surviving point defects is very low, only 20% at 600 K, much lower than the number of Frenkel pairs computed using the NRT model [9]. It is also shown that all the point defects are not free to migrate but that small point-defect clusters are created within the cascade. This clustering is due to short-range diffusion driven by the large elastic interaction among neighboring point defects and small point-defect clusters. In the case of zirconium, large point-defect clusters, up to 24 vacancies and 25 SIAs (at 600 K), can be found at the end of the cascade relaxation (**Figures 1 and 2**) [7].

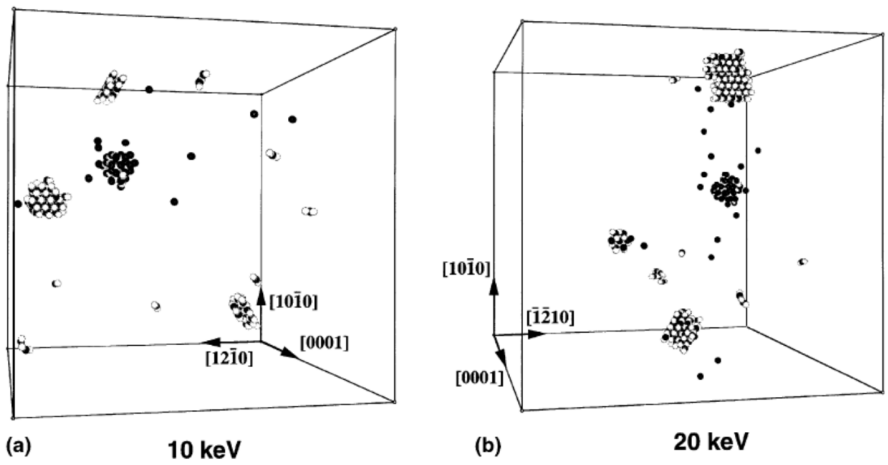

Figure 1: Computer plots showing the final state of damage of: (a) a 10 keV cascade, and (b) a 20 keV cascade at 600 K, where white spheres represent interstitials (SIAs) and dark spheres indicate vacancies.

According to Woo *et al.* [19], the presence of these small point-defect clusters spatially separated from each other, as well as the different concentrations of single vacancies and SIAs, can have a major impact on the subsequent microstructural evolution. This effect is known as the production bias, which has to be considered when solving the rate equations in the mean-field approach of point-defect long-term evolution [19].

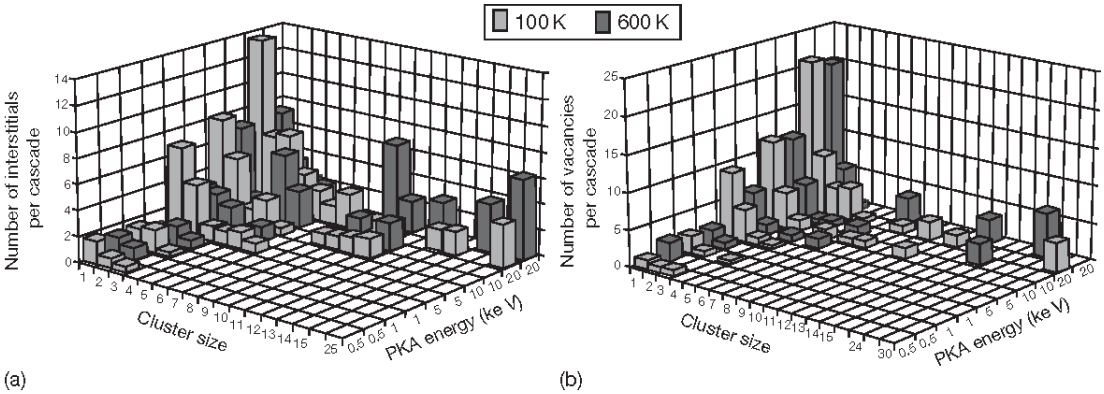

Figure 2 Number of single and clustered (a) interstitials and (b) vacancies per cascade as a function of the PKA energy. Adapted from Gao, F.; Bacon, D. J.; Howe, L. M.; So, C. B. *J. Nucl. Mater*. **2001**, *294*, 288–298

The form of these small clusters is also of major importance since it plays a role on the nucleation of dislocation loops. Wooding *et al.* [21] and Gao *et al.* [7] have shown that the small SIA clusters are in the form of dislocation loops with the Burgers vector $\frac{1}{3}\langle 11\bar{2}0\rangle$. The collapse of the 24-vacancy cluster to a dislocation loop on the prism plane was also found to occur. Voskoboinikov et al. [23] have also conducted MD simulations and found a variety of point defect clusters inside displacement cascades. They confirmed that the majority of SIA clusters are SIA dislocation loops with Burgers vector equal to $\frac{1}{3}\langle 11\bar{2}0\rangle$. Concerning vacancy clusters, they found that the most frequent one has a shape close to a triangular prism, with the triangle bases in the basal plane. They also noticed stacking fault pyramid vacancy clusters with base on the basal plane exhibiting an extrinsic fault in this plane. These types of defects have also been found by other authors [24]. These various defect clusters could play a role on the subsequent evolution of the microstructure, as it will be discussed in the following.

5.01.2.4 Long-Term Evolution of Point Defects under irradiation

After the cascade formation and relaxation, which last for a few picoseconds, the microstructure evolves over a longer time. The evolution of the microstructure is driven by the bulk diffusion of point defects. For a better understanding of the microstructure evolution under irradiation, the

elementary properties of point defects, such as formation energy and migration energy, have first to be examined.

5.01.2.4.1 Vacancy formation and migration energies

Concerning the vacancy, all the atomic positions are equivalent in the lattice and so there is only one vacancy description leading to a unique value for the vacancy formation energy. Due to the rather low α–β phase transformation temperature (863°C for pure zirconium) compared to the high melting temperature (1855°C for pure zirconium), the measurement of vacancy formation and migration energy in the Zr hexagonal close-packed (hcp) phase is difficult. The temperature that can be reached is not high enough to obtain an accurately measurable concentration and mobility of vacancies [25]. Nevertheless, various experimental techniques (**Table 2**), such as positron annihilation spectroscopy or diffusion of radioactive isotopes, have been used in order to measure the vacancy formation and migration energies or the self-diffusion coefficient [25] [26] [27] [28] [29] [30] [31] [32] [33]. The values obtained by the several authors are given in **Table 2**. It is pointed out by Hood [25] that there is large discrepancy among the various results. It is particularly shown that at high temperature, the self-diffusion activation energy is rather low compared to the usual self-diffusion activation energy in other metals [25]. However, as the temperature decreases, the self-diffusion activation energy increases strongly. According to Hood [25], this phenomenon can be explained assuming that at high temperature the vacancy mobility is enhanced by some impurity such as an ultrafast species like iron. At lower temperature, the iron atoms are believed to form small precipitates, explaining that at low temperatures the measured self-diffusion energy is consistent with usual intrinsic self-diffusion of hcp crystals. It is also shown that the self-diffusion anisotropy remains low for normal-purity zirconium, with a slightly higher mobility in the basal plane than along the ⟨ *c*⟩ axis [29] [33] [34]. For high-purity zirconium, with a very low iron content, the anisotropy is reversed, with a higher mobility along the ⟨ *c*⟩ axis than in the basal plane [34].

Table 2: Experimental determination of formation (E_f), migration (E_m) and self diffusion activation (E_a) energies for vacancy (in eV).

Experimental methods	E_f	E_m	E_a	Reference
Semiempirical	1.8–1.9	1.3–1.6	3.3	[25]
Self-diffusion	–	–	1.2–3.5	[25]
Diffusion behavior of various solutes in Zr	1.4–2.1	1.1–1.5	3.2–3.5	[26]
Self-diffusion	–	–	2.85	[27]
Resistivity		0.58		[3]
Positron Annihilation Spectroscopy	>1.5	0.65		[30]

The vacancy formation and migration energies have been computed either by MD methods, where the mean displacement distance versus time allows obtaining the diffusion coefficient, or by static computation of the energy barrier corresponding to the transition between two positions of the vacancy using either empirical interatomic potential [6] [35] [36] [37] [38] [39] [40] [41] or the most recent *ab initio* tools [42] [43] [44] [45]. Since the different sites surrounding the vacancy are not equivalent, due to the non-ideal *c*/*a* ratio, the migration energies are expected to depend on the crystallographic direction, that is, the migration energies in the basal plane (E_m^a) and along the $\langle c \rangle$ direction (E_m^c) are different. New ab-initio computations [46] have confirmed these values. The results are given in **Table 3**.

Table 3: Computation determination of formation (E_f), migration (E_m), and self-diffusion activation (E_{act}) energies for vacancy (in eV).

Computation methods	E_f	E_m^a (basal)	E_m^c (non-basal)	E_{act}	Reference
Pair potential	1.59	1.21	1.10		[35]
Finnis–Sinclair MB potential	1.79	0.93	0.93		[40]
Finnis–Sinclair MB potential	1.79	–	–	–	[6]
Finnis–Sinclair MB potential	1.79	0.84	0.88	2.64	[41]
EAM potential	1.74	0.57	0.59	2.32	[38]
Ab initio FP-LMTO	2.07	–	–	–	[37]
Ab initio GGA	1.86	–	–	–	[43] [44]
Ab initio GGA	2.17	0.51	0.67	2.76	[45]
Ab initio LDA	2.29	0.23	0.43	2.78	[45]
Ab initio GGA		0.538	0.629		[46]
Ab initio GGA	2.07	0.54	0.65		[47]

MB: many body; EAM: embedded atom method; FP-LMTO: full-potential linear Muffin-Tin orbital; GGA: generalized gradient approximation; LDA: local density approximation.

The atomistic calculations are in agreement with the positron annihilation spectroscopy measurement but are in disagreement with the direct measurements of self-diffusion in hcp zirconium [27]. As discussed by Hood [25], and recently modeled by several authors [48] [49], this phenomenon is attributed to the enhanced diffusion due to coupling with the ultrafast diffusion of iron.

5.01.2.4.2 SIA structure and formation energies

In the case of SIAs, the insertion of an additional atom in the crystal lattice leads to a large distortion of the lattice. Therefore, only a limited number of configurations are possible. The geometrical description of all the interstitial configuration sites has been proposed for titanium by Johnson and Beeler [50] and is generally adopted by the scientific community for other hcp structures (**Figure 3**).

- T is the simplest tetrahedral site, and O is the octahedral one, with, respectively, 4 and 6 coordination numbers.
- BT and BO are similar sites projected to the basal plane with three nearest neighbors, but with different numbers of second neighbors.
- BC is the crowdion extended defect located in the middle of a segment linking two basal atoms.
- C is the interstitial atom located between two adjacent atoms of two adjacent basal planes in the $\langle 20\bar{2}3 \rangle$ direction. This direction is not a close-packed direction, and allows easier insertion of the SIA.
- S is the split dumbbell position in the $\langle c \rangle$ direction and BS is the split dumbbell in the basal plane.

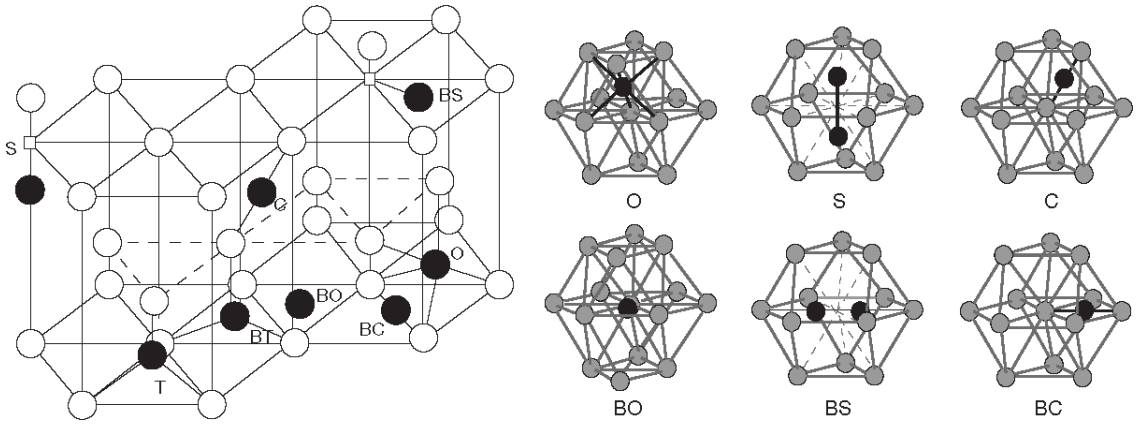

Figure 3 Interstitial sites configuration: (a) static localizations and (b) relaxed configurations. (adapted from Bacon, D. J. *J. Nucl. Mater.* **1993**, *206*, 249–265) (adapted from Willaime, F. *J. Nucl. Mater.* **2003**, *323*, 205–212)

Table 4: Computation of SIAs formation (E_f) and migration (E_m) energies in Zr by *ab initio*, MD, or MS (molecular statics) (in eV).

Method	E_f						E_m		Reference
	O	BO	BS/BC	C	S	T	E_m^a	E_m^c	
Pair potential	–	3.83	–	4.01	–	–	BO: 0.8	BO: 0.49	[35]
							C: 0.49	C: 0.29	[35]
EAM potential	2.8	2.63	2.5	2.78	3.04	_	0.05	0.14	[38]
Finnis-Sinclair MB potential	–	3.97	3.76	3.97	4.32	_	–	–	[6]
Finnis–Sinclair MB potential	–	–	–	–	–	–	0.06	0.15	[40]
Ab initio GGA	2.84	2.88	2.95	3.08	3.01	4.03	–	–	[43] [44]
Ab initio LDA	2.79	2.78	2.90	3.07	2.80	–	–	–	[42]
Ab initio GGA	3.04	3.14	3.39	3.52	3.28	–	–	–	[42]
Finnis–Sinclair MB potential	4.13	3.97	3.75	3.96	3.77	3.98	–	–	[34] [41]

MB: many body; EAM: embedded atom method; FP-LMTO: full-potential linear Muffin-Tin orbital; GGA: generalized gradient approximation; LDA: local density approximation.

The only way to have access to the SIA formation energy is from atomistic computations taking into account the different configurations of the SIA given previously. In their early work on titanium, Johnson and Beeler [50] found that the most stable SIA configuration was the basal-octahedral site (BO). Several other sites were also found to be metastable, like asymmetric variants of the T and C sites. As reviewed by Willaime [42], the relative stabilities of the various SIA configurations were observed to depend strongly on the interatomic potential used (**Table 4**). Recently, *ab-initio* computations [51] have found four other configurations with lower symmetry (referred to as BC', C', PS and P2S). The formation energy of some of these new configurations appear to be lower than that of the more symmetric configurations. These new configurations must therefore be taken into account when assessing the anisotropic mobility of SIAs.

5.01.2.4.3 SIA migration energies

The mobility of SIAs can be estimated experimentally using electron irradiation at very low temperatures (4.2 K), followed by a heat treatment. During the recovery, the electrical resistivity is measured. The main recovery process was found around 100–120 K and analysis of the kinetics gives the SIA migration energy of $E_m \approx 0.26$ eV [3].

Atomistic computations have also brought results (**Table 4**) concerning the SIA migration energy. Several authors [6] [35] [36] [37] [38] [40] [41] [42] [43] [44] have found that the mobility of SIAs is anisotropic, with low migration activation energy for the basal plane mobility ($E_m^a \approx 0.06$ eV) and a higher migration activation energy in the $\langle c \rangle$ direction ($E_m^c \approx 0.15$ eV). In the temperature range of interest for the power reactors ($T \approx 600$ K), the diffusion coefficients obtained are the following: $D_i^a = 8\times10^{-9}$ m^{2}s^{-1} (in the basal plane) and $D_i^c = 10^{-9}$ m^{2}s^{-1} (along the $\langle c \rangle$ direction) [40]. These authors have also shown that the anisotropy depends on the temperature. Computing the effective diffusion rate of SIAs in all directions, taking into account the multiplicity of the jump configurations for each type of migration, Woo and co-workers [41] [52] have obtained the anisotropy for self-interstitial diffusion as a function of temperature. It is shown that the SIA mobility is higher in the basal plane than along the $\langle c \rangle$ axis and that the anisotropy decreases when the temperature increases.

However, recent *ab initio* computations have come to a very different conclusion. Indeed, by using density functional theory (DFT) and Nudged Elastic Band (NEB) techniques, Samolyuk et al. [46] computed all the possible migration energy barriers from one site to another site. Then, by using kinetic Monte-Carlo, they found that both vacancies and interstitials exhibit anisotropic diffusion (more rapid in the basal plane than along the <c> axis for both point defects). Surprisingly, the diffusion anisotropy is higher for vacancies than SIAs for temperatures ranging from 200 K up to 900 K, raising doubts on the earlier results concerning anisotropic diffusion of point defects in zirconium. These authors thus suggest that the fast 1D mobility of small SIA clusters along the <a> directions of the HCP lattice could play a significant role on the microstructure evolution in the same way as it was thought previously for the anisotropic diffusion of SIA.

Nevertheless, in their analysis Samolyuk et al. [46] considered that all sites are populated by vacancies with the same probability, which is not the case, as discussed by Christensen et al. [24]. This assumption leads to an over-estimation of the probability of vacancies jumps along the <c>-axis. Christensen et al. [53], using a new EAM potential fitted on *ab-initio* computations, have been able to evaluate the SIA and vacancy diffusion anisotropy. The simulations show that vacancy diffusion is anisotropic, but to a lesser extent than what was found by Samolyuk et al. [46], the diffusion being more rapid in the basal plane than along the <c> axis. It is also shown that interstitial diffusion occurs almost exclusively in the basal plane, for an unstrained crystal. Suggesting a higher anisotropic diffusion of SIAs than vacancies. This anisotropic diffusion tends to decrease as the temperature increases. The simulations also show a strong effect of the local strain on the anisotropic diffusion of point defects. This effect of local strain could have a strong influence on the evolution of point defects under irradiation.

5.01.2.4.4 Evolution of point defects: Impact of the anisotropic diffusion of SIAs

In zirconium alloys, as in other metals, under irradiation both vacancies and SIAs (Frenkel pairs) are created within the cascades leading to an increase of the point-defect concentration with the irradiation dose. However, even at cryogenic temperatures, the Frenkel pair concentration saturates at values about 1% due to the mutual recombination of vacancies and SIAs [54]. The recombination volume has a size of approximately 100 atomic volumes. At higher temperatures, point defects migrate and can therefore disappear because of a large variety of defects/defects

reactions. Three major mechanisms contribute to defect elimination: vacancy–SIA recombination, point-defect elimination on defect sinks (dislocation, grain boundaries, free surface, etc.), and agglomeration in the form of vacancy dislocation loops and interstitial dislocation loops. It has to be noted that, because of the rapid migration of SIAs towards sinks compared to the slow migration of vacancies, at steady state the vacancy concentration is several orders of magnitude higher than the SIA concentration. Although the creation rate of SIAs and vacancies are equal in the cascade (neglecting the intra-cascade clustering that can induce a production bias effect), the rate of disappearance of SIA is higher (because of higher mobility) than the rate of disappearance of vacancies, thus leading to a higher vacancy concentration than SIAs at steady state.

Because of the elimination of point defects on point-defect clusters, the clusters can grow under irradiation depending on their relative capture efficiency. In the case of cubic metals, since the relaxation volume of SIAs is usually much larger than that of vacancies, edge dislocations eliminate SIAs with a higher efficiency than vacancies (positive bias toward SIAs). Assuming an isotropic diffusion of point defects, this phenomenon leads to a preferred absorption of SIAs by dislocations, provided that there is another type of sink which absorbs more vacancies than interstitials. Because of this preferential absorption of SIAs, the interstitial loops tend to grow under irradiation and the vacancy loops tend to shrink. This explains that in “usual” cubic metals, only interstitial loops are formed (such as Frank loops in austenitic stainless steels) and vacancies clustering create cavities.

However, in hcp zirconium, the point-defect diffusion is usually considered to be anisotropic although there is little experimental evidence of this phenomenon. From the experimental results, it is suggested that vacancy migration is only slightly anisotropic but the SIA migration is suggested to be significantly anisotropic, as shown by early atomistic computations [6] [35] [36] [37] [38] [40] [41] [42] [43] [44]. This diffusional anisotropy difference (DAD) has a strong impact on capture efficiency of point defects by sinks [55]. Assuming SIAs to have a higher mobility in the basal plane than along the $\langle c \rangle$ axis and that the vacancies have an isotropic diffusional behavior, it can be seen that grain boundaries perpendicular to the basal plane absorb more SIAs than vacancies. On the other hand, grain boundaries parallel to the basal plane absorb more vacancies than SIAs. Similarly, a line dislocation parallel to the $\langle c \rangle$ axis absorbs more SIAs than vacancies and a line dislocation in the basal plane absorbs more vacancies than SIAs.

As discussed by Woo [55], this geometrical effect due to the DAD can overwhelm the conventional bias caused by the point-defect/sink elastic interaction difference (EID). Thus, contrary to the implications of the conventional rate theory, edge dislocations in α-zirconium are not necessarily biased toward SIAs, and grain boundaries are no longer neutral sinks. As will be described in the following, this phenomenon can explain some anomalous irradiation-induced microstructural features as well as the growth phenomenon of zirconium alloys.
However, recent ab initio computations [46] have shown an inverse difference of anisotropy, raising doubts concerning the DAD theory. To reconcile experimental results with these numerical simulation results, some authors [56] have speculated that the 1D fast migration of small SIA clusters formed inside the cascades could play an important role in the microstructure evolution, replacing the role of the anisotropic diffusion of single SIAs.

5.01.3 Point-Defect Clusters in Zirconium Alloys

In the case of zirconium alloys, many authors have studied the postirradiation microstructure by using transmission electron microscopy (TEM). In 1979, an international 'round robin' was undertaken consisting of TEM observations of neutron-irradiated recrystallized zirconium alloys [57] in order to determine the nature of the point-defect clusters. A compilation of observations is given by Griffiths [58]. It has been now proved by numerous authors that in zirconium alloys mainly dislocation loops with $\langle a \rangle$ Burgers vector can be found. Only for high fluence, the $\langle c \rangle$ component dislocation loops appear. Cavities are observed only in very specific cases.

5.01.3.1 $\langle a \rangle$ Dislocation loops under neutron irradiation

It is now clearly established [57] [58] [59] [60] [61] [62] [63] [64] [65] [66] [67] that for commercial neutron-irradiated zirconium alloys (e.g., annealed Zircaloy-2 described by Northwood *et al.* [57]) at temperatures between 250 and 400°C and for irradiation dose lower than 5×10^{25} n m^{-2}, the point-defect clusters that can be observed by TEM (>2 nm) consist of perfect dislocation loops, either of vacancy or interstitial nature, with Burgers vector $\langle a \rangle$ ($\frac{1}{3}\langle 11\bar{2}0 \rangle$), situated in the prismatic planes with typical diameter from 5 to 20 nm, depending on the irradiation temperature (**Figures 4** and **5**). For a neutron fluence higher than 10^{24} n m^{-2}, these loops are found in very high density, typically between 5×10^{21} and 5×10^{22} m^{-3}, depending on

the irradiation temperature (**Figure 6**) [57] [63]. The three ⟨ *a*⟩ Burgers vectors are equally represented.

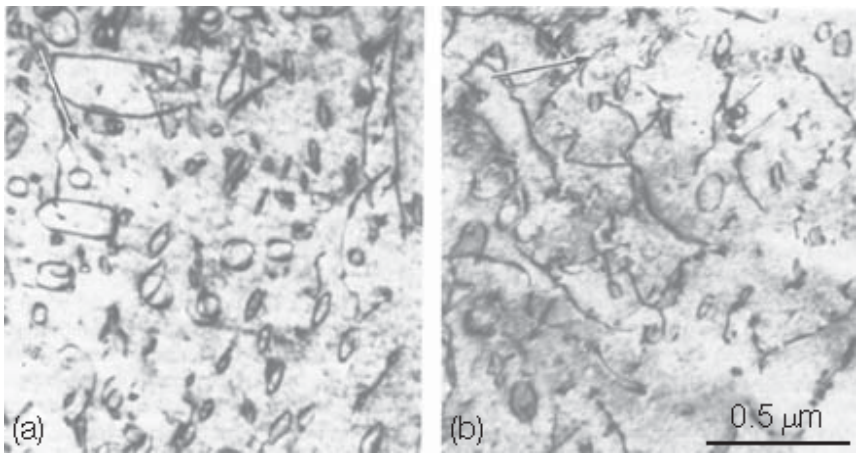

Figure 4 ⟨ *a*⟩ dislocation loops obtained in EBR-II at 700 K: (a) 1.1 × 10^{25} n m^{-2} and (b) 1.5 × 10^{26} n m^{-2}. Diffracting vector $\underline{g} = 10\bar{1}1$ and beam direction $\underline{B} = [0\bar{1}11]$, Griffiths, M. *J. Nucl. Mater*. **1988**, *159*, 190–218.

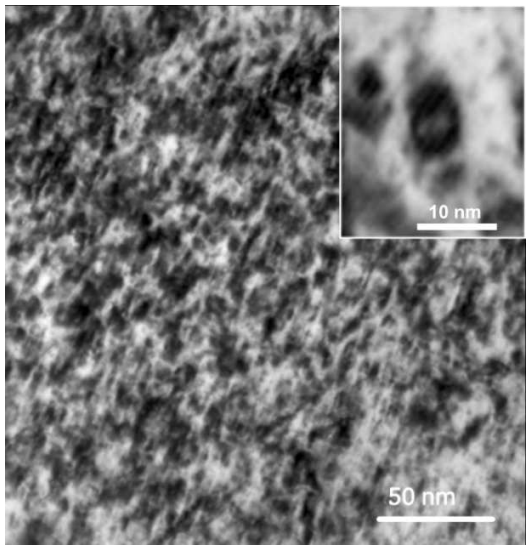

Figure 5 Typical ⟨ *a*⟩ loop microstructure observed on recrystallized Zy-4 irradiated at 280 °C in Siloé up to a fluence of 6 × 10^{24} n m^{-2}. Encapsulated is shown an isolated <a>-loop observed on a thin area of the TEM foil.

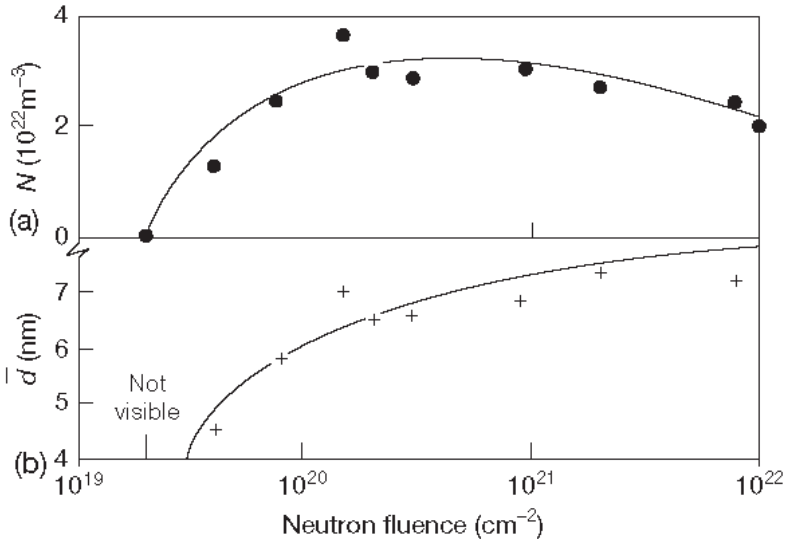

Figure 6 Evolution with dose of the dislocation loops characteristics: (a) density and (b) mean size of defects for Zy-2 irradiated at 300 °C. Adapted from Northwood, D. O. *Atomic Energy Rev*. **1977**, *15*, 547–610.

The proportion of vacancy loops to interstitial loops depends on the irradiation temperature. Indeed, it is observed that for an irradiation temperature of 350°C approximately 50% of observed loops are vacancy loops in crystal-bar zirconium [62], whereas for an irradiation temperature of 400 °C, 70% of loops are vacancy loops [57] [58] [62]. For irradiation temperatures equal or below 300 °C, it is usually very difficult to determine the nature of the loops owing to the too small loop size [62].

The loop habit plane is close to the prismatic plane, but accurate determination proves that the loops are not pure edge but their habit plane is usually closer to the first-order prismatic plane $\{10\bar{1}0\}$. It is even noticed that the habit plane of the <a>-loop is often tilted towards the first order pyramidal plane $\{10\bar{1}1\}$ [62].

The authors have also observed that for loop diameters lower than 40 nm the loops are circular but for diameters larger than 40 nm the vacancy loops become elliptical with the great axis along the $\langle c \rangle$ axis, the interstitial loops remaining circular. The $\langle a \rangle$ loops also appear to be aligned in rows parallel to the trace of the basal plane [58] [62].

For an irradiation temperature of 300 °C, no dislocation loop can be observed below a neutron fluence of 3×10^{23} n m^{-2} in the case of annealed Zy-2 irradiated at 300 °C [63]. However, from

this fluence, the loop density increases rapidly with increasing fluence but saturates at a density of 3×10^{22} m^{-3}, from a relatively low fluence of approximately 1×10^{24} n m^{-2} (**Figure 5**). The loop density saturation has been confirmed by X-ray diffraction analysis, when measuring the line broadening for increasing irradiation dose [68] [69]. The loop size exhibits a square-root increase with fluence, but no clear saturation in the evolution of the loop size is seen even after a fluence of 1×10^{25} n m^{-2} [63] [70].

Increasing the irradiation temperature leads to a decrease in the loop density and to an increase of the loop size [57] [71]. It was shown by Northwood *et al.* [57] that neutron irradiation performed at 350 °C of annealed Zy-2 up to a fluence of 1×10^{25} n m^{-2} leads to a mean loop diameter between 8 and 10 nm and a loop density between 8×10^{21} and 5×10^{22} m^{-3}; whereas a neutron irradiation of the same alloy performed at 400 °C up to a fluence of 1×10^{25} n m^{-2} leads to a mean loop diameter between 16 to 23 nm and a loop density between 4×10^{21} and 2×10^{22} m^{-3}. [57]. Above 500 °C, no irradiation damage is formed under neutron irradiation [64]. The ⟨ *a*⟩ loop microstructure is found to be very sensitive to alloying elements such as oxygen. Indeed, for high-purity zirconium with very low oxygen content, the ⟨ *a*⟩ loops are large and in low density [57], whereas for commercial zirconium alloys (with oxygen content between 1000 and 1500 ppm) the growth speed of loops is considerably reduced yielding smaller loops in much higher density [57].

A recent study of <a>-loop evolution under neutron irradiation at 358°C up to low dose [72] has confirmed the overall trend observed during earlier studies. From 1×10^{24} n m^{-2} to 10×10^{24} n m^{-2} the <a>-loop density increases from 3×10^{21} m^{-3} to 12×10^{21} m^{-3} in α-annealed Zircaloy-4, the average loop diameter being between 5 to 12 nm. For α-annealed Zircaloy-2, the <a>-loop density increases from 2×10^{21} m^{-3} to 8×10^{21} m^{-3} and the loop diameter ranges between 7 and 8 nm for the same fluences. Analyses done on a recrystallized Zr1%Nb alloy (M5) irradiated in a PWR up to higher fluences are also in agreement with early results, the loop number density being between 1 to 2.4×10^{22} m^{-3} while the mean loop size is between 7 and 10 nm [73]. In another Zr1%Nb alloy (E110) irradiated in fast neutron experimental reactor at temperatures between 330°C and 350°C, the <a>-loop density ranges between 3 to 5×10^{22} m^{-3} with diameter between 9 to 15 nm [74].

It was also reported from TEM observations that a particular band contrast of alternative black and white was superimposed on the usual radiation damage normally visible on thin foils of

irradiated materials. This phenomenon has been connected to the alignment of the loops in the same direction and may be a thin-foil artifact. It has been named 'corduroy' contrast by Bell [75]. The commonly accepted explanation of this artefact is based on the local elastic relaxation of the internal stresses in TEM thin foils, in areas where pronounced alignment of ⟨ *a*⟩ loops is present [76]. Shishov et al. [74] have also observed the loop alignment in neutron irradiated Zr1%Nb alloys. The average space between rows of loops is 15-20 nm. The loop ordering is increased when the iron content (and tin) is increased.

5.01.3.2 ⟨ *a*⟩ Loop evolution under irradiation: charged particle emulation

Thorough studies of radiation damage in zirconium using high-voltage electron microscope (HVEM) have been conducted by several authors in the past [77] [78] [79] [80] [81] [82] [83]. Because there are now only few HVEMs in operation, only one recent result has been published using this technique [84]. Heavy ion irradiations have also been used in early studies [59] [78] [85] [86] of radiation damage evolution in zirconium alloys. Recently, with the development of ion irradiation platforms, associated to the difficult access to material testing reactors, many results have been obtained concerning <a>-loop evolution under heavy [87] [88] [84] or light ion irradiations [89] [90] [91].

Quite remarkably, the main irradiation defects formed under charged particle irradiation are always <a>-loops, in good agreement with neutron irradiation. However, the size, the density and even the nature of the loops appear to depend on the incident particle, its energy, the irradiation temperature, damage rate and dose. The effect of damage rate is often an issue since the aim of charged particle irradiation is to reach in one or few days the same irradiation dose as the one seen by the materials in reactor during several months or even several years. It is commonly acknowledged that in order to balance for this dose rate effect it is necessary to perform the charged particle irradiation at a higher temperature. Some rules for this temperature shift can be found in [92] [8].

Furthermore, depending on the experimental procedure, surface effects can arise. Since the surface act as sink for point defects, the point defect evolution may be affected by the presence

of the surface, especially in the case of in situ experiments in TEM where the irradiation is performed on a thin foil.

Some discrepencies obtained between neutron irradiation and charged particle irradiation may also be explained by the difference in the primary damage. Indeed, electron irradiation does not create displacement cascade, light ions such as protons create small cascades and heavy ions create large displacement cascades, that can be similar to the one created by neutron irradiation. Because in displacement cascade, point defects recombine leading to fewer point defects free to migrate, the efficiency of neutron or ion irradiation is lower than that of electron irradiation. On the other hand, small clusters can already be formed within the cascades. This could increase the nucleation rate of point defect clusters.

Experimental studies using charged particle irradiation have been able to show that as the temperature increases the growth rate of loops increases and the number density of loops decreases (**Figure 7**) [78] [83] [84] [88] [91]. The effect of damage rate has also been studied, mainly by using HVEM [83]. It is shown that as the damage rate increases (in dpa/s), the loop growth rate (in nm/s) slowly increases.

The evolution of the loop size and density with dose can also be studied by charged particle irradiation. HVEM irradiation [78] [83] shows an increase of the loop size with irradiation dose, the loop density remaining nearly constant with dose for a given temperature (**Figure 7**).

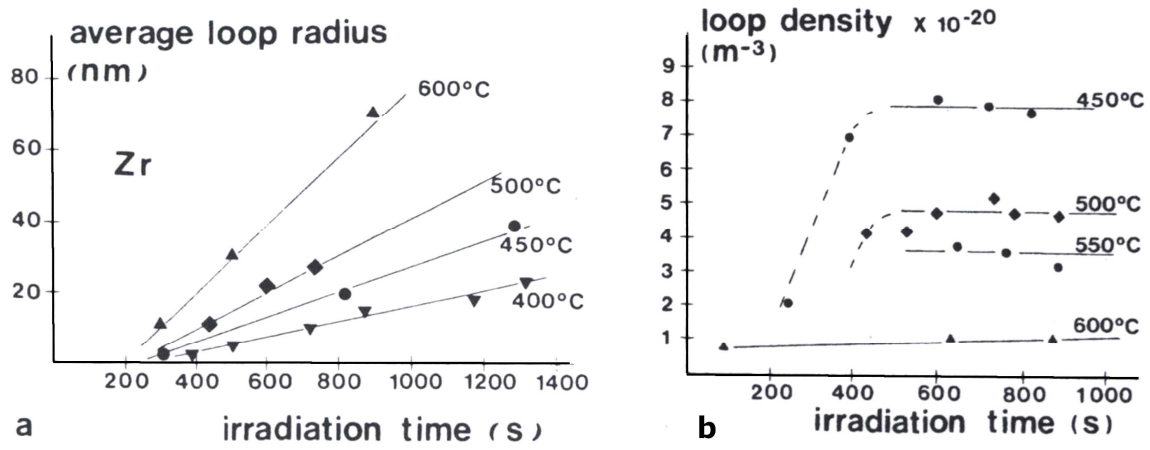

Figure 7 : Electron (HVEM) irradiation of pure zirconium (flux=4.6×10^{22} e/m^{2}s). (a) Influence of the irradiation temperature on the loop density; (b) fluence dependence of the average loop radii

at several temperatures. Adapted from Hellio, C., De Novion, C. H., & Boulanger, L. (1988) Journal of Nuclear Materials, 159, 368-378.

Some authors [79] [93] [90] [94] have been able to evidence the loop alignment after charged particle irradiation, as it can be observed after neutron irradiation.

The nature of <a>-loops has also been studied after heavy ion irradiation and electron irradiation. After electron irradiation, the microstructure of pure zirconium and zirconium alloys consists of both, vacancy and interstitial loops at temperatures below or equal 450°C. At 450°C, it was is shown that there was a higher proportion of interstitial loops [79] [84]. At temperatures above 450°C only interstitial loops were observed [79] [83]. This could be explained by the thermal emission of vacancies from vacancy loops at high temperature.

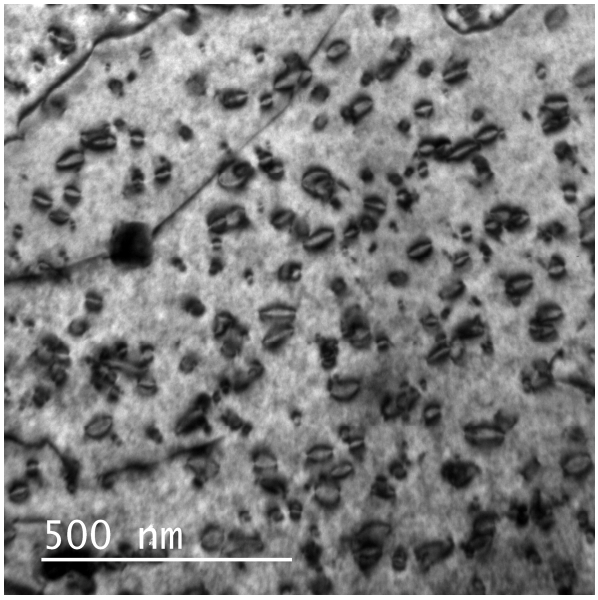

Figure 8: <a> loops formed during Zr ion irradiation conducted at 450°C up to a dose of 8×10^{17} ions/m^2 (0.6 dpa using 40 eV as displacement energy). Adapted from Gaumé, M., Onimus, F., Dupuy, L., Tissot, O., Bachelet, C., & Mompiou, F. (2017). Journal of Nuclear Materials, 495, 516-528.

Under heavy ion irradiations performed at temperatures equal or below 400°C, the loops are small leading to a difficult loop nature analysis. For an irradiation conducted at 450°C (**Figure**

8), only interstitial loops are observed [84] suggesting a shift towards lower temperatures of the critical temperature when vacancy loops evaporate. From the loop nature point of view, the results obtained after charged particle irradiation appear to be rather different from what is observed after neutron irradiation (at 400°C) where vacancy loops are observed in higher proportion at higher irradiation temperature.

The influence of alloying elements has also been studied by using charged particle irradiation on model alloys and comparing it to pure zirconium. It was observed by Hellio et al. [78] that increasing the alloying content (oxygen, niobium) decreases the loop diameter and increases the loop density. Topping et al. [93] [90] have found a segregation of iron on <a>-loops after proton irradiation of Zircaloy-2. It is also shown that the <a>-loop size is larger for a Zr-0.1Fe model alloy than for Zircaloy-2 also suggesting an effect of the alloying elements on the <a>-loop growth rate.

5.01.3.3 ⟨ *a*⟩ Loop formation and evolution: Mechanisms and modelling

The stability of the ⟨ *a*⟩ loops in zirconium was originally attributed to the relative packing density of the prismatic plane compared to the basal plane, which depends on the *c/a* ratio of the hcp lattice. Foll and Wilkens [95] have proposed that when the *c/a* ratio is higher than $\sqrt{3}$, loops are formed in the basal plane with Burgers vector $\frac{1}{6}\langle 20\bar{2}3\rangle$, whereas if *c/a* is lower than $\sqrt{3}$, then loops are formed in the prismatic plane with Burgers vector $\langle a\rangle = \frac{1}{3}\langle 11\bar{2}0\rangle$. For all hcp metals, this means that loops are formed in the prismatic plane except for Zn and Cd. This is not the case for Zr, Ti, and Mg where loops are also formed in the basal planes, depending on the irradiation dose, irradiation temperature, and purity of the metal [66] [67].

MD computations for α-zirconium have also shown that most of the small interstitial clusters produced in the cascade have the form of a dislocation loop with Burgers vector $\langle a\rangle = \frac{1}{3}\langle 11\bar{2}0\rangle$. Small vacancy clusters are also found in the prismatic plane [7] [35] [96]. For larger point-defect clusters [97], it is shown that the point-defect clusters in the prismatic plane always relax to perfect dislocation loops with Burgers vector $\langle a\rangle = \frac{1}{3}\langle 11\bar{2}0\rangle$.

More recently, a multi-scale approach has been proposed to assess the stability of various vacancy point defect clusters in zirconium. This approach combines ab-initio computations,

empirical potential simulations and continuum model based on elastic theory of dislocations [47]. These authors have been able to show that the formation energy of a perfect vacancy loop located in the prismatic plane with a <a> Burgers vector is lower than the formation energy of cavities and faulted vacancy loops in the basal plane. It is worth pointing out that empirical potential only, without using ab initio computation, predict a higher stability for cavities than <a>-loops, proving the need to conduct this combined method.

The origin of the tilted habit plane of <a> dislocation loops was first discussed by Kelly and Blake [60] and was thought to be due to a balance between energy loss on adopting more screw character and the energy gain due to increased line length when tilting the perfect <a> loop out of its pure edge direction. The tilting of loop out of the prismatic plane has also been recently observed in MD simulations in agreement with experiments [98].

The simultaneous observation of vacancy and interstitial $\langle a \rangle$ loops in zirconium alloys [57] [60] [62] [65] [71] is a rather surprising feature [67] [77]. Indeed, as discussed earlier, for usual cubic metals, interstitial loops tend to grow under irradiation and the vacancy loops tend to shrink since the edge dislocations are biased toward SIAs due to the EID.

According to Griffiths [67], the coexistence of these two types of loops in zirconium can be explained by a modified SIA bias in zirconium due to (i) a relatively small relaxation volume of SIA relative to vacancy (low bias), (ii) interaction with impurities, or (iii) spatial distribution of vacancy loops and interstitial loops as a result of elastic interactions or anisotropic diffusion. Other authors [77] [99] suggested that this phenomenon is due to a subtle balance of the bias factors of the neighboring point-defect sinks that lead to an increasing bias as the loop size increases if the loop density is high. Woo [55] considers that the coexistence of both types of $\langle a \rangle$ loops can be explained in the frame of the DAD model, which induces a strong DAD-induced bias. Indeed, in this model, the $\langle a \rangle$ type loops are relatively neutral and may therefore receive a net flow of either interstitials or vacancies, depending on the sink situation in their neighborhood. Christien and Barbu [100] have used a mean field approach called cluster dynamics. In this model they have introduced some of the hypothesis of the DAD theory and they have computed the damage evolution under electron irradiation as a function of dose, temperature and also thin foil orientation with respect to the <c>-axis. This model failed to reproduce the coexistence of vacancy and interstitial <a>-loops observed under HVEM

irradiation. However, in their cluster dynamics model, Dubinko et al. [99] succeeded in having the coexistence of vacancy and interstitial <a>-loops.

Finally, computations [101] using the Monte Carlo method have been carried out. In these simulations, the large vacancy and interstitial point-defect clusters created inside the cascade are taken into account as an input microstructure. Furthermore, SIAs exhibit 1D or 2D migrations in the basal plane. The results show that both vacancy and interstitial loops are able to grow simultaneously, the proportion of vacancy loops increasing with increasing irradiation temperature.

5.01.3.4 ⟨ *c*⟩ Component dislocation loops under neutron irradiation

At the time of the thorough review by Northwood [63], no ⟨ *c*⟩ component loop had been observed yet. The 'round robin' work [57] also established that up to an irradiation fluence of 1 × 10^{25} n m^{-2} no ⟨ *c*⟩ component dislocation loop is observed. As highly irradiated Zircaloy samples became available, for fluence higher than 5 × 10^{25} n m^{-2}, evidence of ⟨ *c*⟩ component loops arose [58] [65] [102] [103] [104] [105] [106]. The ⟨ *c*⟩ component loops have been analyzed as being faulted (basal stacking fault I_1) and of the vacancy type. They are located in the basal plane with a Burgers vector $\frac{1}{6}\langle 20\bar{2}3\rangle$ having a component parallel to the ⟨ *c*⟩ axis (**Figure 9**). The ⟨ *c*⟩ component loops are much larger than the ⟨ *a*⟩ loops but their density is much lower. For instance, for recrystallized Zy-2 and Zy-4 irradiated at 300 °C, after 5.4 × 10^{25} n m^{-2}, ⟨ *c*⟩ component loops are found with a diameter of 120 nm and with a density between 3 and 6 × 10^{20} m^{-3}. From X-Ray Diffraction line broadening analysis, some authors [68] have been able to confirm that the <c>-component dislocation structure can evolve over long periods of irradiation (>10^{26} n.m^{-2}) in annealed (recrystallized) Zy-4 irradiated at 300°C, although the <a>-type dislocation structure tends to saturates at low fluences (lower than 10^{25} n.m^{-2}). It is also seen that the line broadening is much less for <c>-type dislocation structure (with an estimated line density of 10^{13} m^{-2}) than for <a>-type dislocations (estimated line density of 8×10^{14} m^{-2}), which is consistent with the lower <c>-loop density compared to <a>-loops. These results have been confirmed by diffraction line profile analysis [107] of Zr-2.5Nb samples irradiated up to low fluences and on annealed Zy-2 irradiated up to higher fluences [69].

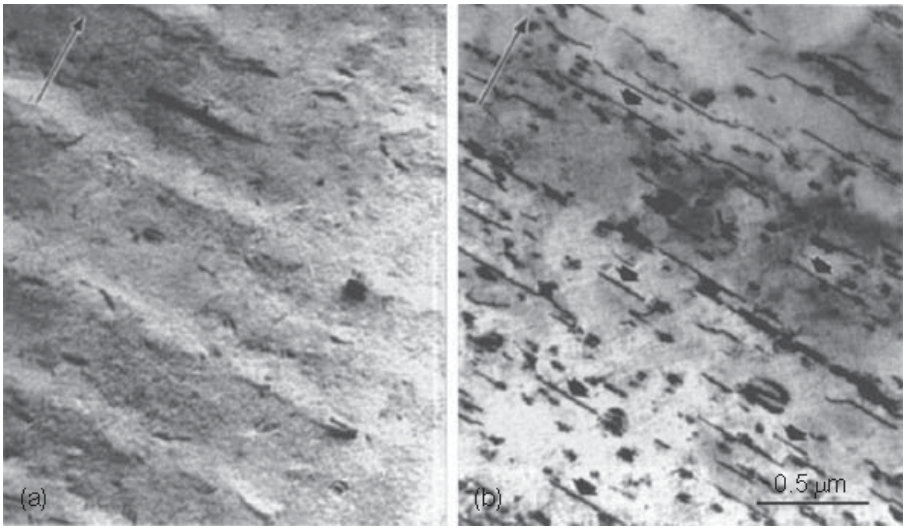

Figure 9 Comparison of neutron damage in Zr at 700 K following irradiation to a fluence of 1.5 × 10^{26} n m^{-2}. (a) Crystal bar purity (500 wt ppm) with no *c*-component loops. (b) Sponge purity (2000 wt ppm) containing basal ⟨ *c*⟩ component in an edge-on orientation (arrowed). Only ⟨ *c*⟩ component defects are visible with diffracting vector of [0002]. The beam direction is [100] for each micrograph. Adapted from Griffiths, M. *Philos. Mag. B*. **1991**, *63*(5), 835–847.

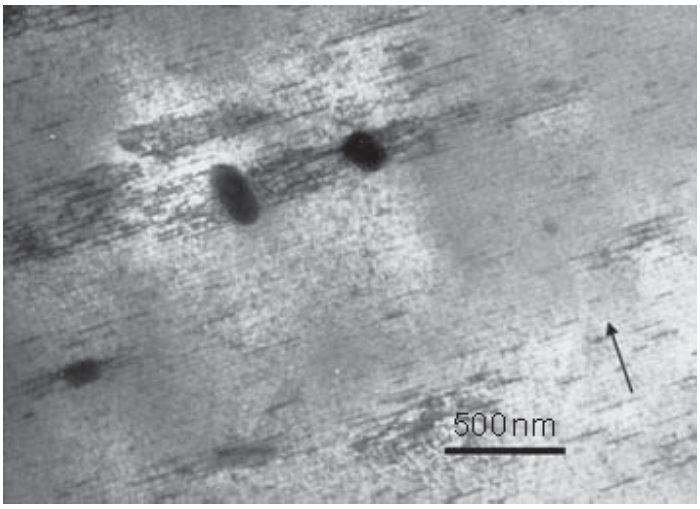

Figure 10 High density of *c*-component loops in the vicinity of the precipitates in a Zy-4 sample irradiated to 6 × 10^{25} n m^{-2} at 585 K. The arrow shows the diffracting vector [0002]. Adapted from De Carlan, Y.; Régnard, C.; Griffiths, M.; Gilbon, D. Influence of iron in the nucleation of ⟨ *c*⟩ component dislocation loops in irradiated zircaloy-4. In *Eleventh International Symposium*

on Zirconium in the Nuclear Industry, 1996; Bradley, E. R., Sabol, G. P., Eds.; pp 638–653, ASTM STP 1295

For irradiation temperatures below or equal 350°C, these ⟨ *c*⟩ component loops are always present in conjunction with more numerous and finer ⟨ *a*⟩ loops. The ⟨ *c*⟩ component loops can therefore only be easily observed edge-on by TEM by using the $g = 0002$ diffraction vector, which leads to invisible ⟨ *a*⟩ type defects. The ⟨ *c*⟩ loops thus appear as straight-line segments. For higher irradiation temperatures or after post-irradiation annealing [105] [108], large circular <c> loops can be clearly observed.

There is considerable evidence to show that the formation of <c>-loops under neutron irradiation is dependent on the purity of the zirconium used (**Figure 9**) [58] [80] [109] [110] [111]. Indeed, it is seen, when comparing a high purity zirconium crystal bar (from the Van Arkel – de Boer process) and a lower purity zirconium sponge (from the Kroll process), that for the same neutron irradiation, the highest purity material always contents less <c>-loops than the others [105] [112].

Concerning recrystallized Zr1%Nb alloys and quaternary alloys (Zr, Nb, Sn, Fe) [113] [114] [73] [15], it is commonly observed that there are much less <c>-loops than in recrystallized Zy-4 or Zy-2 suggesting an effect of niobium on the nucleation and growth of <c>-loops.

The role of iron on the nucleation and growth of <c>-loops under neutron irradiation appears to be complex. Indeed, in Zircaloys, it is observed that at the beginning of their formation, <c>-component dislocation loops are located close to the intermetallic precipitates, and especially the Laves phases $Zr(Fe, Cr)_2$ present in the material [58] [111] (**Figure 10**). [112] [115]. This is attributed to the role of iron which is a fast diffuser and has a very low solubility limit in the zirconium matrix. Iron diffuses out of the precipitate under irradiation and promotes <c>-loop nucleation. The segregation of iron on an assumed <c>-loop after neutron irradiation has been evidenced using Atom Probe Tomography (APT) by Sundell et al. [116] on a neutron irradiated Zy-2, close to the metal-oxide interface. Similar observations have recently been done by Topping et al. [93]. A high spatial resolution chemical analysis done using TEM on a neutron irradiated Zircaloy-2 [90] also suggests a segregation of iron along basal planes, close to Laves phases, where <c>-loops can also be observed.

However, it has been shown by several authors [15] [117] that in Zr1%Nb and quaternary alloys (ZrNbSnFe), the <c>-component loop linear density decreases when increasing the overall iron content. This has been confirmed by recent experimental neutron irradiation where the effect of alloying elements on growth deformation and <c>-loops microstructure has been systematically studied on various industrial and also model alloys [118]. This work shows that increasing the iron matrix content significantly decreases the <c>-loop density.

Furthermore, it was suspected that in-reactor hydrogen pickup, which occurs during the corrosion process of zirconium alloys in normal operating conditions, can increase the <c>-loop formation and growth. Yagnik et al. [118] investigated the role of pre-hydriding of zirconium alloys on <c>-loop microstructure. They established that the <c>-loop density was higher in the pre-hydrided samples with 100 wpmm hydrogen compared with as-fabricated samples. However, when increasing the hydrogen from 100 wppm to 700 wppm, the <c>-loop density does not increase further showing that it is the hydrogen in solid solution which affects the <c>-loop growth rather than the hydrogen in the form of hydrides.

5.01.3.5 ⟨c⟩ Loop evolution: emulation using charged particle irradiation

The study of <c>-loop evolution has mainly been done by using HVEM during the 80s and 90s. These analytical studies have been able to establish very valuable results that still help nowadays to understand the in-reactor microstructure evolution.

In an early study, Griffiths et al. [80] have observed the nucleation and growth of <c>-loops having Burgers vectors of $1/6\langle 20\bar{2}3\rangle$ and $1/3\langle 11\bar{2}3\rangle$ during electron irradiation of pure Zr. HVEM irradiations have also been able to evidence, in-situ, the climb of <c>-component dislocations from <c>-loops [109] [82]. It is also seen that for very high damage dose, the <c>-component loops transform into cavities.

When comparing high purity zirconium crystal bar and lower purity zirconium sponge after HVEM irradiation, it is seen that basal loops are easily produced in zirconium sponge whereas they are fewer and smaller in the zirconium crystal bar [109]. By using an HVEM on iron-doped samples [111], it has been possible to prove that iron enhances the nucleation of the $\langle c \rangle$ loops,

the loop density increasing as a function of the iron content. Moreover, iron was found to have segregated in the plane of the loops [111].

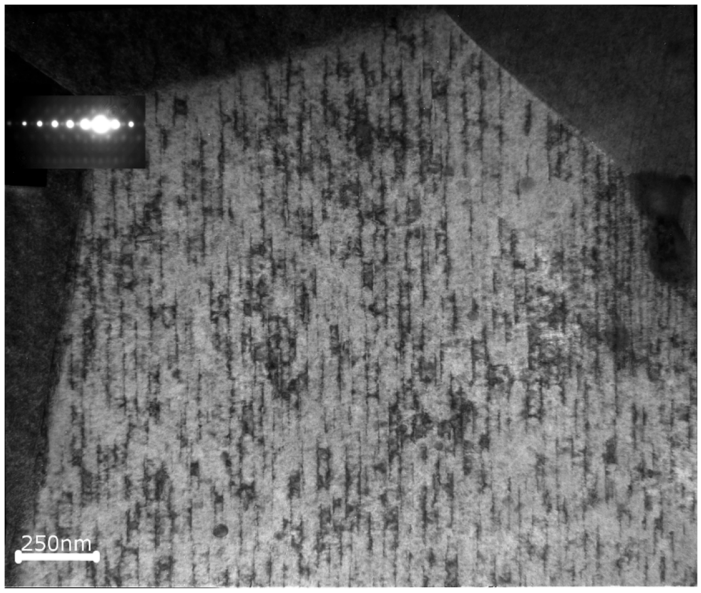

Figure 11 : <c>-component loops observed after 2 MeV proton irradiation of RXA Zy-4 conducted at 350°C up to a dose of 9×10^{23} protons/m^2 (12.5 dpa using 40 eV as displacement energy). Adapted from Tournadre, L., Onimus, F., Béchade, J. L., Gilbon, D., Cloué, J. M., Mardon, J. P., & Feaugas, X. (2013). Journal of Nuclear Materials, 441(1-3), 222-231.

More recently, heavy or light ions have been used to study <c>-loop evolution in zirconium alloys also establishing very interesting results. By using proton irradiation Tournadre et al. [119] [120] [121] have shown that it is possible to observe <c>-component loops after proton (Figure 11) irradiation and they have been able to confirm that in Zr1%Nb alloys the <c>-loops linear density is much less than in recrystallized Zy-4. Furthermore, by using pre-hydrided samples it has been possible to show that the presence of hydrogen in solid solution decreases the incubation dose for <c>-loops. Harte et al. [90] and Topping et al. [93] also used proton irradiation to study the role of alloying elements redistribution on <c>-loop evolution. They suggest a correlation between iron and nickel segregation and <c>-loops. It is also interesting to note that Harte et al. [90] managed to observe circular <c>-loops after proton irradiation conducted after 7 dpa at 350°C without prior annealing.

Several authors have also used heavy ions (mainly Zr or Kr ion) to study <c>-loop evolution under irradiation. Tournadre et al. [120] and Gharbi et al. [122] found rather small <c>-loops (less than 100 nm diameter) after Zr ion irradiation at 300°C with only limited difference between Zr1%Nb alloy and Zircaloy-4. Yamada et al. [123] obtained large <c>-loops in pure Zr after Zr-ion irradiation at 300°C and 400°C up to very high doses. However, because of Focused Ion Beam (FIB) milling the thin foil contained many large hydrides. Hengstler-Eger et al. [124] and Idrees et al. [88] [125] observed in situ the <c>-loop evolution in pure Zr and commercial Zr alloys during Kr ion irradiations on thin foil at various temperatures. These authors observed the incubation dose for loop formation and the rapid growth of <c>-loops. Furthermore, using Zr ion irradiation Gharbi et al. [122] have been able to study the impact of an applied stress on the <c>-loop nucleation and growth. A rather limited effect of the applied stress on <c>-loop nucleation and growth was noticed during these experiments.

5.01.3.6 ⟨ *c*⟩ -Loop formation: mechanisms and modelling

It is surprising that although the most stable loops are the prismatic loops, basal loops are also observed in zirconium alloys. Moreover, these loops are of vacancy nature. According to the usual rate theory, vacancy loops should not grow as a result of the bias of edge dislocation toward SIAs. Furthermore, because the Burgers vector of <c>-component loops is bigger than the Burgers vector of <a>-loops, the bias of <c>-component loops towards SIAs should be stronger than the bias of <a>-loops. This should then result in a shrinkage of vacancy <c>-loops under irradiation, and no vacancy <c> loop must be observed.

The reason for the nucleation and growth of the ⟨ *c*⟩ -component loops in zirconium alloys has been analyzed and discussed in detail by Griffiths and co-workers [58] [66] [67] [80]. The most likely explanation for their appearance [58] is that they nucleate in collision cascades. Voskoboynikov [23] observed a variety of vacancy clusters when simulating displacement cascades. One of them is a pyramid created by the collapse of crystalline planes above an agglomeration of vacancies in the basal plane. As a result, an extrinsic stacking fault is created in the basal plane. If this defect transforms into a basal loop with Burgers vector $b=c/2$ and an extrinsic stacking fault (E), it could then change, by glide of a Shockley partial dislocation, creating a basal loop with $\underline{b} = \frac{1}{6}\langle 20\bar{2}3\rangle$ Burgers vector and an intrinsic stacking fault I_1 as

described by Hull and Bacon [126] and proposed in [120]. Indeed, it is assessed by Varvenne et al. [47] that the basal loop with intrinsic stacking fault is more stable than the loop with extrinsic stacking fault for loop radius larger than 1.4 nm. Christiaen et al. [127] recently observed, using MD simulations, a stacking fault bipyramid resulting from the relaxation of a perfect <c> loop (with a <c> Burgers vector). It is found that as the bipyramid grows it must transform into the perfect <c> loop which is more stable for larger size. From their results, the authors infer that the same process must also occur for faulted <c> loops. A new scenario for faulted <c> loops formation in then proposed. For small size, basal vacancy cluster is in the form of stacking fault pyramid, similar to stacking fault tetrahedron in FCC metals. Then, as the defect grows, it transforms into faulted <c> loop. Other authors [94] have also recently suggested that the presence of <a>-loop alignment could promote <c>-loop nucleation under displacement cascades.

The stability of <c>-component loops is dependent, to a large extent, on the presence of solute elements, such as iron or hydrogen, which lower the basal stacking-fault energies (E and I_1) of the Zr lattice, making the basal $\langle c \rangle$ component loops more energetically stable [128]. It is also possible that small impurity clusters, especially iron in the form of small basal platelets, could act as nucleation sites for these loops [80] [110].
However, according to Griffiths [58], this cannot account for the very large vacancy $\langle c \rangle$ component loops observed, since the growth of vacancy loops is not favorable considering the EID discussed previously. In order to understand the reason for the important growth of the $\langle c \rangle$ component loops, another mechanism must occur. As discussed by Woo [55], the growth of $\langle c \rangle$ component loops is well understood in the frame of the DAD model. Indeed, because of the higher mobility of SIAs in the basal plane rather than along the $\langle c \rangle$ axis (and the isotropic diffusion of vacancies), dislocations parallel to the $\langle c \rangle$ axis will absorb a net flux of SIAs whereas dislocations in the basal plane will absorb a net flux of vacancies. This can therefore explain why the basal vacancy loops can grow.
Most of the hypotheses of the DAD model have been introduced into the cluster dynamics model developed by Christien and Barbu [129]. The authors also assumed that the nucleation of <c>-loops occurs because of the presence of small iron platelets. With this model, the authors

succeeded in computing the evolution of the growth strain as a function of dose for zirconium single crystal.

Because recent *ab-initio* computation failed to find any anisotropic diffusion of point defects that could explain the growth of <c>-component loops under irradiation, several authors have proposed alternative explanations. Barashev et al. [56] proposed that it is the 1D diffusion of small SIA clusters in the basal plane which plays the role of the anisotropic diffusion of single SIAs thus explaining the growth of <c>-component loops for similar reasons than in the DAD model. Using this last assumption, along with assumptions on the <a>-loop and <c>-loop evolution, they proposed a simple rate theory model which is able to predict the growth strain as a function of dose of zirconium single crystal. Following the work of Barashev et al. [56], Choi et al. [130] have improved the above model to compute the growth strain of annealed zirconium polycrystals.

Rouchette et al. [131] did not consider the mobility of small SIA clusters but investigated in detail the sink strength (or efficiency) of loops. They showed that SIAs in Zr induce a much stronger deformation in the basal plane than parallel to the <c> axis. The basal configuration of SIAs thus leads to the highest capture bias for prismatic loops. Consequently, while prismatic loops absorb more SIAs, basal loops will experience a net flux of vacancies. The shape anisotropy of SIAs could therefore explain the basal vacancy loop growth in irradiated zirconium alloys. It is also possible that saddle point anisotropy, pointed out by Woo [132] [80], and recently evidenced in other metals [133], could play a significant role on microstructure evolution under irradiation of zirconium.

The incubation period before the appearance of $\langle c \rangle$ component loops is a rather puzzling phenomenon which has been discussed by many authors. First, it can be wondered whether the <c>-loops are already present but too small to be observed by TEM or whether they really appear only from a threshold dose. However, it is clear, when reading the literature, that when <c>-loops start to be visible they grow very rapidly. Indeed, after neutron irradiation, the <c>-loops observed are always large, typically 100 nm diameter.

According to Griffiths *et al.* [106], the incubation dose could be explained by the fact that the $\langle c \rangle$ loop formation is dependent on the volume of the matrix containing a critical interstitial solute concentration. This volume increases as the interstitial impurity concentration is gradually supplemented by the radiation-induced dissolution of elements such as iron from intermetallic

precipitates (or β-phase in the case of Zr–Nb alloys). For a high enough concentration of solute elements, <c>-loops nucleate. As described earlier, Christiaen et al. [127] propose that for small size basal vacancy clusters are in the form of pyramid. As the dose increases these pyramids grow. When they reach a critical size, for a corresponding threshold dose, they collapse into faulted <c> loops. This mechanism could explain the fact that small <c>-loops (smaller than 10 nm) are never observed, thus explaining the incubation dose. Other authors [94] propose that the formation of <c>-loops is related to the presence of already formed <a>-loops, thus explaining that <c>-loops can only be observed when a high enough density of <a>-loops are present. This could also account for the incubation dose.

Atomistic computations have been used to understand the influence of impurities or alloying elements on the nucleation and growth of <c>-loops. It is especially shown that hydrogen atoms [53] [128] exhibit a significant binding energy with vacancy clusters, thus stabilizing the small vacancy clusters. Furthermore, hydrogen decreases the basal stacking fault energy, which in turns increases the stability of faulted basal vacancy loops.

The role of iron has also been studied by *ab-initio* computations. It was shown that there is a strong binding energy between iron atoms and vacancies [134]. Ordered structures iron-zirconium are rapidly formed in vacancy clusters. One effect of iron could be to bind vacancy clusters to the formation of nano-intermetallic phases instead of making them available for generating vacancy <c>-loops. This could then explain that in ZrNb alloys, increasing the iron content reduces the <c>-loop nucleation and growth.

5.01.3.7 Void formation

Early studies failed to show any cavity in Zr alloys after irradiation [135]. From all the obtained data, it is seen that zirconium is extremely resistant to void formation during neutron irradiation (**Figure 12**) [58] [64]. As reviewed by Faulkner and Woo [136] this has been attributed to several factors such as a low dislocation bias for interstitials [64] or the effect of very low production of helium by (n, α) reactions during neutron irradiation. Faulkner and Woo [136] also suggest that the relatively low vacancy formation energy and the relatively high atomic volume could explain the resistance to void formation of zirconium compared to steels. But most probably, the fact that for zirconium alloys vacancy <a> type loops in prismatic planes are more

stable than voids, as shown by atomistic computations [47], can be the reason for the absence of void. Moreover, the vacancy <c>-loops that grow, after the incubation dose, act as sinks for vacancies further preventing the formation of voids. To favor the formation of voids, various studies performed, especially on model alloys, have shown that stabilization of voids can occur when impurities are present in the metal. Helium coming from transmutation of boron on Zr sponge [70] as well as impurities located near Fe-enriched intermetallics are found to favor the stability of voids [65].

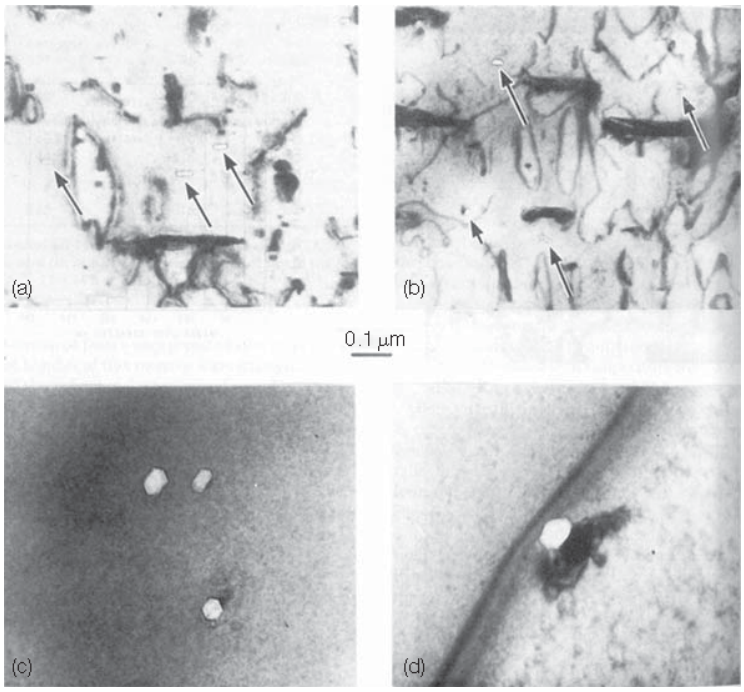

Figure 12 Examples of radiation-induced cavities in zirconium alloys. (a) Annealed zirconium crystal-bar, prism foil, 673 K, 1.2 × 10^{25} n/m^2; (b) annealed zircaloy-2, prism foil, 673 K, 1.2 × 10^{25} n/m^2; (c) annealed Zr-2.5 wt% Nb, basal foil, 923 K, 0.7 × 10^{25} n/m^2; (d) typical cavity attached to inclusion on a grain boundary, material (c). Adapted from Gilbert, R. W.; Farrell, K.; Coleman, C. E. *J. Nucl. Mater.* **1979**, *84*(1–2), 137–148

Irradiations with electrons give better conditions to stabilize voids: the main reason is probably that irradiation doses can be very high – hundreds of displacements per atom can be reached after few hours [109]. Moreover, electron irradiation on Zr samples preimplanted with He at various concentrations showed the nucleation and growth of voids only for the samples doped

with at least 100 ppm of He [136]. Implantation of Kr or He in zirconium or Zircaloys [137] [138] induce the formation of a high density of small bubbles which exhibit as self-organization pattern in the shape of a bubble super-lattice. This last phenomenon is attributed by the authors to the two-dimensional self-interstitial diffusion.

5.01.4 Secondary-phase evolution under irradiation and alloying element redistribution

In addition to point-defect cluster formation, irradiation of metallic alloys can affect the precipitation state as well as the alloying elements in solid solution. The instability of the precipitates under irradiation is of great importance since the secondary-phase precipitates play a major role on the corrosion resistance of zirconium alloys. Furthermore, alloying elements redistribution can affect the nucleation and growth of point defect clusters and especially the basal <c>-component loops. Since these loops are at the origin of the accelerated growth, a good knowledge of the alloying elements evolution under irradiation is essential.

5.01.4.1 Crystalline to amorphous transformation and dissolution of Zr-(Fe,Cr,Ni) intermetallic precipitates in Zircaloys

5.01.4.1.1 Zr-(Fe,Cr,Ni) precipitates under neutron irradiation

Transmission Electron Microscopy (TEM) observations reveal that for Zircaloys (Zircaloy-2 and Zircaloy-4), irradiated at temperatures typical for commercial light water reactors (around 330°C), $Zr(Fe,Cr)_2$ Laves phase precipitates begin to become amorphous after a fluence of about 3×10^{25} n m^{-2}. Furthermore, this amorphization is associated with a dissolution of alloying elements from the precipitates into the matrix. It is often observed that the precipitates dissolve preferentially parallel to the basal plane creating saw-tooth like irregularities on the periphery of the particle, the zigzag edge of the precipitate being parallel to the <a> and <c> directions of the matrix [139]. The other common precipitates present in Zircaloy-2, the $Zr_2(Fe,Ni)$ Zintl phase precipitates, remain crystalline up to higher irradiation doses [135] [110] [140]. The periphery of the $Zr_2(Fe,Ni)$ Zintl structure particles can also exhibits irregularities due to progressive dissolution, but without amorphization [110] [141]. It is proposed by several authors [142] [143] that the preferential dissolution of the precipitates along the basal plane is the result of the anisotropic diffusion of SIAs [53] which is more rapid in the basal plane. The flux of SIAs toward the precipitate would result in a flux of alloying elements in the opposite direction, from the precipitate toward the matrix, by a replacement mechanism.

The effect of temperature on the crystalline to amorphous transformation has been studied by various authors [110] [144] [145] [139] [140] [146]. It is shown that, at low temperatures, under neutron irradiation, both $Zr(Fe,Cr)_2$ and $Zr_2(Fe,Ni)$ undergo a rapid and uniform crystalline to

amorphous transformation [145] from a dose threshold, without any composition change. As the irradiation temperature increases, a higher dose is required for amorphization. It is indeed seen that, at an "intermediate temperature", $Zr(Fe,Cr)_2$ precipitates undergo only a partial amorphous transformation (**Figure 13**) and that $Zr_2(Fe,Ni)$ particles remain crystalline.

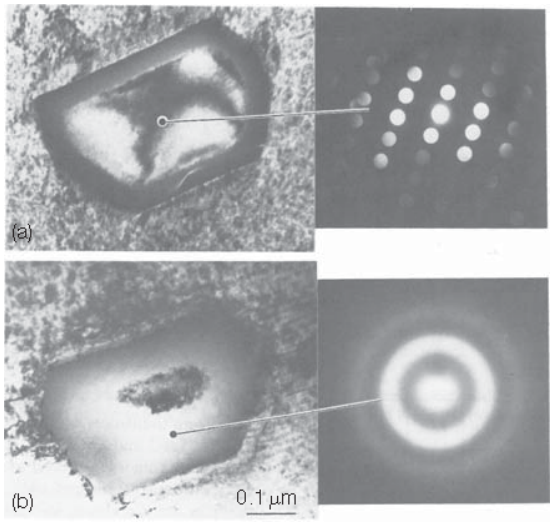

Figure 13 Crystalline to amorphous transformations of $Zr(Cr, Fe)_2$ particle in Zy-4 irradiated in a BWR at 560 K: (a) $3.5x10^{25}$ n m^{-2} and (b) $8.5x10^{25}$ n m^{-2}. Adapted from Griffiths, M.; Gilbert, R. W.; Carpenter, G. J. C. J. Nucl. Mater. 1987, 150(1), 53–66.

The crystalline to amorphous transformation starts at the periphery of the particles, and then the amorphous rim moves inward until the whole precipitate becomes fully amorphous. The chemical concentration profile within the precipitates also exhibits two distinct zones corresponding to the two different states: the crystalline core and the amorphous periphery. The amorphous layer exhibits a lower iron content than the initial precipitate [142], the iron profile showing a local drop from the standard value of 45 at% (Fe/Cr~1.7) to below 10 at.% (Fe/Cr<0,5) (**Figure 14**). At higher temperatures, amorphization was not detected [110] [145] and the precipitates remained crystalline, but some authors [144] have nevertheless observed a loss of iron at the periphery of the particles and even a total dissolution of $Zr_2(Fe,Ni)$ and $Zr(Fe,Cr)_2$ precipitates and redistribution of alloying elements. When a progressive dissolution without amorphization is observed, the periphery of the $Zr(Fe,Cr)_2$ particles is full of irregularities where the Fe/Cr ratio tends to 1 [113] (see **Figure 15**).

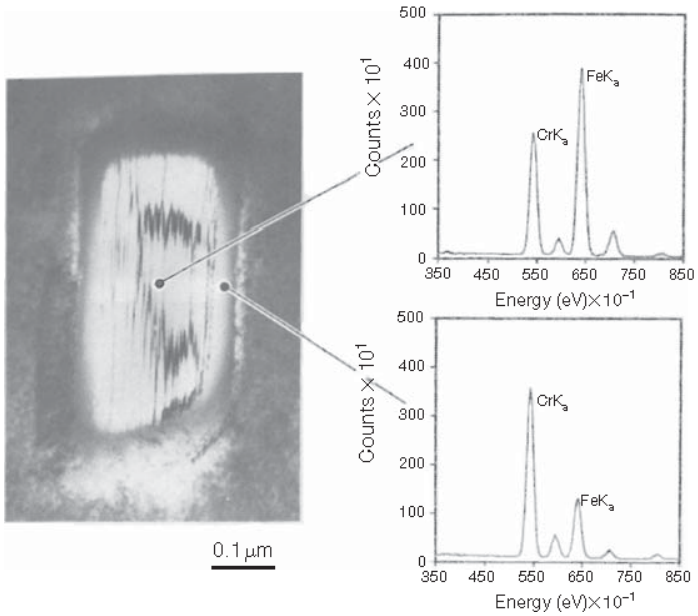

Figure 14 Crystalline to amorphous transformation of $Zr(Fe,Cr)_2$ particle in Zircaloy-4 irradiated at 3.5X1025 n/m2. Energy Dispersive X-ray Spectroscopy spectrum shows that the amorphous volume is coincident with a depletion of Fe. Adapted from Griffiths, M.; Gilbert, R.W..; Carpenter, G.J.C.J. Nucl. Mater, 1987, 150(1), 53-66.

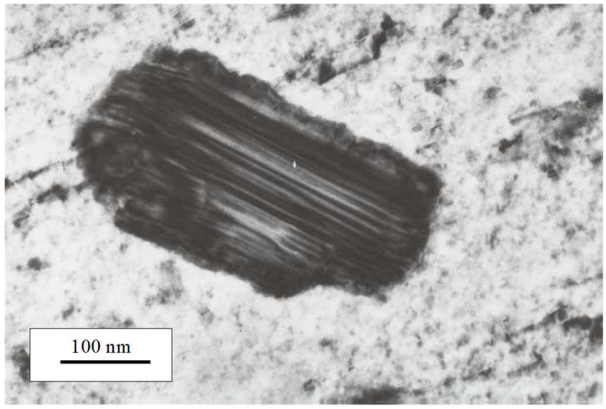

Figure 15 Evolution of a $Zr(Fe,Cr)_2$ precipitate irradiated $4.9x10^{25}$ n/m^2 at 400°C with irregularity on the periphery. Adapted from Doriot, S.; Gilbon, D.; Béchade, J. L.; Mathon, M.;Legras, L.; Mardon, J. P. J. ASTM Int. 2005, 2, 175–201.

5.01.4.1.2 Mechanisms of Zr-(Fe,Cr,Ni) precipitates evolution under neutron irradiation

Laves phases

To explain the $Zr(Fe,Cr)_2$ (Laves phase) behavior under neutron irradiation, several authors [110] [140] [113] have proposed a competition between thermal diffusion recovery and irradiation damage. Three temperature regimes can be distinguished for damage rates typical of neutron irradiations.

i) Low temperature regime

The uniform crystalline to amorphous transformation of $Zr(Fe,Cr)_2$ (Laves phase) precipitates, at low temperature (below a critical temperature referred to as T_{C1}), is easily understood in terms of ballistic radiation-induced disordering. At this temperature, the recombination of point defects or recrystallization within the intermetallic precipitate is too slow to compensate for the rate of atomic displacement [144]. The dissolution of alloying elements remains limited at this low temperature and the amorphization is mainly due to sputtering, that is, transfer of matter from the particle because of atomic displacements by neutrons. When the point-defect concentration becomes too high and/or when the chemical disordering is too high, the crystalline structure is destabilized and undergoes a transformation to an amorphous phase [110] [144] with only a limited dissolution [125].

ii) Intermediate temperature regime

At higher temperature, in the intermediate temperature regime ($T_{C1} < T < T_{C2}$), the $Zr(Fe, Cr)_2$ (Laves phase structure) precipitates undergo a progressive amorphization that starts at the precipitate–matrix interface forming a front that gradually moves into the precipitate. This phenomenon is believed to happen by a deviation from stoichiometry due to a ballistic interchange of iron and zirconium atoms across the precipitate–-matrix interface. It also agrees with the observed kinetics of amorphization, predicting an amorphous thickness proportional to fluence and the absence of an incubation period for the transformation to start [147]. Some authors explained this progressive amorphization in $Zr(Fe,Cr)_2$ by the metastable free-energy diagram of the Zr-Fe alloy [148]. The reason for the drastic depletion of iron from the precipitates after amorphization is not clearly understood yet. According to Griffiths *et al.* [144] iron may be in some form of irradiation-induced interstitial state in irradiated zirconium alloys and may then diffuse rapidly,

through interstitial process, out of the intermetallic particles. This intermediate temperature regime may be referred to as the progressive dissolution and amorphization.

ii) High temperature regime

At higher temperatures ($T > T_{C2}$ with T_{C2} typically higher than $0.3T_m$), the thermal activation is sufficient to induce dynamic recrystallization impeding the amorphization of the precipitates. Because of the high mobility of Fe and Cr, redistribution of solute can occur, leading to secondary-precipitate formation. This high temperature regime can be referred to as dissolution without amorphization.

The two critical temperatures, T_{C1} and T_{C2}, depend on the dose rate. For a higher dose-rate the critical temperatures are expected to be higher and the precipitates are predicted to be amorphized more quickly, since the vacancy concentration will be higher at a given fluence, compared to a low dose rate [149]. Under neutron irradiation, with a dose-rate similar to that of a Pressurized Water Reactor (PWR), the transition temperature T_{C1} for $Zr(Fe,Cr)_2$ in Zircaloy-4 seems to be between 280°C and 290°C [65] [139] [149]. Furthermore, a critical temperature T_{C2} for neutron irradiation in PWR of about 370°C for $Zr(Fe,Cr)_2$ in Zircaloy-4 can be deduced from the literature [58] [110] [139] [113] [150] [149]. However this transition temperatures can be different depending on the Fe/Cr ratio if the chemical composition of the alloy is different from that of Zircaloy-4. Indeed, the susceptibility of the $Zr(Cr, Fe)_2$ particles to amorphize increases with increasing Cr content as seen by Griffiths *et al.* [65] and Harte *et al.* [141].

Zintl phases

The fact that $Zr_2(Fe, Ni)$ Zintl phase remains crystalline at intermediate temperatures is presumably due to a more rapid reordering than the disordering in this structure. However, at lower temperature, as low as 60°C, the radiation resistance of the $Zr_2(Fe, Ni)$ Zintl phase is lower than that of the $Zr(Fe,Cr)_2$ Laves phase [151]. It was further stated by Harte et al. [141] that in the Zr_2Ni system, the vacancy and antisite defects have, on average, lower formation energies than in the $ZrCr_2$ system. This suggests that if both systems had an equal number of defects, then the Zr_2Ni would be in a lower free energy state. Although this could explain why the Fe-Ni particles recover from irradiation damage more effectively than the Fe-Cr, arguments based on free energy are not

strictly valid when considering the dynamics and localized nature of ballistic collision cascades [152].

Relationship between <a>-loops, <c>-loops and secondary phase particle dissolution

As described earlier, the evolution of Zr-(Fe,Cr,Ni) intermetallic precipitates in Zircaloys has a significant effect on <c>-loop formation. Indeed, the <c>-component loops are more numerous at the vicinity of second phase particles which undergo a high loss of iron (see Figure 17) suggesting an effect of iron on <c>-loop formation in Zircaloys [58] [110] [111] [112]. Some authors pointed out however that chromium is a slower diffuser than iron and localization of <c>-component loops near $Zr(Fe,Cr)_2$ particles could be linked to chromium instead of iron [58].

Fe and Sn were observed by atom probe tomography study (APT) to segregate to ring-shaped features in the metal that were interpreted to be <c>-component vacancy loops [116]. A recent study conducted by Cockeram *et al.* using APT examinations of Zircaloy samples from HFIR neutron irradiations at 360°C, has evidenced the segregation of Fe, Sn and Cr and cluster formation at features similar in size, shape and number density as the <a> loops previously characterized by TEM [153]. Similar observations were done using EDX on a Zircaloy-2 irradiated in a BWR at 280-330°C [141] (**Figure 16**).

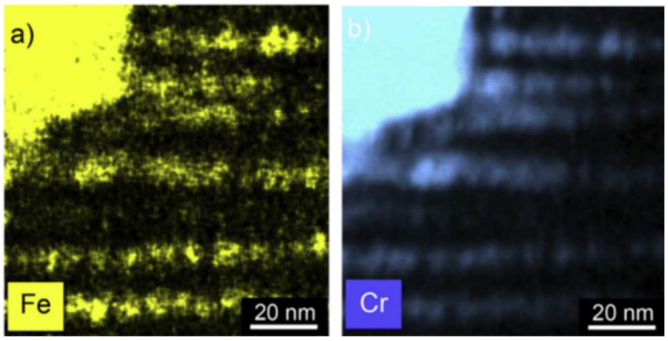

Figure 16: Fe and Cr map near a precipitate (by EDX) in Zircaloy-2, neutron-irradiated to 14.7×10^{25} n m^{-2} ~24.5 dpa. Orientation along the < 1120> direction. Adapted from Harte, A., Topping, M., Frankel, P., Jädernäs, D., Romero, J., Hallstadius, L., Darby, E.C., Preuss, M. (2017), Journal of Nuclear Materials, 487, 30-42.

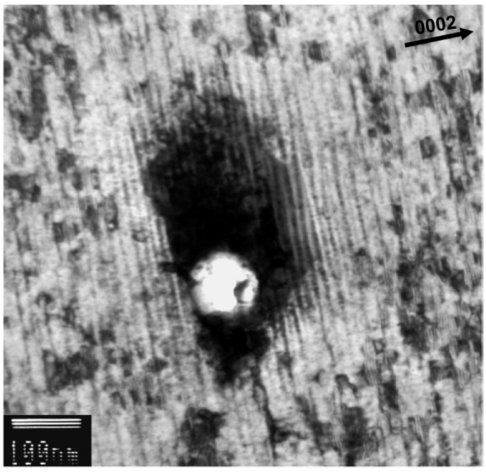

Figure 17 TEM observation of the precipitates on RXA Zircaloy-4 tubes after 6 cycles of PWR irradiation (21.0 x 10^{25} $n.m^{-2}$): precipitate under dissolution with depletion in Fe and high density of <c> component loops. Adapted from P. Bossis, B.Verhaeghe, S. Doriot, D. Gilbon, V. Chabretou, A. Dalmais, J.-P. Mardon, M. Blat, A. Miquet, Zircon. Nucl. Ind. Fifteenth Int. Symp. ASTM STP 1505 (2009) 430-456.

5.01.4.1.3 Evolution of Zr-(Fe,Cr,Ni) precipitates under light ion irradiation

When considering the literature, it can be noticed that only two of the three domains have been observed so far in the case of proton irradiation: progressive amorphization (intermediate temperature domain), and dissolution without amorphization (high temperature domain). Uniform amorphization (low temperature domain) was not reported with proton irradiation, probably because the irradiation temperatures investigated were not low enough to reach this domain. However, when conducting 1.5 MeV He irradiations at very low temperature (~100 K) [154], homogeneous amorphization was reported.

Proton irradiations conducted at 350°C on Zircaloy-4 samples show $Zr(Fe,Cr)_2$ Laves phase particles with an amorphous rim around a crystalline core [155] [156]. For the same dose and temperature [156], the $Zr_2(Fe,Ni)$ and Zr_2Fe particles were still fully crystalline.

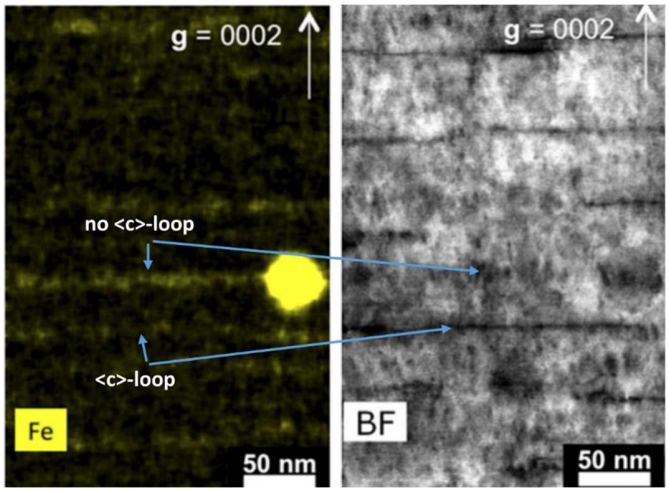

a) **b)**

Figure 18 Bright field a) and chemical maps b) extracted from a spectral image of a precipitate in Zircaloy-2, proton-irradiated to a dose of 7.0 dpa for Fe. Vector g = 0002, demonstrating the chemical segregation along basal planes similar to <c>-loops. Adapted from Harte, A., Seymour, T., Francis, E. M., Frankel, P., Thompson, S. P., Jädernäs, D, Romeo, J., Hallstadius, L., Preuss, M. (2015). Journal of Materials Research, 30(9), 1349-1365.

Under proton irradiation, as for neutron irradiation, the progressive amorphization of precipitates induces a dissolution of the alloying elements into the matrix. Harte *et al*. [157] measured by APT an increase in Fe and Cr content in the matrix after proton irradiation at 350°C, even for a low dose of 1.5 dpa (~$5x10^{-6}$ dpa/s). They observed also the segregation of Fe and Cr in rod-shaped features. Both the Fe and Cr content in rods decreased with the distance from the closest Fe-Cr precipitate. It was also seen that the Cr concentration of the rods decreases more rapidly than the Fe concentration with respect to radial distance, which is consistent with a lower mobility of Cr than Fe. These rod-shaped features were also observed by Topping et al. after proton irradiation at 450°C but not after proton irradiation at 280°C ($1.5x10^{-5}$ dpa/s) [91]. In addition, Harte *et al*. [90] observed after proton irradiation of Zircaloy-2 samples at 350°C ($6.7x10^{-6}$ dpa/s) segregation of Fe, Sn, Ni on features similar in size, shape and number density as Fe and Cr segregations for neutron irradiation at 280-330°C [153] (**Figure 16**).

The <c>-component loops appear usually more numerous at the vicinity of second phase particles which undergo a high loss of iron, and therefore appear correlated to iron re-distribution from the precipitates into the matrix [156]. The iron rejection into the matrix is seen to be much slower

during proton irradiation than in PWR. However, the measured <c>-loop line density was similar with proton and neutron irradiation [90] [120] [73]. As a consequence, <c>-component loop nucleation and growth seem locally correlated to iron dissolution into the matrix, but not directly correlated to the global amount of iron rejected [156]. Harte et al. [143] evidenced a chemical segregation (Fe,Sn,Ni) along the basal planes in a similar manner than <c>-component loops, in a Zy-2 irradiated with protons at 350°C. Some of these segregations correspond to <c>-loop trace, other do not (Figure 18). It is suggested that both vacancies, <c>-component-loops and alloying elements may cluster on basal planes by a cooperative rather than a sequential relationship [143].

5.01.4.1.4 Evolution of Zr-(Fe,Cr,Ni) precipitates under heavy ion irradiation

Only few studies using heavy ion irradiations are available in the literature. The amorphization of $Zr(Fe,Cr)_2$ and $Zr_2(Fe,Ni)$ precipitates in Zircaloy-4 during heavy ion irradiation was seen to be a uniform in the irradiation conditions tested [140] [155] [158] [151] [159]. The precipitates observed during *in-situ* experiments progressively loose, uniformly, their crystallinity [155] and the critical dose for amorphization increases with temperature [154]. The $Zr_2(Fe,Ni)$ particles are more resistant to irradiation than $Zr(Fe,Cr)_2$ [140] [159]. However, for low irradiation temperature (60°C) $Zr_2(Fe,Ni)$ particles are less resistant to irradiation than $Zr(Fe,Cr)_2$ [151]. No iron rejection was detected from the precipitates into the matrix (even at high doses such as 25 dpa and high temperature such as 600°C). No amorphous rim was evidenced at the periphery of precipitates whatever the doses and the irradiation temperatures (between 300 and 600°C). This means that only the "low temperature regime" was observed up to now, under heavy ion irradiation, as a result of the high damage rate (~1 x 10^{-3} dpa/s) [160]. A plausible explanation for the lack of progressive amorphization is that the diffusion process [161] [148] cannot occur at temperature below the glass temperature with such a high dose-rate.

5.01.4.1.5 Evolution of Zr-(Fe,Cr,Ni) precipitates under electron irradiation

Very few investigations have been conducted using *in situ* electron irradiation in a High Voltage Electron Microscope (HVEM). With such electron irradiation a sudden uniform amorphization is observed for both $Zr(Fe,Cr)_2$ and $Zr_2(Fe,Ni)$ particles in Zircaloy-2 and Zircaloy-4. The dose threshold for amorphization depends on the electron energy, on the dose-rate and on the irradiation

temperature. The dose to amorphization increases exponentially with irradiation temperature and is lower for higher dose-rate and higher electron energy [140]. The transformation occurs homogeneously throughout the precipitates, with no preferential amorphization at stacking faults. In neither of the two types of precipitates were any variations in chemical composition or precipitate dissolution observed. The critical temperature for amorphization was said to be lower than for neutron and ion irradiations. This phenomenon was partly attributed to the free surface of the thin foils that are sinks for irradiation defects [158] and also to the lack of cascade event during electron irradiation [140].

5.01.4.2 Behavior of (Zr,Fe,Nb) precipitates in Zr-Nb-Fe-(Sn) alloys

5.01.4.2.1 Evolution of (Zr,Fe,Nb) precipitates under neutron irradiation

$Zr(Fe,Nb)_2$ particles (Laves phases with HCP crystal structure) are commonly observed in quaternary alloys (Zr,Fe,Nb,Sn) such as Zirlo [162], E635 alloy [14] [117] [163] [164] [74] [165], O2-O8 alloys [166], or Q12 alloy [15]. These particles are also observed, in small amount, in Zr-1Nb alloys, such as E110 [117] or M5 [15] [73]. In addition to iron and niobium, small amount of chromium, of the order of 1.5 to 2 wt.%, can be found in these particles, even though chromium is only present as an impurity element (less than 100 ppm) in these alloys, because of the very low solubility of chromium in zirconium [162] [15] [167].

According to literature, $Zr(Fe,Nb)_2$ Laves phases loose very quickly their iron during neutron irradiation in usual service condition without amorphization (T_{irr} > 300°C), becoming Zr-Nb micro-crystallized highly faulted particles and then transform into βNb particles. This transformation into βNb particles was suggested a long time ago by Russian authors [14] [117] [163] [164] [74] [165] and was ascertained thanks to Y-NBED diagrams (Precession NanoBeam Electron Diffraction) [162] [143]. More recently, Markelov *et al.* [166] validated this transformation by providing diffraction diagrams on a partially transformed particle, showing a core retaining the initial HCP structure and a periphery with blocks of βNb precipitates (BCC structure). The transformation starts at the periphery of the particle and is seen to be complete after a dose of about 10 dpa [117] [15]. The allotropic transformation from a BCC to a HCP structure (and *vice-versa*) was described by Burgers in 1934 [168] and occurs when the iron content is too low to stabilize the HCP structure [117]. A concentration profile across a former Laves phase SPP

in a Zr1%Nb0.3%Sn0.1%Fe (wt%) alloy (**Figure 19**) [15], irradiated for two 18-month cycles in a PWR, exhibits a homogeneous profile in the core of the SPP with a drastic loss of iron in the core of the precipitate with a ratio Nb/Fe≈10 (in weight percent), while before irradiation this ratio was close to Nb/Fe≈2. Furthermore, the chromium content appears unchanged. On the periphery of the SPP, iron and chromium concentrations drop down to zero and only niobium and zirconium remain at the periphery of the particle.

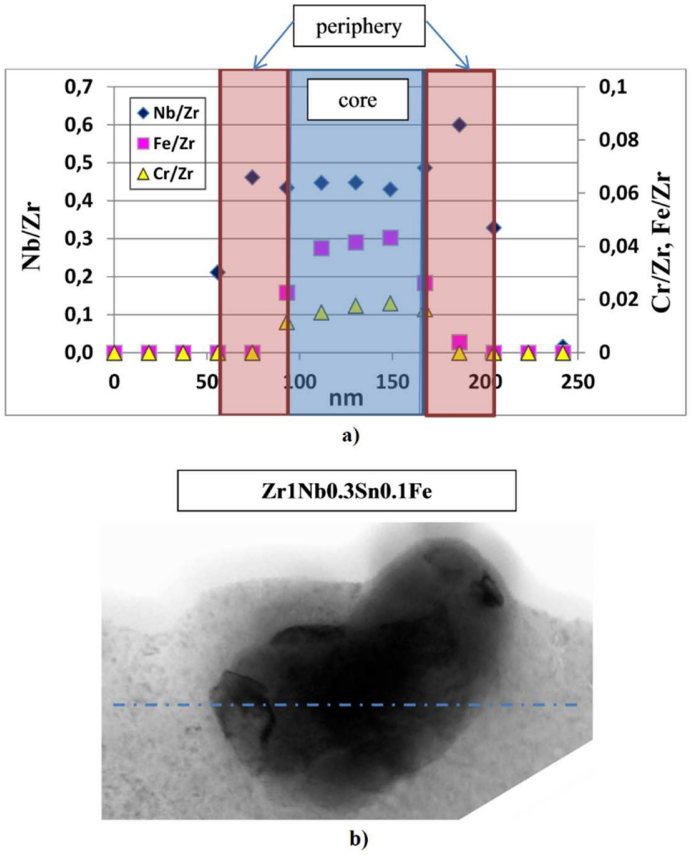

Figure 19 Concentration profile across a former Laves phase second phase particle in Zr1%Nb0.3%Sn0.1%Fe (wt%) alloy irradiated during two 18-month cycles, a) concentration profile (w%), b) micrograph. Adapted from Doriot, S., Verhaeghe, B., Soniak-Defresne, A., Bossis, P., Gilbon, D., Chabretou, V., Mardon, J.-P., Ton-That, M., and Ambard, A.,*" Zirconium in the Nuclear Industry: 18th International Symposium*, ASTM STP 1597, R. J. Comstock and A. T. Motta, Eds., ASTM International, West Conshohocken, PA, 2018, pp. 825–858.

Rare events of progressive amorphization of $Zr(Fe,Nb)_2$ SPPs are also reported in the literature [169] (see Figure 20) and some authors evidence a uniform amorphization of these precipitates under irradiation at the low temperature of 60°C [74].

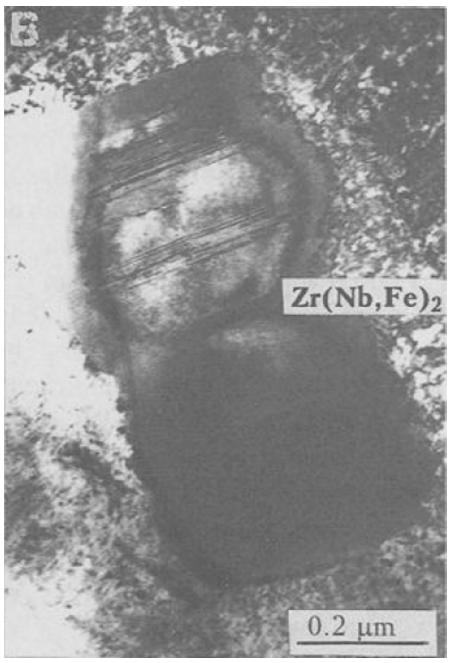

Figure 20 Microstructure of recrystallized E635 alloy irradiated to a fluence of $5x10^{25}$ n/m^2 at 350°C: a rare event of progressive amorphization of an intermetallic particle retaining crystalline core. Adapted from V. N. Shishov, A. V. Nikulina, V. A. Markelov, M. M. Peregud, A. V. Kozlov, S. A. Averin, S. A. Kolbenkov, A. E. Novoselov, Zircon. Nucl. Ind. Eleventh Int. Symp. ASTM STP 1295 (1996) 603-622.

Some authors conclude from these observations that the three temperature domains observed with the $Zr(Fe,Cr)_2$ particles also exist for the $Zr(Fe,Nb)_2$ second phase particles [156] [157]. Nevertheless, determination of the critical temperature (if it exists) is not possible because of the lack of data between 60°C and 300°C. In addition, the composition of these particles varies in a large domain of concentrations (25-36 at. % Fe, 29-41 at. % Nb) [170]. This probably induces variabilities in their behavior and could explain the coexistence of amorphized and of non-amorphized second phase particles for the same irradiation conditions as reported by some authors [169]. In addition, the initial phase composition, and therefore phase designation, becomes sometimes difficult in *post-mortem* analyses, especially when there is incomplete report prior to

irradiation [169] [157]. Furthermore, it is surprising to observe such a different behavior of $Zr(Fe,Nb)_2$ precipitates, compared to $Zr(Fe,Cr)_2$, in similar neutron irradiation conditions [156] [157]. It seems that $Zr(Fe,Nb)_2$ precipitates are in the "high temperature" domain while $Zr(Fe,Cr)_2$ particles are in the "intermediate temperature" domain in the same PWR irradiation conditions [156]. This difference may be explained by their difference in composition that influences the amorphization resistance of the particles [149]. Nevertheless, a significant difference in the behavior of $Zr(Fe,Cr)_2$ and $Zr(Fe,Nb)_2$ particles is observed in the "high temperature domain" ; the latter undergoes a structural transformation whereas the former does not [156] [157]. The drastic loss of iron from the $Zr(Fe,Nb)_2$ precipitates is attributed to the high diffusivity of iron compared to niobium in zirconium whereas, in the case of $Zr(Fe,Cr)_2$, the difference in diffusivity between iron and chromium is lower [156]. The structural transformation may be explained [157] by a much greater diffusion coefficient in α-Zr for Cr relative to Nb [171] and by the β-stabilizing effect of Nb in Zr.

If the iron content is high enough (about 2% in weight) a cubic phase $Zr(Fe,Nb)_4Fe_2$ may be observed in some quaternary alloys such as 3R alloy [113], Zr1%Nb0.25%Sn0.35%Fe alloy (wt %) [172], Zr1%Nb0.3%Sn0.2%Fe alloy [15], the Russian E635 alloy [14] [169] [117] [74] [163] or the O2, O5, O8 alloys [166]. This phase was called T-phase by the Russian team and has a FCC lattice and the composition of 60Zr-10Nb-30Fe (at.%) [117]. At low dose (few dpa) no noticeable microstructural or micro-chemical change (no composition gradient) was observed in these particles under irradiation [113] [74]. A review by Harte et al. [157] summarizes the behavior of these precipitates at higher doses, under neutron irradiation: the cubic phase $(Zr,Nb)_2Fe$ retains its crystalline core and shows a polycrystalline microstructure at the particle periphery that is likely Nb-rich platelets. This behavior was described in several publications [113] [163] [117] [115]. These particles were analyzed by EDX on extraction replica by the Russian team and on thin foils by the French team. In spite of the scatter of measurements before and after irradiation (Fe at. % between 24 and 29), the authors concluded that no compositional change occurred in the crystalline core during irradiation. But the iron content drops down drastically in the polycrystalline particle on periphery [14] [113] [117] (Figure 21).

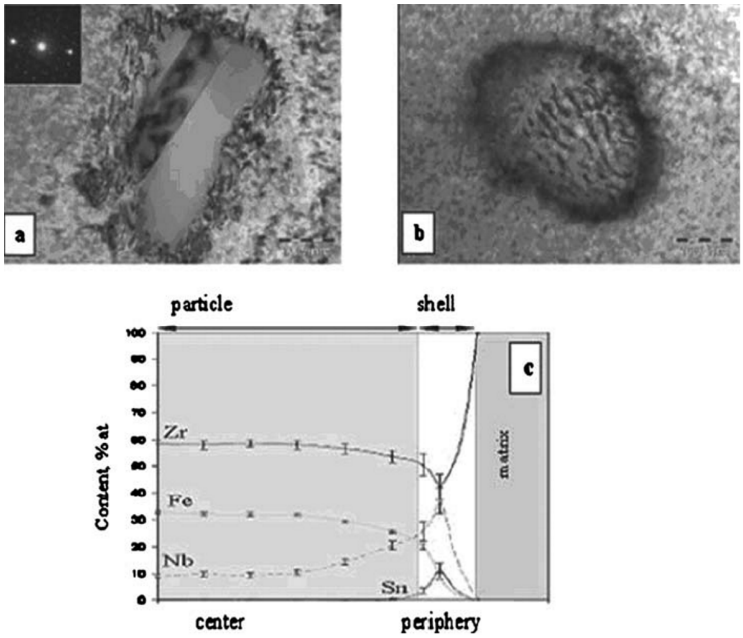

Figure 21 T-phase precipitates $(Zr,Nb)_2Fe$ in E635 type alloy (Zr-0.7Nb-0.3Fe,.1.2 Sn) irradiated to F = 3.6 x10^{26} m^{-2} , a) plate precipitates at the periphery; (b) T-phase rim; (c) element distribution within particle and on boundary with matrix. Adapted from V.N. Shishov, Zircon. Nucl. Ind. Sixteenth Int. Symp. ASTM STP 1529 (2011) 37-66.

It can be concluded that the irradiation induces a significant dissolution of iron from the Zr-(Fe,Cr,Nb) precipitates into the matrix. However, no evidence of a significant Nb dissolution is pointed out in the literature. As in Zircaloys, the <c>-component loops appear more numerous at the vicinity of second phase particles that undergo a high loss of iron (Figure 22) suggesting that <c>-loop formation is correlated to iron re-distribution from the precipitates into the matrix. However, although the iron rejection occurs in a much faster way in the quaternary alloys than in Zircaloy-4 in PWR conditions, the <c>-component loop linear density in these quaternary alloys is much lower than that in Zircaloy-4 [15]. Thus, it can be concluded that there is a correlation between the iron rejection from the precipitates into the matrix and the <c>-component loop nucleation in quaternary alloys and in Zircaloy-4, but this correlation is very complex and not elucidated yet [162].

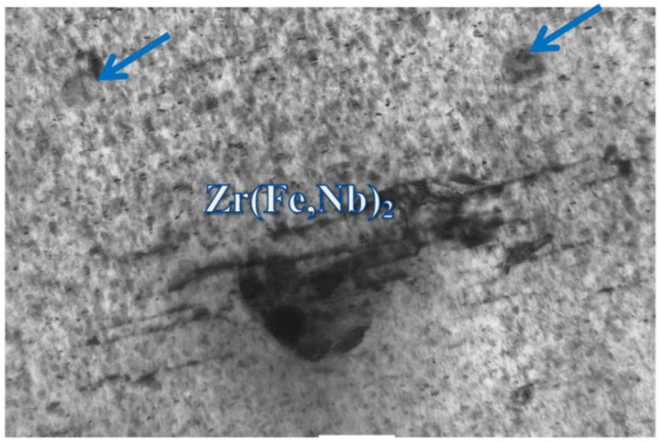

Figure 22 Second phase particles and <c>-component loops. Micrographs with g=0002 diffracting vector. Zr1%Nb0.3%Sn0.1%Fe (wt%) alloy irradiated during two 18-month cycles. Arrows indicate location of βNb particles. Adapted from Doriot, S., Verhaeghe, B., Soniak-Defresne, A., Bossis, P., Gilbon, D., Chabretou, V., Mardon, J.-P., Ton-That, M., and Ambard, A.,*" Zirconium in the Nuclear Industry: 18th International Symposium*, ASTM STP 1597, R. J. Comstock and A. T. Motta, Eds., ASTM International, West Conshohocken, PA, 2018, pp. 825–858.

5.01.4.2.2 Evolution of (Zr,Fe,Nb) precipitates under proton irradiation

Very few authors have studied the behavior of $Zr(Fe,Nb)_2$ under proton irradiation. Francis et al. [162] irradiated a Low Tin ZIRLO™ with protons at the temperature of 350°C ($7.5x10^{-6}$ dpa/s). In these proton irradiation conditions the $Zr(Fe,Nb)_2$ Laves phases evidences the same behavior as in PWR irradiation conditions with a drastic loss of Fe and a transformation into βNb. In the same irradiation condition and in the same material, rod-shaped Fe-rich precipitates (few nanometers) are observed after irradiation [173] as seen in Zircaloy-2 after proton irradiation [157] [91]. At the same irradiation temperature, but with a much higher dose-rate (~$2x10^{-5}$ dpa/s) the Laves phases were found to be totally amorphised after irradiation [156] (Figure 23). Concentration profiles across amorphised Laves phases show a uniform preferential dissolution of iron out of the precipitate increasing with the dose. In addition, there is some indications that iron accumulates in the matrix adjacent to the Laves phase after irradiation. In the work of Doriot *et al*. [156], at the dose of 19 dpa, amorphised particles undergo only a moderate decrease of their iron content. Nevertheless, <c>-component loops appear more numerous at the vicinity of Laves phase particles

and the <c>-component loop linear density is similar to the <c>-component loop density after neutron irradiation at the same dose. Thus it can be concluded once again that the correlation between the iron rejection from the precipitates to the matrix and the <c>-component loop nucleation is very complex.

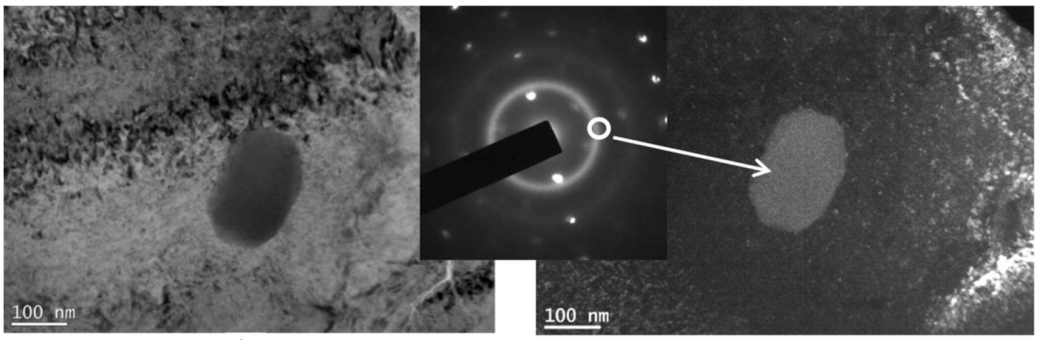

Figure 23 Fully amorphised Laves phase in the 2 MeV proton irradiated M5 alloy at 350°C, 8.1 dpa, a) Bright Field, b) Dark Field. Adapted from S. Doriot, ∗, F. Onimus, D. Gilbon, J.-P. Mardon, F. Bourlier, "Transmission electron microscopy study of second phase particles irradiated by 2 MeV protons at 350 °C in Zr alloys", Journal of Nuclear Materials 494 (2017) 398-410.

5.01.4.2.3 Evolution of (Zr,Fe,Nb) precipitates under heavy ion irradiation

Russian authors [174] irradiated an E635 alloy with Zr^{6+} ions (390°C, 10^{-3} dpa/s). The iron content of the particles, analyzed on extraction replica dropped down from about 30 at.% to 3-10 at. % after 30 dpa irradiation. Thus, there is an iron dissolution after ion irradiation at 390°C, but it is not as drastic as during neutron irradiation. As a consequence an increase of Fe content and Fe-rich nanoclusters are evidenced in the Zr matrix after ion irradiation [175]. It is also observed [174] that no <c>-component loop appears up to 30 dpa in this alloy while they are seen at lower doses in alloys with a lower iron content (E110 and E125).

5.01.4.3 Evolution of native β-Nb precipitates in Zr-Nb alloys

5.01.4.3.1 Evolution of native β-Nb precipitates under neutron irradiation

In Zr-Nb alloys, with Nb content of 1% (in weight) or higher, the HCP α–Zr matrix contains Nb in solid solution and BCC βNb precipitates are present, according to the binary phase diagram. Zr-1Nb alloys, such as E110 [117] [14] [163] and M5 [113] [73], are characterized by a dense (~10^{20} m^{-3}) and homogenous highly refined dispersion of βNb precipitates in fully recrystallized grains. The chemical compositions reported in the literature for βNb precipitates (~85 at. % Nb), usually show no Fe, but, in some cases, up to 4 at.% Fe can be observed [157]. In the quaternary alloys described above (see paragraph 4.01.1.4.2), the βNb precipitates coexist with (Zr,Fe,Nb) particles, and in a low-tin Zirlo Francis et al. [162] noticed a segregation of iron onto the βNb particle interface by EDX spectra line (> 6 wt.%). In non-equilibrium states, the βNb precipitates can coexist with the metastable βZr and ω phases [157] as in the Russian E125 alloy (Zr2.5Nb) [169] [165] or in the Canadian Zr2.5Nb alloy [68] [176].

Observations of βNb phase particles after neutron irradiation highlight the noteworthy irradiation tolerance of this phase: no crystallographic change in βNb particles is observed [176] neither for high irradiation doses [113] [73] [117] [74] [14] [162], nor for very low irradiation temperatures (288 K) [74] [163]. In Zr1%Nb alloys the diameter of βNb particles was seen to increase slightly with irradiation dose [113] [73] [74] [164] while their number density exhibited a slight decrease at high fluence. Nevertheless the mean size of the coherent diffracting domains analysed by Synchrotron X-Ray Diffraction in Transmission mode (T-XRD) of these particles drops from 33 (±2) nm before irradiation down to 11 (±1) nm after irradiation [73]. As concluded by the authors, this phenomenon could be due to irradiation defects and is consistent with the granitic aspect of the precipitates observed by TEM (**Figure 24**). In addition, the iron segregation observed at the interface of these precipitates was found to be greatly reduced after irradiation [162].

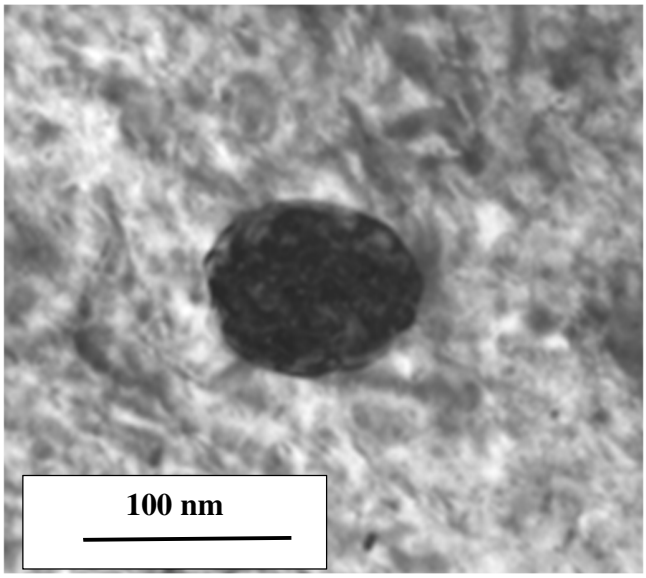

Figure 24 TEM micrographs of βNb in M5 irradiated during 6 PWR cycles. Granitic aspect. Adapted from Doriot, S., Verhaeghe, B., Béchade, J.-L., Menut, D., Gilbon, D., Mardon, J.-P., Cloué, J.-M., Miquet, A.,and Legras, L.*," Zirconium in the Nuclear Industry: 17th International Symposium*, STP 1543, Robert Comstock and Pierre Barberis, Eds., pp. 759-799, ASTM International, West Conshohocken, PA 2014.

EDX microanalysis (on extraction replica and on thin foils) [117] [73] and Synchrotron X-Ray Diffraction [73] show a slight decrease of Nb content in βNb particles. In a non-equilibrium Zr2.5Nb alloy [169] [165] the Russian authors observe on the contrary a slight increase in the Nb content of the βNb particles in order to reach the equilibrium composition.

Doriot et al. [113] noticed that the βNb second phase particles contain after irradiation about half of the total Nb of the alloy, as before irradiation. They concluded that the decrease of Nb content in the βNb precipitates does not induce a dissolution of Nb into the matrix. In addition, it can be noticed that no <c>-component loop decorate the vicinity of the βNb particles (Figure 24). Furthermore, it was shown that the ω phase, obtained in Zr–2.5Nb by transformation of the β-Nb after extrusion, disappears and transforms into β-Nb [68].

5.01.4.3.2 Evolution of native β-Nb precipitates under proton irradiation

Francis *et al.* [162] (Zirlo, $7.5x10^6$ dpa/s) and Doriot *et al.* [156] (M5, $2x10^{-5}$ dpa/s, 19 dpa) observed that the native βNb precipitates retained their BCC crystallographic structure after proton irradiation at 350°C. The Fe enrichment observed in the core of the precipitates before irradiation disappears after proton irradiation [162]. In addition, Yu et al. [177] observed a partial dissolution of the native precipitates in a Zr-1%Nb alloy irradiated at the dose of 1 dpa at the temperature of 350°C with 2 MeV protons. This dissolution was not observed in a Zr-0.5%Nb alloy. A slight decrease of the Nb content of the native particles was also noticed.

5.01.4.3.3 Evolution of native β-Nb precipitates under heavy ion irradiation

He *et al*. conducted *in situ* Kr^{2+} ion irradiations on a Zr1%Nb and a Zr2.5%Nb alloys at different temperatures between 50K and 873K [178]. At the high flux of 10^{-3} dpa/s and at the low temperature of 50K the particles retained their crystallinity up to 20 dpa, showing, once again, the exceptional stability of these particles under irradiation. He *et al*. [178] observed (but only at the temperature of 623K) a behavior similar to neutron [73]: a moderate lowering of the Nb content with an increase of the size of the particles, the total Nb content of the particles remaining unchanged. This behavior was attributed to the formation of a "mixing zone" of Zr and Nb atoms at the periphery of the particles due to the cascades, seen at the broadened EDX profiles (See **Figure 25**). At low temperature the recombination rate of vacancies and interstitials in the cascade is high, and at high temperature the back Nb diffusion is higher: thus in both cases the phenomenon of "mixing zone" is constrained. The increase of the size was seen preferentially along the <c> direction. The average diameter of about 50 nm observed after about 5 dpa in PWR was not reached after a dose of 40 dpa by ion irradiation: therefore the increase in size and consequently the lowering in Nb content appear slower during ion irradiation compared to neutron irradiation. No Nb transfer from the particles into the matrix was noticed.

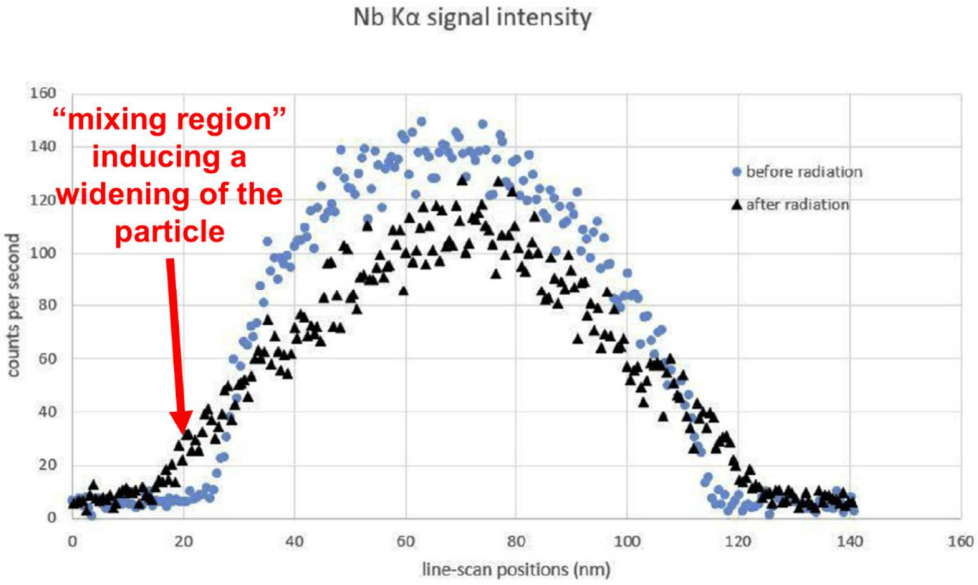

Figure 25 Typical EDX line-scan profile of the Nb Kα signal for precipitate irradiated at 623K. Adapted from Guanze He, Junliang Liu, Kexue Li, Jing Hu, Anamul Haq Mir, Sergio Lozano-Perez, Chris Grovenor, Investigating the stability of Second Phase Particles in Zr-Nb alloys under irradiation, Journal of Nuclear Materials 526 (2019) 151738.

5.01.4.4 Irradiation effects in Zr–Nb alloys: Enhanced precipitation under irradiation

5.01.4.4.1 Enhanced Nb precipitation under neutron irradiation

In binary Zr–Nb alloys (Zr–1% Nb and Zr–2.5% Nb), the microstructure is usually in a metastable state due to the thermomechanical processing in the upper α range or in the α + β domain. Indeed, at this relatively low temperature (around 580 °C), the atomic mobility is low and the equilibrium state cannot be reached in a reasonable time. After cooling, the matrix is therefore supersaturated in Nb and the composition of secondary phases (Nb rich) still corresponds to the high-temperature chemical composition. It is indeed shown by Toffolon-Masclet *et al.* [179] that a Zr–1% Nb–O alloy that has undergone a final heat treatment at 580 °C for a few hours can still evolve toward its thermodynamic equilibrium after 10000 h of heat treatment at 400 °C.

Under irradiation, it is observed that the microstructure of Zr–Nb alloys is not stable and very fine Nb-rich precipitates, with diameter of a few nanometers, are observed in very high density (**Figure 26**). This precipitation of Nb-rich precipitates from the supersaturated matrix is evidenced in any type of binary alloys after neutron irradiation: in Zr1%Nb such as M5 [113] [73] and E110 [14]

[169] [165] [74] and in Zr2.5% Nb [180] [181]. These nano-precipitates are also present after neutron irradiation of some quaternary alloys (Zr-Fe, Nb, Sn) such as 3R [113], Q12 [15], E635 [117] or O2-O8 [166]. Simultaneously to the formation of these precipitates, a noticeable decrease of Nb content occurs in the matrix [115]. Another interesting observation is the fact that these nano-precipitates are not more numerous at the vicinity of native βNb. This is consistent with the fact that no significant Nb dissolution out of the native βNb particles occurs since the Nb diffusion rate in Zr is very low [165].

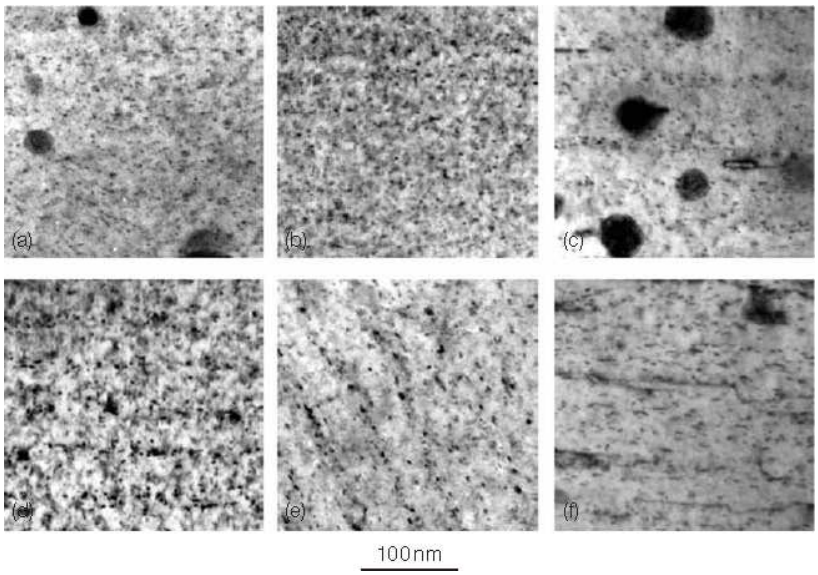

Figure 26 Micrographs of needle-like radiation-enhanced precipitation: (a) M5 2.1 × 10^{25} n m^{-2}, (b) Zr–1% NbO 2.8 × 10^{25} n m^{-2}, (c) M5™ 3.6 × 10^{25} n m^{-2}, (d) Zr–1% NbO 5.7 × 10^{25} n m^{-2}, (e) Zr–1% NbO 8.2 × 10^{25} n m^{-2}, and (f) M5 13.1 × 10^{25} n m^{-2}. Reprinted, with permission, from *J. ASTM Int.*, copyright ASTM International, 100 Barr Harbor Drive, West Conshohocken, PA.

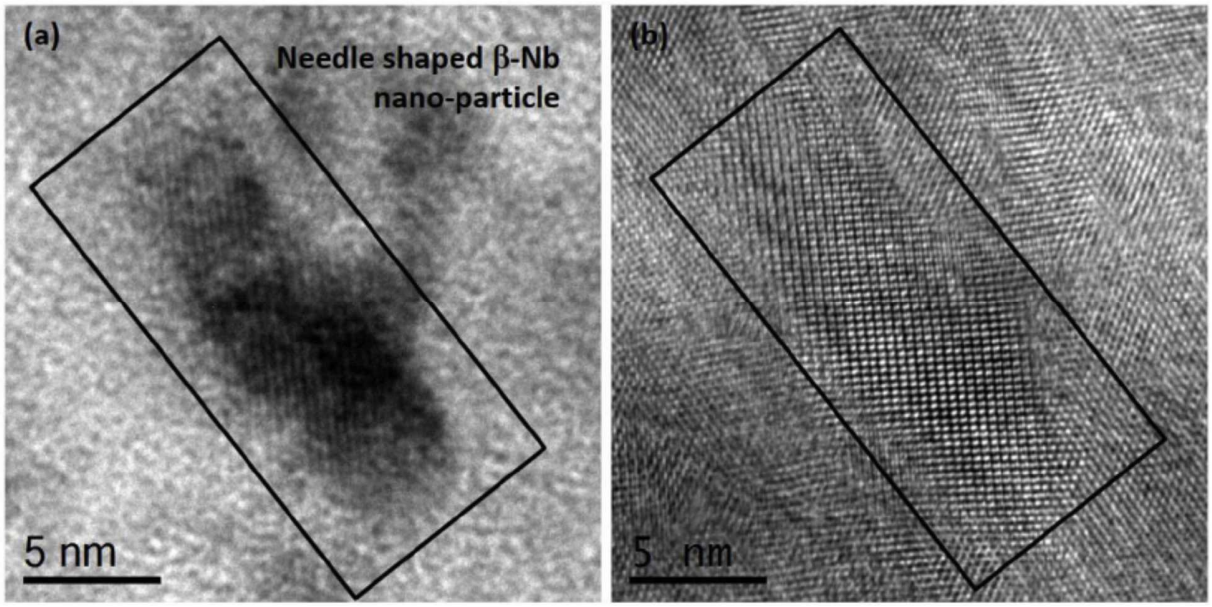

Figure 27 : Orientation relationships of a needle-shaped precipitate : (a) bright-field micrograph, (b) high-resolution micrograph. Adapted from Ribis, J., Doriot, S., & Onimus, F. (2018). Journal of Nuclear Materials, 511, 18-29.

This precipitation is due to an enhanced mobility of Nb atoms under irradiation because of the very high vacancy concentration created by irradiation. This allows the rapid evolution of the microstructure toward its thermodynamic equilibrium, leading to precipitation of very fine Nb-rich precipitates.

These particles are thermodynamically stable [113] [181], which is consistent with a mechanism of precipitation due to irradiation-enhanced diffusion controlled by migration of non-equilibrium irradiation-induced point defects [182] [183] [184]. The small size of these precipitates, however, makes it difficult to clearly characterize them by TEM [117] but for a long time they were supposed to be βNb particles because of their thermodynamic stability, with a composition of about 55-60 at. % Nb (the composition of native βNb under irradiation) [14] [113]. The composition of the particles was ascertained by EDX [163] using extraction replica and by T-XRD using Synchrotron facility [73]. The BCC crystallographic parameters were validated by T-XRD measurements [73] and more recently by high resolution TEM (HRTEM) analyses (**Figure 27**) [185] [186].

Furthermore, it was shown that the βNb nano-particles display an unrelaxed tetragonal structure rather than a perfect cubic structure owing to interfacial strain effect [186].

The particles were evidenced at very low fluence corresponding to less than 1.5 dpa [185]. A measurement by TEM of the width and length of these particles versus fluence was plotted for E110 [185] and for M5 [113]. For both Zr1%Nb alloys, the two parameters were rapidly increasing up to a fluence corresponding to about 5 dpa to reach saturation for higher fluence. The average length saturated at about 7 nm. This particle size enhancement during irradiation was also observed by SANS [113]. The Nb-enriched particles looked almost circular for the low dose of 1 PWR cycle. For higher fluence they became elongated in the direction close to the basal plane trace with prism-plane foil orientation [181] [117] [113] [73] [185] [186]. This shape could be explained by the attempt to minimize the stress field due to matrix/precipitate misfit and by the anisotropy in diffusivity of irradiation-induced point defects [183]. According to Ribis *et al.* [186] the elongated shape of the particle, in the basal plane, was explained by the existence of an invariant line along the [11-20]//[111] type direction. The invariant line may be visualized as a row of atoms common to both structures. In addition, precipitates tend sometimes to concentrate in spaced layers parallel to the basal plane separated by ~50 nm [117] [73] [186]. According to Shishov and Doriot *et al*. this phenomenon could be related to external stress. An increase in iron and tin content promote this particle ordering [117]. The authors measured a density of about 1-2x 10^{22} m^{-3} whatever the fluence [74] [163] [113] [73] [185]. Nevertheless, it was shown by Gurovich *et al.* [185] that for small fluences (~1.5 dpa), the number density of these fine precipitates reaches a maximum. This was explained by the authors by the initial stage of fine precipitates formation with their subsequent coalescence.

5.01.4.4.2 Enhanced Nb precipitation under electron irradiation

At higher temperature (450-500°C) and much lower dose rate (~10^{-6} dpa/s) a precipitation of βNb needle-like precipitates is observed in a Zr2.5Nb alloy, after 10 MeV electron irradiation [187].

5.01.4.4.3 Enhanced Nb precipitation under light ion irradiation

Some authors did not observe any nanometric precipitation of βNb after 2 MeV proton irradiation of M5 alloy [156]. According to these authors, the lack of radiation-enhanced precipitation could be due to the high dose-rate used (~$2x10^{-5}$ dpa/s, 350°C) and therefore to the low irradiation duration that does not allow the diffusion process to take place at this temperature. At higher temperature (450-500°C) and much lower dose rate (~10^{-6} dpa/s) a precipitation of βNb needle-like precipitates is observed in a Zr2.5Nb alloy, after 3.5 MeV proton irradiation [188].
Topping *et al*. [91] observed Nb-rich nanoclusters (diameter~2 nm) after 2 MeV proton irradiation at a lower and at a higher temperature (280°C and 450°C) and with a similar dose-rate as Doriot *et al.* in a low tin Zirlo. Similar features were also observed by SAT in the same material at 350°C with dose-rates of about 10^{-6} - 10^{-7} dpa/s [173] [177]. These nanoclusters contained about 30 at.% Nb and 10 at.% Fe [173] [177] and it is not clear whether they are similar to the needle-like particles observed after neutron irradiation.

A precipitation of Nb-rich platelets was also observed after proton irradiation of Zr1%Nb alloys at 350°C [177]. These platelets were quite bigger (135 nm long and 27 nm wide) than the needle-like particles observed after neutron irradiation. They followed [177] the well-known Burgers crystallographic relation with the α matrix [189]. This relation induces the occurrence of six equivalent precipitate crystallographic orientations or variants [190]. Such a precipitation looks similar to the V-rich βTi particles that appeared in the α-matrix of Ti-6%Al-4%V alloys after neutron, proton and ion irradiation [191] [190] [192] [193] [194]. A lowering of the matrix Nb content was also reported [177].

5.01.4.4.4 Enhanced Nb precipitation under heavy ion irradiation

Needle-like Nb-rich precipitation is usually not reported after ion irradiation [154] [178] [119] [120] [122]. Motta et al. [154] assume that this precipitation is controlled by the specific diffusion length ($<\chi> = \sqrt{D_{Nb}\, T_{irr}}$, where D_{Nb} is the diffusion coefficient of Nb and T_{irr} the irradiation temperature). They calculated $<\chi>$ for different kinds of irradiations between 400 and 450°C). $<\chi>$ is smaller for heavy ions than for electrons and protons in thin foils, where surfaces are sinks for point defects. In addition the irradiated thickness spreads only on few hundred nanometers and

is near the surface of the sample which is a sink for point defects [119]. A fine precipitation is nevertheless observed by Novikov *et al.* [174] after Zr^{6+} irradiation at 390°C 24 dpa (10^{-3} dpa/s) but no detail were provided on these particles. Matsukawa et al. [175] also observed by APT, Nb-rich nanoclusters after Ni^{3+} ion irradiation of a J-Alloy (573K) at a dose lower than 0.1 dpa. A lowering of the matrix Nb content is also reported by these authors.

5.01.5 Postirradiation mechanical behavior

During in-reactor use in normal operating conditions, the mechanical behavior of zirconium alloys is significantly altered because of fast neutron irradiation and hydriding associated to water oxidation. This last phenomenon strongly decreases the failure properties of the material. In the following the impact of hydriding on the mechanical behavior of zirconium alloys, a subject in itself, is not discussed. Only the effect of neutron irradiation is described, either using samples tested in inert environment or samples with low enough hydrogen content.

5.01.5.1 Mechanical behavior during tensile testing

5.01.5.1.1 Irradiation hardening: macroscopic behavior

As for many other metals, zirconium alloys exhibit strong hardening after neutron irradiation. It is indeed observed by numerous authors [195] [196] [197] [198] [199] [200] [201] [202] [203] [204] [205] [206] [207] [208] [209] [210] [72] [211] and reviewed in the past by several authors in [28] [135] [212] that the yield stress (YS), as well as the ultimate tensile strength (UTS), of both recrystallization-annealed (RXA) and stress-relieved annealed (SRA) zirconium alloys are significantly increased by neutron irradiation (**Figures 28, 29 and 30**).

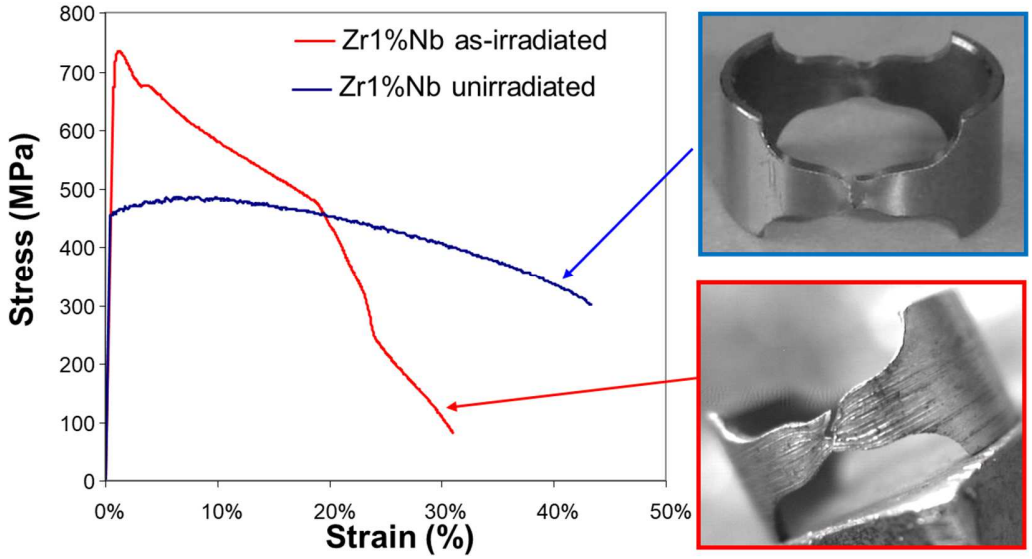

Figure 28 : Engineering stress-strain curves obtained during ring tensile tests performed at room temperature on as-irradiated and unirradiated Zr-1 % Nb specimens. Adapted from Bourdiliau,

B., Onimus, F., Cappelaere, C., Pivetaud, V., Bouffioux, P., Chabretou, V., & Miquet, A. (2012) Zirconium in the Nuclear Industry: 16th International Symposium. ASTM International.

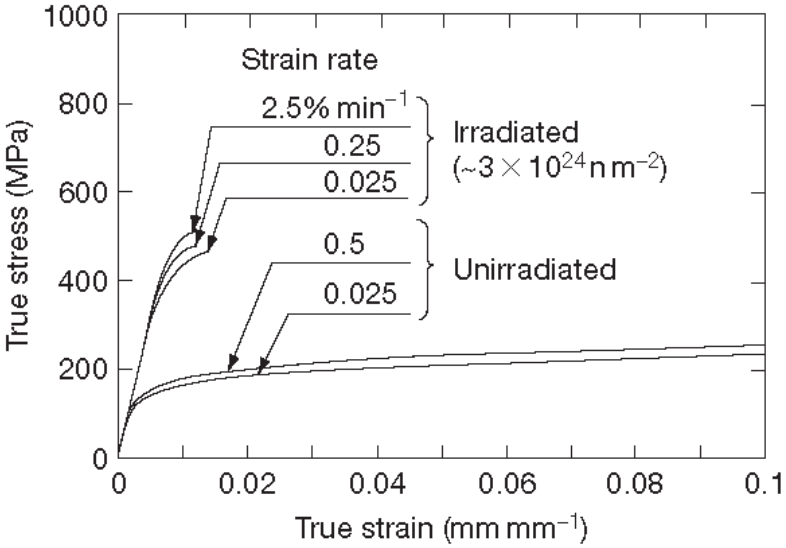

Figure 29 Stress–strain curves indicating the effect of irradiation and strain rate of RXA Zy-2 measured during uniaxial tensile test at 616 K. Reprinted, with permission, from *Seventh International Symposium on Zirconium in the Nuclear Industry*, Strasbourg, France, June 24–27, 1985, copyright ASTM International, 100 Barr Harbor Drive, West Conshohocken, PA 19428.

Microhardness tests done after neutron irradiation also prove this phenomenon [213] [214] [215] [216] [108] [210]. The irradiation-induced hardening (defined as $\Delta\sigma = \sigma_{irr} - \sigma_{unirr}$ where σ_{unirr} is the yield stress of the unirradiated material and σ_{irr} the yield stress of the irradiated material) increases rapidly for fluences below 1 × 10^{24} n m^{-2} (E > 1 MeV), at irradiation temperatures between 320 and 360 °C, but saturates above 1 × 10^{24} n m^{-2} (E > 1 MeV) and little change occurs from 1 × 10^{24} up to 1.5 × 10^{25} n m^{-2} (E > 1 MeV) [197]. It is however to be noticed that some authors do not find a clear saturation of the irradiation-induced hardening for fluences up to 1.5 × 10^{25} n m^{-2} and irradiation temperatures between 320 and 360 °C [197] [202]. Although the YS (and UTS) of SRA Zr alloys is significantly higher than the YS of RXA Zr alloys before irradiation, the YS of both alloys, measured after high irradiation doses, at saturation, become close [28] [195] [212].

According to Higgy and Hammad [197], and reviewed by Douglass [28], as the irradiation temperature increases from temperatures below 100 °C up to temperatures between 320 and 360

°C, the irradiation-induced hardening decreases. According to these authors, this shows that the accumulation of damage decreases as the irradiation temperature increases, presumably due to recovery during irradiation.

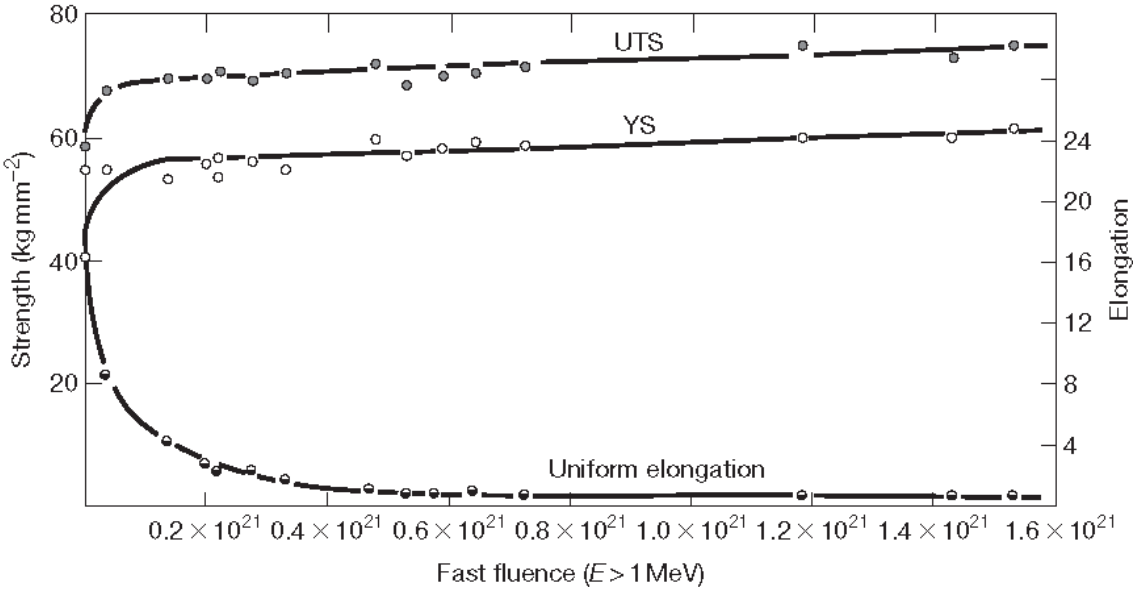

Figure 30 The effect of fast fluence (given in n cm^{-2}, E > 1 MeV) on the room temperature tensile properties of RXA Zircaloy-4 for irradiation temperature between 320 and 360 °C. Adapted from Higgy, H. R.; Hammad, F. H. *J. Nucl. Mater.* **1972**, *44*, 215–227.

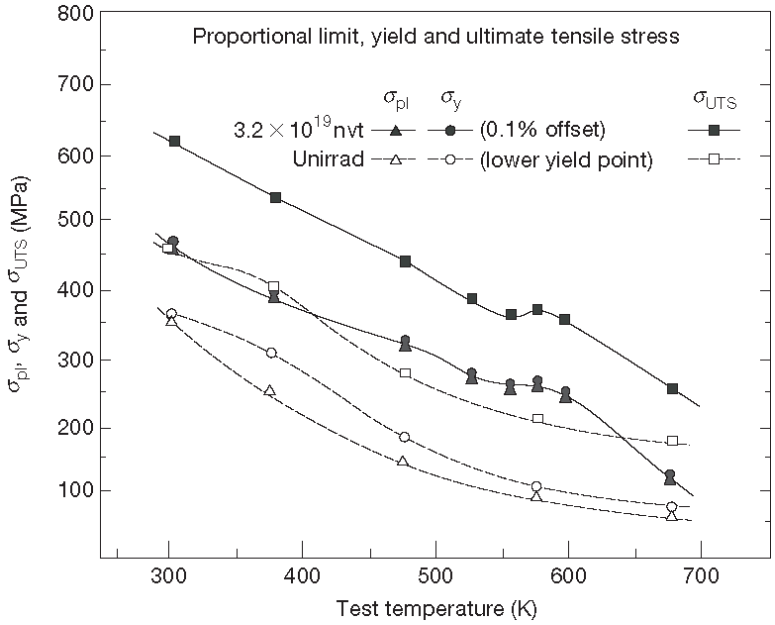

Figure 31 Proportional limit, yield, and ultimate tensile stress as a function of temperature for unirradiated and irradiated annealed (RXA) Zircaloy-2, tested at a strain rate of 1.1×10^{-4} s^{-1}. Adapted from Onchi, T.; Kayano, H.; Higashiguchi, Y. *J. Nucl. Mater.* **1980**, *88*(2–3), 226–235.

The chemical composition seems to play a secondary role in the irradiation-induced hardening compared to the effect of the metallurgical state (SRA vs. RXA). The oxygen content is nevertheless shown to have a slight effect on the irradiation-induced hardening. Indeed, Adamson and Bell [213] have shown using microhardness tests that the irradiation-induced hardening ($\Delta\sigma$) is higher for RXA Zy-2 alloy with high oxygen content (1800 ppm) than in the case of an RXA Zy-2 alloy with low oxygen content (180 ppm).

It can also be noticed that the test temperature seems to have only a small influence on the irradiation-induced hardening ($\Delta\sigma$), for a given irradiation temperature, up to a test temperature of 400 °C. Indeed, as reported by Onchi *et al.* [201] (**Figure 31**), the YS of both irradiated and unirradiated RXA Zy-2 decreases with the test temperature, the decrease being only slightly lower for the irradiated specimens between 20 and 300 °C. However, beyond a test temperature of 400 °C, a significant decrease of the irradiation hardening occurs due to the recovery of the irradiation damage during the test.

By using proton irradiation allowing reaching relatively thick irradiation depth of 30 µm, Zu et al. [155] have been able to measure the radiation induced hardening using low load (10 g) micro-hardness tests at room temperature.
Recently, several authors have conducted heavy ion irradiation and small-scale testing experiments such as micro-pillar [217] [218] or nano-indentation in order to measure radiation induced hardening [219] [220] [221]. These authors have been able to measure the nano-hardness increment resulting from the charged particle irradiation on a very thin layer.

5.01.5.1.2 Irradiation hardening: mechanisms and modelling

It is widely agreed [135] [212] that the irradiation-induced hardening in zirconium alloys is the result, as for many other metals, of the creation of a high density of small point-defect clusters that act as obstacles for dislocation glide. As described earlier, the point-defect clusters in zirconium alloys consist mainly of small prismatic loops, with Burgers vector lying in the $\langle a \rangle$ direction and the habit plane close to the prismatic plane of the hcp crystal lattice. Several authors have discussed that dislocations interact with irradiation-induced dislocation loops through their long-range stress field [222] [223] and also through contact interactions, which can lead to junction creation that can be strong obstacles to dislocation motion [224] [225] [226]. Several authors have investigated in more detail the junction formation between dislocations and loops in zirconium alloys. Particularly, Carpenter [227] has considered the mechanism proposed by Foreman and Sharp [225] and he applied it to the prismatic glide in zirconium alloys. He has shown that an edge dislocation gliding in the prismatic plane that is pinned by a loop can annihilate the loop. More recently, it has been discussed that the junctions between the loops and the dislocations gliding in the basal plane are always glissile, whereas they are sessile when the dislocations glide in the prismatic plane [228] [229]. This phenomenon could then lead to a lower hardening of the basal slip system compared to the other slip systems. MD computations [230] have been undertaken in order to gain a better understanding of the interaction mechanisms between dislocations and loops in zirconium alloys. It is shown that not all the slip systems are affected in the same way by the presence of the $\langle a \rangle$ type loops, the basal slip system being less hardened than the prismatic slip system, for instance. Recently, more complex MD simulations have been undertaken [231] [232]. As for FCC metals [233] it is shown that the strongest reaction is the interaction between a screw dislocation gliding in the prismatic plane and a loop

which creates a helical turn on the dislocation. These simulations thus confirm that loops can act as strong pinning point for screw dislocations gliding in the prismatic plane thus explaining the radiation induced hardening.

In order to reach larger length scales and more complex configurations, Dislocation Dynamics simulations have also been conducted to study dislocation and loop interactions [234]. Furthermore, these dislocation dynamics simulations have been compared with experimental observations of dislocation and loop interaction using in situ straining inside TEM [235]. In that case, dislocations gliding in the pyramidal plane were mainly observed. For some configuration, a significant pinning of the dislocation was observed whereas other configurations lead to the annihilation of the loops.

The hardening effect due to the pinning of dislocation by a high density of small loops is often accounted for using the so-called Dispersed Barrier Hardening model described by many authors from the late 50's [236] [237] [238] and investigated numerically in 1966 by Foreman and Makin [239]. According to this model, the increase in the yield stress ($\Delta\sigma$) due to the presence of a random array of small obstacles is proportional to the square root of the areal density of obstacles in the glide plane of the dislocation. It is often considered that for loops the areal density can be expressed as Nd where d is the mean diameter of loops and N the loop number density per unit volume. The increase in yield stress is thus expressed as Equation 1, where M is analogous to the Taylor factor that relates, for FCC metals, the critical resolved shear stress on the slip system to the yield stress. The concept of Taylor factor is often used for HCP metals, although it cannot be defined clearly because of the various slip systems. μ is the shear modulus (in MPa), b is the Burgers vector of the gliding dislocations and α is a coefficient characteristic of the strength of the obstacles. This last coefficient must be lower than 1 since it is equal to the cosinus of half the critical angle when the dislocation overcome the obstacle [240]. According to Foreman [239] the coefficient α must be lower than 0.8 for statistical reasons. Typical values of α coefficient for dislocation loops range from 0.25 to 0.5.

$$\Delta\sigma = \alpha M \mu b \sqrt{Nd} \qquad \text{(Eq. 1)}$$

From the literature data, it is clear that there is a strong correlation between the evolutions of the yield stress or hardness and the <a>-loop microstructure during irradiation or during annealing. However, only few authors have attempted to relate quantitatively the experimental yield stress

increase or hardness increase to the <a>-loop density and mean diameter to evaluate the relevance of such a simple model. Ribis et al. [108] obtained a coefficient $\boldsymbol{\alpha}$ =0.39 using a Taylor factor of $\boldsymbol{M}$ =4 or $\boldsymbol{\alpha}$ =0.78 for a Taylor factor of $\boldsymbol{M}$ =2. Cockeram et al. [72], using a Taylor factor equal to $\boldsymbol{M}$ =2, obtained a good correlation for a large body of data with a coefficient $\boldsymbol{\alpha}$ =1. Despite the uncertainty on the value for the Taylor factor, these results show that in zirconium alloys <a>-loops are rather strong obstacles, presumably because of segregation of solutes, such as oxygen, to loops. Furthermore, the fact that the irradiation hardening increment ($\boldsymbol{\Delta\sigma}$) does not depend on the test temperature suggests that dislocation and loop interactions are athermal.

5.01.5.1.3 Post-yield deformation: Macroscopic behavior

Concerning the mechanical behavior beyond the YS, it is pointed out by several authors [202] [241] [207] that for RXA zirconium alloys, the strain hardening rate is higher after irradiation at the onset of plastic flow but decreases rapidly with the plastic strain, more rapidly than before irradiation, resulting in a low strain hardening capability, and therefore in little difference between YS and UTS [28]. This strong decrease of the strain hardening rate is believed to be the cause of the early localization of the plastic strain at the specimen scale (from Considere's criterion), observed particularly in RXA zirconium alloys, which leads to a strong decrease of the uniform elongation, as reported by numerous authors [197] [198] [199] [201] [202] [203] [242]. Several authors [228] [243] [244] [245] have shown that, for RXA zirconium alloys, this apparent or macroscopic loss of ductility is related to the early localization of the plastic strain inside shear bands, the failure mode remaining ductile with dimples [202] [228] [242] [246] [247]. The material does not become brittle considering the fracture mode but localizes all the plastic strain in a limited part of the specimen, which leads, at the specimen scale, to a very low uniform elongation (**Figure 30**). As the irradiation-induced hardening increases with the fluence, the uniform elongation decreases rapidly with the fluence from 10% down to values lower than 1% for RXA alloys at 350 °C, and saturates from a fluence of 5×10^{24} n m^{-2} [197].

As for the irradiation-induced hardening, the SRA and RXA zirconium alloys exhibit similar uniform elongation at saturation [212]. Some authors [201] [242] suggest that there is a minimum of uniform elongation for RXA zirconium alloys for testing temperatures between 300

and 400 °C. This loss of ductility could be due to an additional hardening that can occur in this temperature range because of the trapping of oxygen atoms by the loops [242], as already observed using microhardness tests [213]. For testing temperatures above 400 °C, the ductility is progressively recovered as shown by Garde [242].

Reduction of area at failure is often considered as a good measure of the ductility of the material. Rosenbaum et al. [248] have shown that for a recrystallized Zircaloy-2 with typical texture of thin tubes irradiated up to 1.33×10^{25} n/m^2 and tested in the transverse direction at 250°C the reduction of area was 47.6% whereas it is equal to 77.6% before irradiation. This highlights that although the ductility of the material decreases with irradiation, its failure remains largely ductile.

In the case of RXA Zircaloy-4 irradiated at low temperatures (<200°C) and tensile tested at room temperature, Byun and Farrell [249] have shown that plastic instability occurs on the stress-strain curve for fluences above a critical fluence. This critical fluence corresponds to a critical radiation hardening or more precisely to a true stress critical value. Surprisingly, this critical value corresponds to the maximum true stress reached during tensile test done on the unirradiated material. This highlights that from a macroscopic point of view, irradiation hardening bears some similarities with strain hardening of unirradiated materials.

It is difficult to evaluate the fracture toughness of thin tubes made of zirconium alloys, however some data concerning the radiation effects on fracture toughness are available for thick pressure tubes used for CANDU reactors [250] [251]. It is shown that fracture toughness (in terms of dJ/da) decreases rapidly in the first four years of service and tends to saturates above a fluence of 3×10^{25} n/m^2 by irradiation, for temperatures between 240°C to 300°C. A transition temperature is observed, in the range of 70°C to 150°C, between a lower-shelf and an upper-shelf of the fracture toughness. However, the fracture mechanism after irradiation still remains void formation and growth in the two temperature domains.

Based on various mechanical data such as Knoop hardness test [215] or plane strain and plane stress tensile tests, several authors [198] [247] have shown that the irradiation decreases the plastic anisotropy of the RXA zirconium alloys. Concerning the SRA zirconium alloys, the mechanical behavior is already more isotropic before irradiation than RXA zirconium alloys [252] and the relative decrease of the anisotropy is therefore lower [247]. According to these

authors [247] [215] this decrease of the anisotropy of RXA zirconium alloys is due to a change of slip systems activation after irradiation.
A recent study of the anisotropy of tensile properties of CANDU calandria tubes at room temperature confirm these results [209]. It is observed that the yield stress (at 0.2% plastic strain) of the unirradiated material is lower in the longitudinal direction than in the transverse direction. As the neutron fluence increases, the longitudinal yield stress increases rapidly, more rapidly than the transverse yield stress. Leading to a reverse anisotropic behavior for low doses. For higher irradiation dose, both yield strength converge, showing a low anisotropic behavior in the Transverse-Longitudinal plane for this material.
By using nano-indentation on ion-irradiated zirconium alloys, some authors [221] succeeded in relating the radiation hardening to the orientation of individual grains. The results obtained suggest that <c+a> slip systems are less harden by irradiation than <a> slip systems thus explaining the reduced anisotropy after irradiation.

Fatigue properties of neutron irradiated zirconium alloys have also been investigated by several authors [253] [254] [255] [256] [257]. Pettersson et al. [254] do not find any significant effect of irradiation on fatigue life of Zircaloy-2 at 300°C. On the other hand, it is shown by Nakatsuka et al. [255] that for recrystallized Zircaloy-2 tested at 350°C in inert gas, neutron irradiation increases the fatigue life for a total strain amplitude above 0.3% but decreases the fatigue life for total strain amplitude below 0.3%. The increase or decrease in failure cycles is attributed to hardening or localized deformation in the irradiated material. O'Donnell and Langer [253] and Wisner al. [257] also confirm that for low-cycle fatigue (low-cycle high-strain) the number of cycle to failure (or the allowable stress for a given number of cycles) is reduced by irradiation. Furthermore, these authors [253] [257] have observed an interesting phenomenon during low cycle fatigue tests. Indeed, although the unirradiated material strain hardens during cycling, the irradiated material strain softens, so that there is little difference between the cyclic stress-strain curves for the unirradiated and irradiated conditions.

5.01.5.1.4 Post-yield deformation: mechanisms and modelling

Several authors [201] [228] [229] [244] [245] [246] [258] [259] [260] [210] have studied the deformation mechanisms using TEM by taking thin foils out of the specimens after testing. They have observed that, as for many other irradiated metals, after testing, numerous cleared bands free of irradiation defects are present in the material (**Figure 32**). These cleared bands are the consequence of the dislocation channeling mechanism reviewed in detail by Hirsch [226], Wechsler [261], and Luft [262]. According to several authors [263] [264] [265], the irradiation-induced loops, which are obstacles to dislocation glide, can be overcome by dislocations when a sufficient stress is applied, the loops being subsequently annihilated or dragged by dislocations following different possible mechanisms [224] [225] [226] [233] [266]. This process of removal of irradiation loops by moving dislocations produces a cleared zone free of defects inside the grain. These obstacle-free channels or swaths will therefore constitute preferred areas for further dislocation gliding, leading to plastic strain localization at the grain scale with regions of very high local plastic strain surrounded by regions of almost zero plastic strain. According to Williams *et al.* [243] and Adamson *et al.* [244], the local plastic strain could reach up to 100% inside these bands.

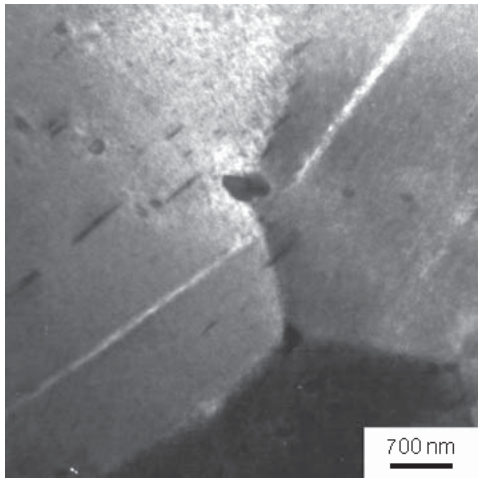

Figure 32 Propagating basal channels observed after tensile testing at 350 °C. Adapted from Onimus, F.; Monnet, I.; Béchade, J. L.; Prioul, C.; Pilvin, P. *J. Nucl. Mater.* **2004**, *328*, 165–179.

Drouet et al. [235] have been able to observe, in real time and at the nanometer scale, using in situ straining experiments inside a TEM, the incorporation and the clearing of loops by gliding

dislocations in recrystallized Zircaloy-4 irradiated with Zr ions. These observations explain the dislocation channels formation.

Several authors have analyzed the plane corresponding to channels. Some have observed channels along the prismatic planes [213] [244] for tests performed at 250 and 327 °C on a Zircaloy-2 containing 1500 ppm oxygen and irradiated up to 3×10^{25} n/m^2. This material had a typical texture of rolled plate and the tensile test was conducted along the transverse direction. For low oxygen material (44 ppm), the authors found that channels are along the basal planes. Other authors [229] [258] [259] [260] have observed channels along the basal plane for transverse tensile tests and internal pressure tests conducted at 290°C or 350°C on recrystallized zirconium alloys with typical texture of thin tubes or rolled plates. When the samples were tested along the axial direction at 350°C, prismatic and pyramidal channels were observed. This is easily explained by the fact that in this case the basal slip systems undergo a very low resolved shear stress because of the strong texture of the material. When conducting transverse tensile tests at room temperature, using ring specimens taken from thin tubes, basal, prismatic and presumably pyramidal channels are observed [210]. This suggests that temperature has a significant effect on the activation of the various slip systems of zirconium alloys after irradiation. Recently, Thomas et al. [267] have conducted transverse tensile tests at room temperature on proton irradiated samples made of recrystallized Zircaloy-4. The irradiation was conducted using 2 MeV protons at 357°C up to a damage dose of 0.13 dpa. By using High Resolution Digital Image Correlation they observed intense shear bands inside the grains parallel to prismatic planes and also, for few grains, parallel to pyramidal planes. Fournier et al. [125], after testing similar samples at room temperature, observed basal and prismatic channels.

The fact that the basal slip becomes the easy glide slip system at 350°C after irradiation constitutes a major change in the deformation mechanisms since, before irradiation, for the same test temperature it is the prismatic slip system that is the easy glide slip system. This change in the deformation mechanisms can be explained by the difference in the interaction between the irradiation-induced loops and the dislocations gliding either in the basal plane or in the prismatic plane, as pointed out previously. Indeed, the junction created between a dislocation gliding in the basal plane and a loop is always glissile, whereas it is sessile when the dislocation is gliding in

the prismatic plane. Therefore, when the dislocation glides in the basal plane and encounters a loop, the loop can be dragged along the slip plane, leading to a progressive clearing of the basal channel.

As mentioned above, dislocation and loop interactions in zirconium have been investigated numerically using molecular dynamics simulations by several authors [231] [232]. It is shown that for several configurations, the loop is incorporated into the dislocation as double super-jog which can be easily dragged away. In order to reach higher length scale and study more complex configurations, Drouet et al. [234] have conducted dislocation dynamics simulations of interactions between dislocation and loops. These simulations have been able to confirm that there are less pinning configurations for basal slip than for prismatic slip explaining the easier clearing of loops by basal glide and thus the easier dislocation channeling phenomenon.

Since the loops are cleared by gliding dislocations inside the channels, it is usually assumed [268] that within the channels a strain softening occurs. This phenomenon is believed to be the cause of the decrease of the strain-hardening rate with irradiation and thus to the early localization of the deformation at the specimen scale, explaining the dramatic decrease of the uniform elongation after irradiation [201] [268]. According to several authors [244] [262], the strong texture of the rolled sheets or tubing leads to an even stronger localization of the plastic strain. Indeed, due to the texture, the $\langle c \rangle$ axis of the hcp grains is along the (r, θ) plane in the case of a tube. Since for internal pressure test or transverse tensile tests the channels are along the basal plane, the basal channels can easily propagate from grain to grain, as it has been shown by Onimus *et al.* [258] [259] [260]. When the entire section of the specimen is crossed by dislocation channels, a strong necking is observed on the specimen. As was pointed out by Franklin *et al.* [269], the RXA alloys are more susceptible to the plastic instability since the dislocation tangles that remain in SRA alloys are believed to inhibit the easy glide and the plastic flow localization.

As discussed by Onimus and Béchade [270], the polycrystalline nature of the material may also play an important role in the overall macroscopic response of irradiated zirconium alloys after irradiation. Indeed, although dislocation channels are created from the onset of plasticity, the intergranular stresses that develop because of strain incompatibilities between grains balance the local microscopic softening occurring in the dislocation channels leading to a macroscopic strain

hardening behavior. When the strain softening is too strong, because of the multiplication of dislocation channels, or when the intergranular stress increase becomes too low to compensate for the microscopic strain softening, Considere's criterion can be reached and plastic instability occurs at the specimen scale leading to an early necking.
The cyclic strain softening observed during low-cycle fatigue tests is presumably due to the clearing of loops by gliding dislocations and the creation of dislocation channels [257].

At a larger length scale, the clearing of loops by gliding dislocations can be accounted for in crystal plasticity models by introducing a strain softening term in the local behavior of individual grains. This has been done by several authors using polycrystalline models [270] [260] or Finite Element computations [271].

5.01.5.2 Mechanical behavior after postirradiation heat treatment

5.01.5.2.1 Effect of postirradiation heat treatment on macroscopic properties

A heat treatment performed at a temperature higher than the irradiation temperature on various zirconium alloys results in a recovery of the radiation-induced hardening [195] [272] [210] [273] (**Figure 33**). This recovery can also be measured using microhardness tests [213] [214] [216] [108] [210] [274] [275] [276] [277]. The recovery of the hardening is always associated with the recovery of the ductility and the fracture properties [272] [210] [273].
Howe and Thomas [195] have shown that in a cold-worked zirconium alloy most of the recovery occurring between 280 and 450 °C appears to be the annealing out of radiation damage rather than cold work. In the case of strongly cold-worked zirconium alloys such as SRA Zy-4, radiation hardening recovery is also observed. The hardness of the material can even become lower than the initial hardness of the SRA Zy-4 [216] [210] owing to the recovery of the dislocations, in addition to the recovery of the loops.

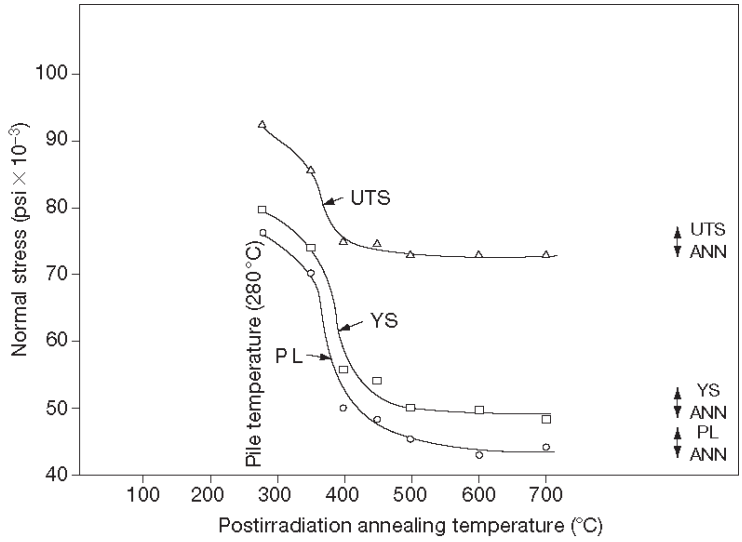

Figure 33 Recovery curves for irradiated annealed Zy-2. PL: Proportional limit, YS: 0.2% offset yield stress, UTS: ultimate tensile strength. Adapted from Howe, L.; Thomas, W. R. *J. Nucl. Mater*. **1960**, *2*(3), 248–260

Some authors [213] [275] [278] [242] [273], on the basis of various experimental results, have suggested that there is an interaction between oxygen and irradiation-produced dislocation loops, which increases the dislocation–defect barrier interaction. During the recovery, this phenomenon can lead to an additional hardening, as shown by Snowden and Veevers [275].

5.01.5.2.2 Effect of postirradiation heat treatment on the microstructure: experiments

Several authors [60] [213] [216] [108] [276] [279] [280] [273] have shown that during a heat treatment performed on a RXA zirconium alloy, the $\langle a \rangle$ loop density strongly decreases and the loop size increases. This decrease of the obstacle density to dislocation motion has been clearly correlated to the decrease of the radiation-induced hardening [213] [108] [273].

Concerning the nature of the loops, Kelly and Blake [60] have studied 240 loops in a zirconium alloy sample heat-treated at 490 °C during 1 h after irradiation up to a fluence of 1.4×10^{24} n m^{-2}. These authors show that, although the initial microstructure is composed of both interstitial and vacancy loops in equal amount, after the heat treatment, two-thirds of the analyzed loops are vacancy loops and only one-third are interstitial loops. This implies that the interstitial loops undergo a more rapid recovery than the vacancy loops. These observations have been recently confirmed by Ribis et al. [108] [216], who observed that the proportion of vacancy loops

increases during heat treatment. These authors also noticed that the β-Nb nano-precipitates, formed under irradiation, are very stable during annealing [73] [186]. They also found that the <c>-component loops do not anneal out during heat treatment but exhibit a change in their Burgers vector, from $\frac{1}{6}\langle 20\bar{2}3\rangle$ to $\langle 0002\rangle$ as also shown in [105].

Recently, Topping et al. [281] were able to characterize the loop recovery when analyzing the diffraction peak width by XRD experiments. Furthermore, they were able to see, by in situ TEM, the motion of two <a>-loops toward each other during annealing.

When analyzing by TEM samples tested at room temperature after prior post-irradiation creep test, Bourdiliau et al. [210] have been able to explain the origin of the recovery of strength and ductility observed after heat treatment. Indeed, without prior annealing it is seen that plasticity occurs by dislocation channeling process because of the high density of small <a>-loops. With prior heat treatment, or creep test, <a>-loops have been annealed out and deformation occurs by homogeneous glide of dislocations similar to the unirradiated material, thus explaining the recovery of uniform elongation.

5.01.5.2.3 Effect of postirradiation heat treatment on the microstructure: mechanisms

In the literature, several mechanisms are proposed in order to explain the irradiation damage recovery. The most commonly agreed mechanism is based on bulk diffusion of vacancies during the recovery and their exchange between loops of various size [108] [216] [282] [283] [284]. Indeed, the smaller vacancy loops emit vacancies that diffuse toward larger vacancy loops, which absorb more vacancies than they emit, leading to a growth of the larger loops at the expense of the smaller loops. On the other hand, interstitial loops always absorb vacancies whatever their size, since the vacancies are in supersaturation during the heat treatment, explaining the rapid disappearance of the interstitial loops [108] [216] [282]. Another annealing mechanism, based on loop coalescence is also discussed in the literature. Because of the attractive stress field that can arise between loops, depending on their respective location and Burgers vector, an attractive force between loops can arise. This attractive force can result in loop motion towards each other, either by glide on their cylinder, or through a self-climb phenomenon described in [285] [286].

5.01.5.3 Postirradiation creep behavior

5.01.5.3.1 Postirradiation creep: macroscopic behavior

There are relatively few data in the literature concerning the postirradiation creep behavior of zirconium alloys as pointed out by Peehs and Fleisch [287]. Even in the thorough review by Franklin *et al.* [269], very few results concerning the postirradiation creep are given. In the case of the SRA zirconium alloys [277] [288] [289] [290] [291] [292] [293] or RXA Zy-2 [277] [294], several authors have shown that irradiation leads to a strong decrease of the creep rate (**Figure 34**). This phenomenon is attributed to the presence of a high density of irradiation defects that harden the material. However, according to Ito *et al.* [277] and Schäffler *et al.* [290], irradiation does not seem to affect strongly the stress sensitivity coefficient of SRA Zy-4, at least for the high stress range. However, for low applied stress, Ito *et al.* [277] have shown that the stress sensitivity coefficient is lower after irradiation than before irradiation. They have also shown that irradiation has a weak effect on the creep activation energy of SRA Zy-4 for temperatures from 330 to 600 °C and for stresses from 77 to 384 MPa. Murty and Mahmood [295] have suggested that the creep anisotropy of RXA Zy-2 is decreased by irradiation. According to these authors, this phenomenon is due to the activation of other slip systems than the prismatic slip system after irradiation, such as the basal and the pyramidal slip systems.

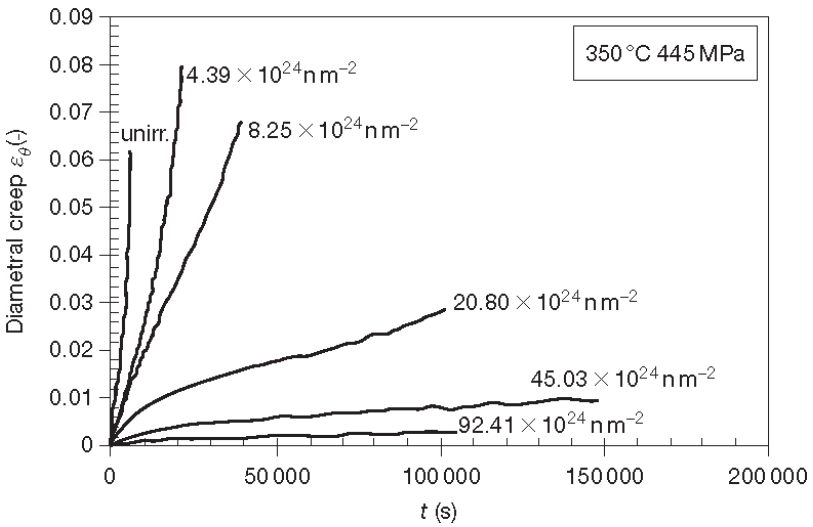

Figure 34 Effect of fluence on thermal creep behavior at 350 °C of irradiated SRA Zy-4 cladding tubes. Reprinted, with permission, from *Thirteenth International Symposium on Zirconium in the*

Nuclear Industry, 2002, copyright ASTM International, 100 Barr Harbor Drive, West Conshohocken, PA 19428

Cappelaere *et al.* [292] and Limon and Lehmann [293] have shown that for low applied stress, a 'tertiary creep' occurs for SRA Zy-4, even though the creep strain level remains low. This phenomenon cannot be explained by the increase of the stress due to the thinning of the wall of the tube. This phenomenon is therefore interpreted as a result of the recovery of the irradiation defects during the creep test and also due to the beginning of the recrystallization that can occur for high-temperature creep tests. Tsai and Billone [296] have come to the same conclusions by analyzing their own long-term creep tests.

5.01.5.3.2 Postirradiation creep: mechanisms

The recovery of irradiation loops during creep tests has been observed, by several authors on SRA Zy-4 [292] or RXA Zr–1% Nb–O alloy [259] using TEM, but it is the work by Ribis *et al.* [216] that gives the most detailed study of the microstructure evolution during creep tests of the above alloy. In this study, the microstructure is compared to that observed after postirradiation heat treatment or after creep of the nonirradiated material. It is shown that in RXA zirconium alloys, the irradiation loops are progressively annealed out during the creep test, as for a heat treatment without an applied stress, the magnitude of the recovery being similar in both cases. Moreover, these authors show that β-Nb nano-precipitates and <c>-loops do not anneal out during creep tests. It is also noticed that for tests performed at 400 °C and for low applied stress (130 MPa), in addition to the recovery of loops, the microstructure observed after creep tests exhibits a high dislocation density. This phenomenon could result from the <a>-loops, the <c>-loops and the β-Nb nano-precipitates that act as obstacles to dislocation motion. This could explain that for long-term creep test performed at 400 °C under an applied stress of 130 MPa, although a significant recovery of the irradiation damage occurs, the creep strain remains limited. For higher applied stress, higher than 200 MPa, these authors suggest that a sweeping of loops occurs. This mechanism is believed to be similar to the dislocation channeling mechanism that is observed for burst tests and tensile tests [258] [259] [260]. This mechanism therefore allows the deformation of the material for high applied stress.

5.01.6 Deformation under irradiation

5.01.6.1 Irradiation growth

5.01.6.1.1 Irradiation growth: macroscopic behavior

One of the most specific macroscopic effects of irradiation on materials is the dimensional change without applied stress. In the case of zirconium alloys, it is known that under neutron irradiation, without any applied stress, a zirconium single crystal undergoes an elongation along the basal plane (along the ⟨ *a*⟩ axes) and a shortening along the ⟨ *c*⟩ axis without significant volume evolution. Thorough reviews of this phenomenon have been given in [104] [288] [297] [298] [299] [300] [301]. A recent comprehensive review of irradiation growth, written by R. Adamson, C. Coleman and M. Griffiths can be found in [17]. It is observed that the elongation along the basal plane (along the ⟨ *a*⟩ axes) is rapid at the beginning of the irradiation and slows down until reaching a low stationary growth rate (**Figure 35**). The growth strain remains small (<0.02%) and saturates at fluences less than 5×10^{24} n m^{-2} [299] [302]. Eventually, at higher fluence a growth breakaway (increase of the growth rate) occurs for annealed zirconium single crystals. [299].

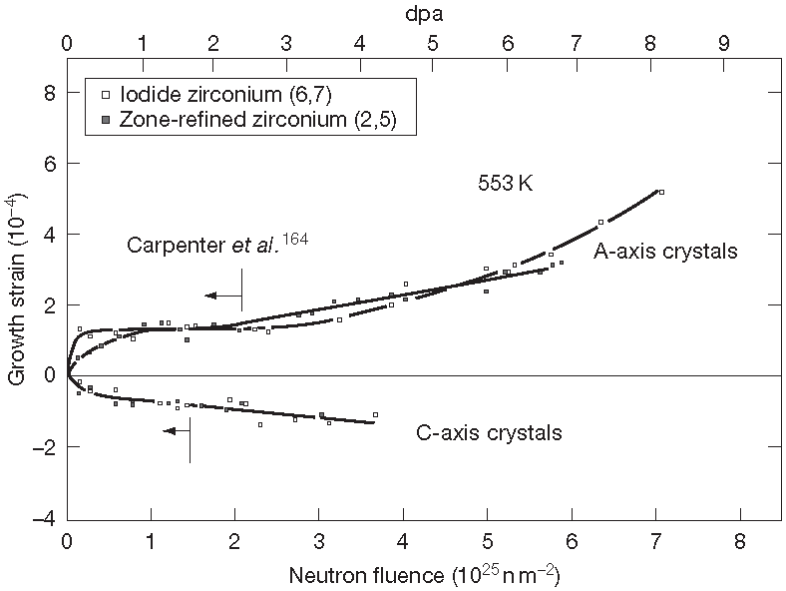

Figure 35 High-fluence growth strain as a function of fluence for annealed zirconium single crystals at 553 K. Adapted from Carpenter, G. J. C.; Zee, R. H.; Rogerson, A. *J. Nucl. Mater.* **1988**, *159*, 86–100

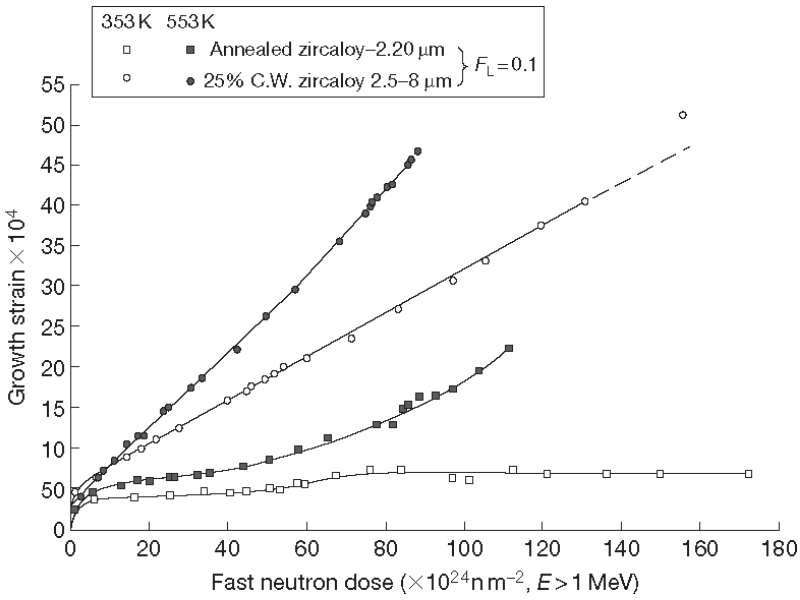

Figure 36 Irradiation growth in annealed and 25% cold-worked Zircaloy-2 at 353 and 553 K. Rogerson, A. *J. Nucl. Mater.* **1988**, *159*, 43–61

Since the deformation of the polycrystalline cladding is the result of the growth of all the grains, the crystallographic texture has a major influence on the growth of the polycrystalline material. The crystallographic texture can be characterized in a simple way by the Kearns factors. . The Kearns factor f_d is defined as the resolved fraction of basal poles (i.e. <c> axis) along the direction d [305]. A weakly textured product made of zirconium alloy, with Kearns factors close to $f_d \approx 0.33$ along the three directions, such as β-quenched zirconium alloys [303] [304] as reviewed by Fidleris [288], exhibits a very low growth. Indeed, the growth strains of randomly oriented grains cancel each other. On the other hand, strongly textured products, with most grains orientated with $\langle c \rangle$ axis along one given macroscopic direction (high Kearns factor, $f_d >$ 0.5), exhibit a negative growth in this direction and a positive growth in the direction with low Kearns factor ($f_d <$ 0.2). It is indeed commonly acknowledged that growth rate in the direction d, is proportional to following expression (Eq. 2). This expression can be easily derived theoretically assuming constant volume for growth.

$$\dot{\varepsilon}_d \propto 1 - 3f_d \quad (2)$$

In the case of highly textured products such as cold-worked tubing, in SRA or RXA metallurgical state, a large majority of the grains exhibit their $\langle c \rangle$ axis close to the radial

direction (⟨ c⟩ axes oriented in the (r, θ) plane with an angle between 20° and 45° to the radial direction, the Kearns factor along the radial direction being f_r □ 0.6). The directions $\langle 11\bar{2}0\rangle$ or $\langle 10\bar{1}0\rangle$ are along the rolling direction (low Kearns factor along the rolling, or axial direction f_a □ 0.1–0.16. [306] [150]). Due to this strong texture, an elongation of the tube along the rolling direction is observed [297] [150] as well as a decrease of the thickness as shown on rolled sheet, [297] the strain along the diameter of the tube remaining low [291] since the Kearns factor along the hoop direction is close to 0.3.

In the case of cold-worked Zr–2.5Nb pressure tube for Canadian deuterium uranium (CANDU) reactors, the irradiation growth leads to an increase of the length in the axial direction and a decrease of the diameter (associated to a thickness increase) since the ⟨c⟩ axes are mainly along the transverse direction ($f_r \sim 0.3, f_a \sim 0.05, f_t \sim 0.6$, respectively for radial, axial, and transverse Kearns factors), [301].

Textured RXA Zy-4 or Zy-2 products, in the form of thin tubes or thin sheets, exhibit first a rapid elongation along the rolling direction, and then a decrease in the growth rate, reaching a low stationary rate [297]. It can be noticed that the stationary growth strain of the polycrystal is higher than that for the Zr single-crystal [299] suggesting an effect of the grain boundaries on the growth mechanisms. For higher fluence, higher than 5×10^{25} n m^{-2}, a growth breakaway is observed, yielding a high growth rate, similar to that of SRA zirconium alloys (**Figure 36**) [304] [298]. This phenomenon is also observed for recrystallized Zr1%Nb and Zr-Nb-Sn-Fe alloys as reported by Kobylyansky et al. [115] [118].

There is no evidence of any large change in volume during neutron irradiation of polycrystalline zirconium alloys [288], although some authors [307] measured a slight volume change, less than 0.1%. More recently, it has been assessed by Holt and Causey [308] that there is a volume conservation during growth of Zr2.5Nb. Yagnik et al. [118] also proved that the volume change remained very small, but nonzero, during free growth of RXA Zircaloy-4 thick plate, even up to high fluences.

When considering the growth of thin tubes used for fuel rod cladding tube, two different measures can be found in the literature: the fuel rod growth and the stress free growth. The stress free growth is the actual mechanism of interest here. Whereas the fuel rod growth is not only due

to irradiation growth (stress free growth), but anisotropic creepdown and, at higher fluences, the pellet cladding mechanical interaction, also contribute [304] [309] [310].

It is reported [57] [288] [298] [304] that for polycrystalline zirconium alloys, the grain size affects the growth rate of RXA zirconium alloys during the initial growth transient at 280°C, the growth rate increasing when the grain size decreases. On the other hand, the stationary growth is not affected by the grain size. This phenomenon is also observed for Zircaloy-2 [297]. Ibrahim and Holt [311] and Holt [312] have also suggested that the grain shape, especially in the case of Zr–2.5% Nb material, can play a role on the growth behavior.
It is shown that for cold-worked materials ($\varepsilon > 10\%$) the growth rate increases as the cold working increases [288] [297] [298]. For the extreme case of SRA zirconium alloys, which could undergo up to 80% cold working followed by a stress-relieving annealing, the growth rate is so high that the stationary growth rate is not observed, and from the beginning of the irradiation, the growth rate is comparable to the growth rate measured for RXA zirconium alloys after the breakaway growth. The dependence of the amount of cold-working on the growth rate has been also observed for Zy-2 and Zr-Nb-Sn-Fe alloys by Kobylyansky et al. [115]. Several authors, as reviewed by Fidleris *et al.* [297] and Holt [104], have clearly correlated the increase of the growth rate with the increase of the dislocation density [106] due to the cold working. This also proves the importance of the initial dislocation network in the growth mechanisms.
The irradiation temperature has a complex influence on the growth behavior [104] [288]. For SRA zirconium alloys, it is shown that the growth rate increases as the temperature increases. On the other hand, for RXA zirconium alloys the prebreakaway growth rate has a very low temperature sensitivity, the growth rate increasing very slowly with increasing temperature. A growth peak is even observed around 20°C, the growth rate decreasing rapidly above 350°C. However, for postbreakaway growth, the temperature sensitivity is high, as high as for SRA zirconium alloys [288]. It is also shown that the breakaway fluence decreases with increase in the temperature [104].

Several authors have studied the effect of the impurity and alloying elements on the growth rate and especially on the growth acceleration. For a high-purity zirconium single-crystal obtained by the melting zone method, no growth breakaway is observed at 280 °C,. On the other hand, for a

lower purity zirconium single crystal obtained by using the iodine purification method [299] the breakaway growth is observed. Similarly, for polycrystalline RXA zirconium alloys, irradiated at elevated temperature (390–430 °C), the growth rate is higher than that of pure zirconium [106] [298]. It is particularly noticed by Griffiths *et al.* [106] that RXA zirconium alloys exhibit accelerated growth contrary to pure zirconium.

Tin appears to enhance or diminish growth relative to that in unalloyed zirconium depending on the temperature [298]. Zee et al. [313] have observed differences in the early transient growth for temperatures 353 K but similar steady state growth rates at higher fluences. For a temperature of 553 K tin increases the growth rate during transient, but similar steady-state growth rate is reached for low tin and high zirconium alloys. In the thorough review of Rogerson [298] it is stated that the minor elements (Fe, Cr, Ni) appear to influence growth in zirconium and its alloys. However, only few data concerning this point were available at that time. With the development of new alloys, the influence of niobium, tin and iron have been systematically studied. Gilbon et al. [150] have shown that recrystallized Zr-1%Nb alloys exhibit a reduced growth rate compared to RXA Zy-4. This was confirmed later, up to higher fluences, by Bossis et al. [114]. Kobylyansky et al. [115] when studying the growth behavior of Zr-Nb-Sn-Fe alloys, such as E635, have also proved that Zr-Nb-Sn-Fe alloys exhibit a significantly reduced growth rate compared to recrystallized Zy-2. Shishov et al. [74] have shown that when the iron content is increased from 0.15 to 0.65 in a Zr-Nb-Sn-Fe alloy, the onset of the accelerated growth is significantly delayed. It is also shown by Chabretou et al. [172] that introducing 0.3%Sn and 0.1%Fe in a Zr-1%Nb alloy leads to a reduced free growth. It is the recent work by Yagnik et al. [118] which gives the most systematic investigation of alloying element effect on free growth. In this study, it is shown that the addition of niobium decreases the free growth. Zirconium alloys containing only tin and iron had the highest growth. An increase in tin content leads to a slight decrease of growth. The addition of iron causes a significant decrease in growth in Zr-Nb and Zr-Sn alloys as well as in Zr-Sn-Nb alloys (**Figure 37**).

These last authors [118] also studied the impact of hydrogen on free growth, because of in-reactor hydrogen pick-up. It is shown that all the samples containing more than 100 ppm hydrogen exhibit an increased growth rate compared to the samples containing less than 10 ppm hydrogen.

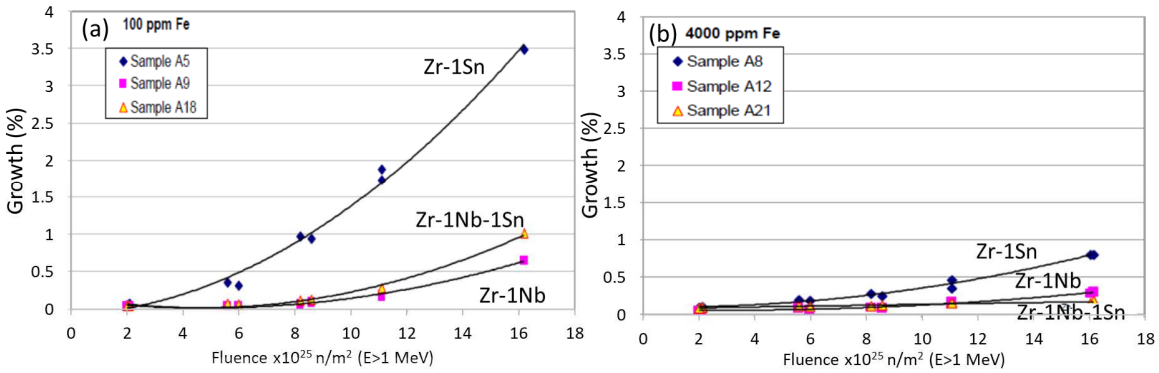

Figure 37: Irradiation-induced growth strain as a function of fast fluence for several different zirconium alloys with varying iron additions from 100 to 4000 ppm.

5.01.6.1.2 Irradiation growth: mechanisms and modelling

The mechanisms proposed in the literature in order to explain the growth under irradiation of zirconium and its alloys have progressively evolved as the observations of the microstructure have progressed. Recent atomistic numerical simulations also brought a new light on the detailed mechanisms explaining growth.

Several comprehensive reviews of these mechanisms have been given [55] [58] [104] [301] and a nice history of the various mechanisms for irradiation growth of zirconium alloys is provided by Holt [300]. Some of these mechanisms are not compatible with all the observations. For instance, the fact that both vacancy and interstitial $\langle a \rangle$ loops in prismatic planes are present in the polycrystalline material, as described in the first part, shows that the model proposed by Buckley [314] and described by Northwood [315] and Holt [300] for the growth of zirconium alloys, is not correct.

The most promising model that gives the best agreement with the observations is the model based on the DAD, first proposed by Woo and Gösele [316] and described in detail by Woo [55]. This last model is based on the assumption that the diffusion of SIAs is anisotropic, the vacancy diffusion anisotropy being low. Indeed, as reported in the first part of this chapter, several authors [35] [40] [41] [317] have shown, using atomistic simulations, that the mobility of the SIAs is higher in the basal plane than along the $\langle c \rangle$ axis and that the vacancy diffusion is only slightly anisotropic.

The growth mechanism proposed by Woo [55] is the most convincing model, since every feature of the growth phenomenon is understood in its frame unlike in the previous models. According to this mechanism, during the first stage of the irradiation of RXA zirconium alloys, with low initial dislocation density, the grain boundaries are the dominant sinks. Due to the rapid mobility of SIAs in the basal plane, the grain boundaries perpendicular to the basal plane are preferential sinks for SIAs. In contrast, grain boundaries parallel to the basal plane constitute preferential sinks for vacancies. This leads to a fast initial growth of polycrystalline zirconium alloys, in agreement with the model first proposed by Ball [318] (**Figure 38(a)**). This mechanism explains why the initial growth transient is sensitive to the grain size.

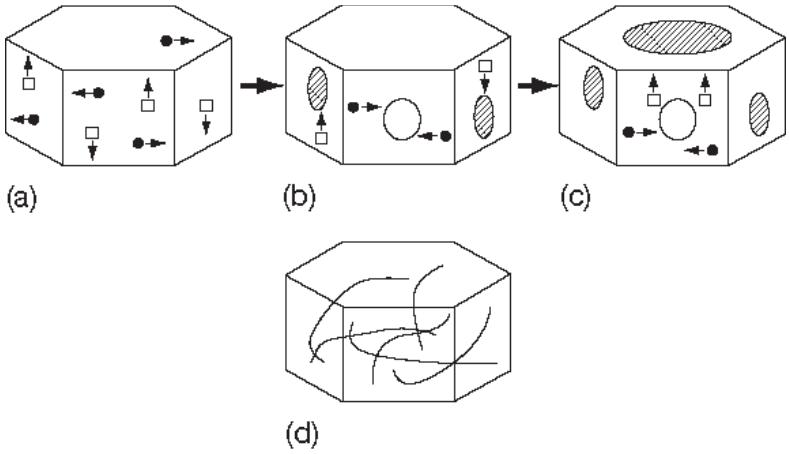

Figure 38 (a–c) The three phases of growth of recrystallized zirconium alloys. (d) Growth mechanisms of stress relieved zirconium alloys.

As the irradiation dose increases, the ⟨ *a*⟩ loop density increases and the ⟨ *a*⟩ loops become the dominant sink for point defects. In the absence of ⟨ *c*⟩ component dislocation (as is the case in RXA zirconium alloys), calculations of DAD-induced bias show that linear ⟨ *a*⟩ type dislocations parallel to the ⟨ *c*⟩ axis are preferential SIA sinks while ⟨ *a*⟩ type loops are relatively neutral and may receive a net flow of either interstitials or vacancies, depending on the sink situation in their neighborhood. This explains why both interstitial and vacancy ⟨ *a*⟩ type loops can be observed. This also explains why in the neighborhood of prismatic grain boundaries, or surfaces, which experience a net influx of SIAs, there will be a higher vacancy supersaturation leading to a predominance of vacancy loops towards interstitial loops as shown by Griffiths [58]. It has to be pointed out that the simultaneous growth of interstitial and vacancy

⟨ *a*⟩ type loops in the prismatic plane does not induce strain of the crystal although they are the dominant sinks (**Figure 38(b)**). This explains the low stationary growth rate observed.

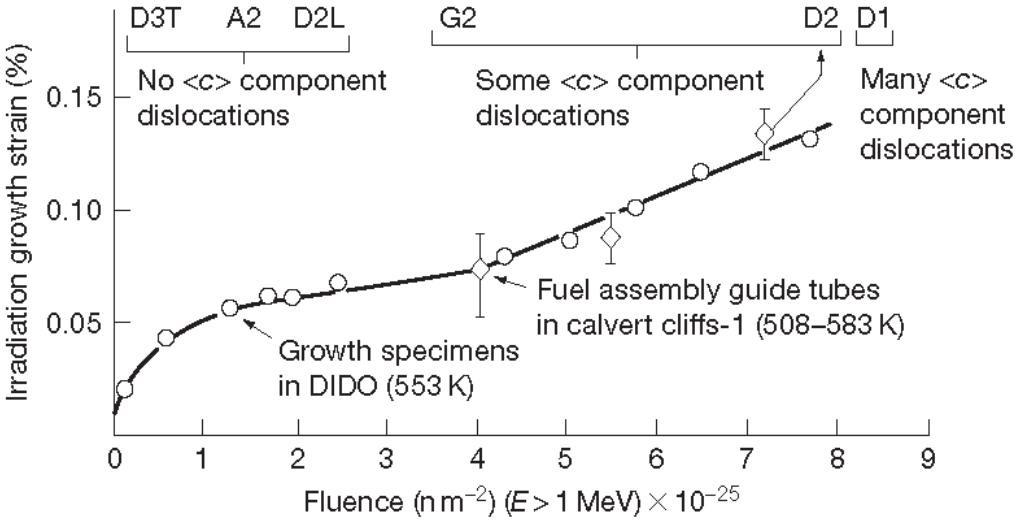

Figure 39 Irradiation growth in annealed (RXA) Zircaloy at 550–580 K, showing accelerating growth at 4 × 10^{25} n m^{-2} (E > 1 MeV). Adapted from Fidleris, V. *J. Nucl. Mater.* **1988**, *159*, 22–42

For irradiation doses higher than 5 × 10^{25} n m^{-2} (in the case of RXA Zircaloy-4), vacancy ⟨ *c*⟩ component dislocation loops in the basal plane are observed in RXA zirconium alloys (**Figure 38(c)**). It is commonly acknowledged that the nucleation and growth of these loops are responsible for the growth breakaway [103] (**Figure 39**). Indeed, the clustering of vacancies in the form of disks in the basal plane induces a shrinking along the <c>-axis. Further growth of these loops, via the climb of the dislocation line surrounding the vacancy disc, explains the accelerated growth rate. The elongation of the zirconium grains along the basal plane, because of mass balance, may be the result of interstitials diffusing towards grain boundaries, or to the preferential growth of interstitial <a>-loops, at the expense of vacancy <a>-loops. It is interesting to note that the original Buckley's mechanism is partly relevant for breakaway growth.
The origin of the nucleation of ⟨ *c*⟩ component loops remains unclear. As discussed earlier, it is very sensitive to impurities and alloying elements redistribution, such as iron [67] [106] [110] [111]. As explained previously, the fact that these vacancy ⟨ *c*⟩ component basal loops are able

to grow in zirconium alloys, whereas it is the ⟨ *a*⟩ prismatic loops that are the most stable, is easily explained in the frame of the DAD model. It can be shown that it is due to the DAD that vacancies are eliminated preferentially on the ⟨ *c*⟩ component loops and on the grain boundaries parallel to the basal plane. The SIAs are eliminated on ⟨ *a*⟩ type dislocations and grain boundaries parallel to the prismatic plane. This partitioning of the point defects on these different sinks leads to the growth of the vacancy ⟨ *c*⟩ component loops and therefore to the accelerated growth of RXA zirconium alloys. There is a clear qualitative correlation, at least at low dose, between the occurrence of the breakaway and the appearance of ⟨ *c*⟩ loops. However, as pointed out by Griffiths et *al.* [106], the strain induced by the loops observed is significantly lower than the growth strain measured. The strain induced by the <c>-loops is thus probably only a minimum estimate. Griffiths et al. [106] also show that as the fluence is further increased after the onset of accelerated growth, there is less agreement between calculated and measured strains. It seems that a better correlation could be obtained between growth rates and <c>-loops densities. The recent work by Yagnik et al. [118] also tried to correlate the linear density of <c>-loops observed by TEM and the growth strain. It is shown that as the growth strain increases, the <c>-loop linear density increases, in good agreement with the proposed mechanism. However, when the growth strain reaches values above 2%, the <c>-loop linear density tends to saturate and no obvious evolution occurs whereas the growth strain keeps increasing. This phenomenon could probably be partly explained by the fact that the largest <c>-loops are cut by the two surfaces of the TEM thin foil. These results also underline that the relationship between <c>-loops and accelerated growth strain is probably not so straightforward.

The fast and continuous growth of cold-worked or SRA zirconium alloys can also be easily explained by this model. Indeed, since in these materials the ⟨ *c* + *a*⟩ line dislocations are already present before irradiation, under irradiation, the vacancies are preferentially eliminated on the dislocations, with ⟨ *c* + *a*⟩ Burgers vector, which lie in the basal plane [104] [300] [301], leading to the climb of these dislocations. On the other hand, the SIAs are eliminated on ⟨ *a*⟩ type dislocations, leading to the climb of these dislocations. This partitioning of point defects therefore leads to the fast and continuous growth of cold-worked or SRA zirconium alloys (**Figure 38(d)**). Here the growth created by the point-defect flux to the grain boundaries is relatively unimportant because they are not dominating sinks. Irradiation growth under such circumstances is thus not sensitive to the grain size or shape [319].

Many authors [104] [318] [320] [321] [322] [323] [324] [325] [326] [327] have proposed rate theory models, based on various hypotheses, to account for the free growth of zirconium alloys. Some of these authors used the DAD theory as the main hypothesis for their model. Recently, Christien and Barbu [129] introduced most of the DAD hypotheses into a cluster dynamics model and managed to compute the growth strain of zirconium single crystal.

The recent atomistic simulations that showed no clear evidence of anisotropic diffusion of SIAs have shed doubt on the DAD theory. Several alternative models have been proposed to account for irradiation growth. Golubov and Barashev [328] proposed a rate theory model where the anisotropic diffusion of SIAs is replaced by the 1D or 2D motion in the basal plane, of small point defect clusters. The rate theory model was then able to compute the evolution of the growth strain with irradiation.

It has also been discussed by several authors, especially by Woo [329] and Holt [300] that due to the polycrystalline nature of the material, the growth strain of the individual grains can induce strain incompatibilities between adjacent grains that exhibit different orientations. Intergranular stresses can then result from these strain incompatibilities, leading to a local irradiation creep of individual grains even without macroscopic applied stress on the material. This phenomenon can also affect the growth behavior of the polycrystalline material. It has also been shown that the intergranular stresses resulting from a deformation prior to irradiation can lead to a complex transient growth behavior at the beginning of the irradiation due to intergranular stress relaxation [300] [330]. Many authors have modeled the interactive creep and growth of polycrystalline zirconium alloys. They have used statistical average on the grain orientations representative of the texture of the material, such as the upper bound evaluation [331] [332] or the self-consistent evaluation [327] [333] [334]. Thanks to their numerical models, these authors emphasized that because of the intergranular stresses that arise from strain incompatibilities, a coupling between creep and growth appears at the polycrystalline scale. A recent work on this subject can also be found in [335].

5.01.6.2 Irradiation creep

5.01.6.2.1 Irradiation creep: macroscopic behavior

Metals and alloys subjected to simultaneous constant load, below yield stress, and irradiation exhibit a creep deformation. Depending on the applied stress and temperature, the in-reactor creep rate can be higher than the out-of-reactor 'thermal' creep rate of the unirradiated material, the creep rate increasing as the neutron flux increases (**Figure 40**). This peculiar deformation phenomenon activated by the neutron flux is called irradiation creep.

The creep behavior of zirconium alloys under irradiation has been studied extensively, from the early 1960's to the late 1980's, because of the major importance of the prediction of the in-reactor deformation of the fuel assembly in the case of pressurized water reactor (PWR) and boiling-water reactor (BWR) [309] or in-reactor structure especially in the case of the CANDU reactor [336].

These early studies have been reviewed by Franklin *et al.* [269] and Fidleris [288]. For CANDU reactors several other recent experiments have been conducted and are described in the thorough review by R. Holt. [301]. The readers are also invited to refer to the recent review by R. Adamson, C. Coleman and M. Griffiths [17] in which more data can be found.

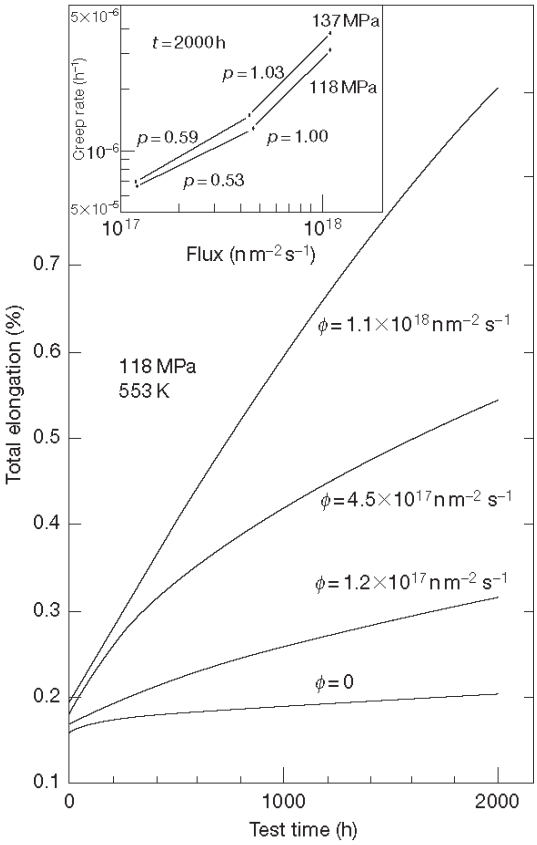

Figure 40: Flux dependence of in-reactor uniaxial creep of cold-worked Zircaloy-2 (adapted from Fidleris [288], after Tinti [337]).

It is usually assumed, for practical considerations, that the in-pile deformation of zirconium alloys consists of the sum (equation 3) of (i) the growth ($\dot{\varepsilon}_{growh}$), (ii) the classical thermally activated out-of-pile creep, or so-called thermal creep ($\dot{\varepsilon}_{thermal-creep}$), and (iii) the irradiation creep ($\dot{\varepsilon}_{irradiation-creep}$), strictly speaking [212] [288] [301] [338].

[3] $\dot{\varepsilon} = \dot{\varepsilon}_{thermal-creep} + \dot{\varepsilon}_{irradiation-creep} + \dot{\varepsilon}_{growth} = \dot{\varepsilon}_{creep} + \dot{\varepsilon}_{growth}$

The creep deformation under irradiation ($\dot{\varepsilon}_{creep}$), which includes both the irradiation creep and the thermal creep, is the total strain substracted from the growth strain. The growth strain is measured on separated samples subjected to the same temperature and neutron flux without applied stress. The 'pure' irradiation creep strain, which is the in-reactor creep substracted from the thermal creep, is not usually computed, since the thermal creep during irradiation cannot be unambiguously defined. However, for low enough stress and/or low enough temperature, the

thermal creep remains low, and the creep strain measured under irradiation should only be due to irradiation creep. In the general case, creep under irradiation is always a combination of thermal creep and irradiation creep.

Several types of mechanical tests [17], such as uniaxial [337] and biaxial loading devices [291], are commonly used to assess the in-reactor creep deformation of zirconium alloys. Another convenient, but indirect, way to assess creep under irradiation is to use bent strips to measure the stress relaxation under irradiation. From stress relaxation, the irradiation creep law can be deduced. This last method has been used by several authors [339] [203].
Recently, the experiment done by Carassou et al. [340] clearly shows the more rapid stress relaxation under irradiation than out of flux of RXA Zy-4 unirradiated samples (Figure 41).

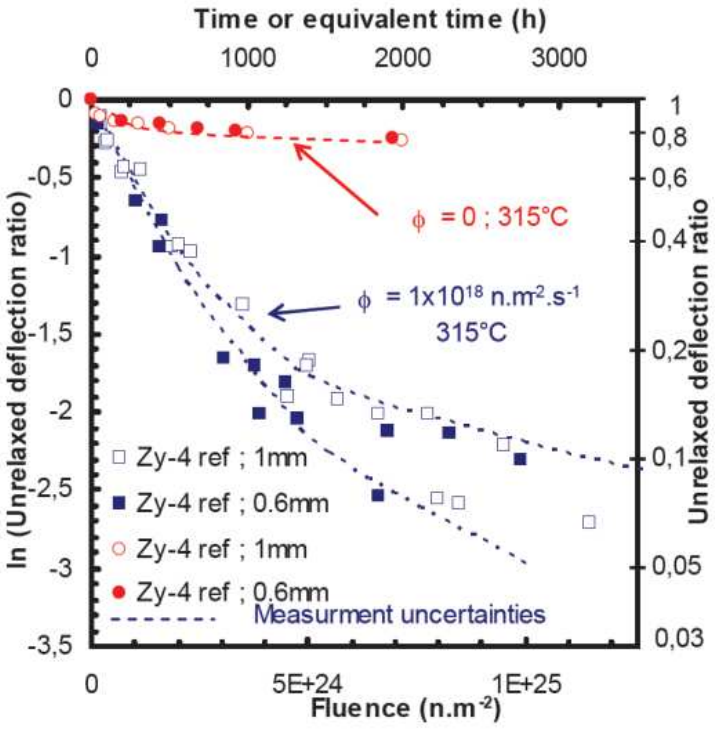

Figure 41: Evolution of the unrelaxed deflection ratio at 315°C of reference RXA Zy-4 as a function of time or fluence for two different imposed deflections (1 and 0.6 mm). For irradiated specimens, equivalent time refers to their measured fluence divided by the maximum flux (10^{18} $n.m^{-2}s^{-1}$). Adapted from Carassou, S., Duguay, C., Yvon, P., Rozenblum, F., Cloué, J.,

Chabretou, V., ... & Audic, K. (2012) Zirconium in the Nuclear Industry: 16th International Symposium. ASTM International.

The creep deformation under irradiation results, in fact, from two antagonistic phenomena. Indeed, while pure irradiation creep is activated by the neutron flux, causing the creep rate to increase, the thermal creep rate is strongly reduced by irradiation due to the irradiation-induced hardening. This phenomenon is often called irradiation-retarded creep as opposed to irradiation creep, which is irradiation induced or irradiation enhanced.
Indeed, as pointed out earlier, irradiation significantly reduces the postirradiation thermal creep [291]. When a preirradiation [288] is conducted before a subsequent creep test conducted under irradiation, the thermal creep component of the deformation under irradiation is reduced. The effect of preirradiation on the reduction of the irradiation creep rate is particularly noticeable for RXA alloys stressed near or above the yield stress of the unirradiated material. However, the hardening effect saturates at fluence of about 4×10^{24} n m^{-2} and is followed by a steady-state creep rate. During stress relaxation tests done on RXA Zircaloy-4 under irradiation by Carassou et al. [340] it is also shown that the first transient of stress relaxation is reduced by the preirradiation, however the steady-state strain rate is not significantly modified by preirradiation. Concerning cold-worked materials, the effect of the preirradiation is lower, according to Fidleris [288]. In the case of CANDU pressure tubes [301] [17], the effect of irradiation-retarded creep is clearly evidenced when measuring the diametral strain along the axial direction of the tube. A peak of diametral strain rate is observed under neutron flux, whereas out-of-flux the diametral strain rate is lower than the in-flux strain rate. At the edge of the fueled zone, where the fast neutron flux is low, a minimum in the diametral strain rate, lower than the out-of-flux strain rate, is observed. This minimum is due to the “suppression” of thermal creep (or irradiation-retarded creep) by radiation damage accumulated at a neutron flux too low to induce significant irradiation creep. This example illustrates the combination of irradiation-retarded creep (thermal creep) and irradiation creep.

In the literature, in-reactor creep is often compared to out-of-reactor creep or laboratory tests. Although this is not often stated clearly, it usually refers (but not always) to the thermal creep of the unirradiated material which is significantly higher than that of the as-irradiated material. It

must also be kept in mind that during postirradiation creep test, recovery of the microstructure may occur. A clear assessment of the respective role of the irradiation-retarded creep and of the irradiation creep, depending on stress and temperature, is thus difficult to do.

The effects of flux, as well as the effect of stress, are usually described by a power correlation. The effect of temperature is described by an Arrhenius equation [269]. The overall in-reactor creep constitutive law can be thus written as (equation 4) [301] [338].

[4]

$$\dot{\varepsilon}_{creep} = K_0 \sigma^n \varphi^p \exp(Q/RT)$$

where $\dot{\varepsilon}_{creep}$ is the strain rate in s^{-1}; σ is the effective stress for thermal creep in MPa; n is the stress exponent; T is the temperature in K; Q is the activation energy in J; R is the gas constant, 8.31 J K^{-1} mol^{-1}; φ is the fast neutron flux in n m^{-2} s^{-1} (E > 1 MeV); p is the flux exponent; and K is a constant in s^{-1} $(MPa)^{-n}(n\ m^{-2}\ s^{-1})^{-p}$. According to various authors [309] [288] the flux exponent (p) has been assigned values ranging from 0.25 to 1. A flux exponent of p = 1 is commonly obtained for CANDU pressure tube deformation [301] [341]. For uniaxial creep tests performed at 280 °C on cold-worked Zy-2, Tinti [337] has obtained a flux exponent increasing from 0.6 to 1.0 with increasing instant flux. The increase of in-reactor creep rate for increasing fast neutron flux has also been clearly evidenced by DeAbreu et al. [342] for Zr2.5Nb alloy. A non-linearity with an exponent slightly lower than one is suggested by these data.
A stress exponent of n = 1 is obtained at temperatures below or equal to 300 °C for low applied stress ($\sigma \leq 100$ MPa). When the temperature increases from 300°C to 400°C the stress exponent increases up to n = 2. As the stress increases, the stress exponent also gradually increases, reaching values up to n = 2 to 3 for stresses ranging between 200 and 400 MPa for cold-worked Zr–2.5% Nb. [288] [341]. A stress exponent n = 1 has been recently found by Walters et al. [343] for stresses up to 160 MPa for small samples representative of Zr2.5Nb pressure tubes. Foster and Baranwal [16] and Foster et al. [344] also obtained, for a SRA zirconium alloy (Zirlo) and a RXA Zr-1%Nb alloy, a linear dependence between the irradiation creep strain and the applied stress (at the same fluence). The effect of temperature on the creep rate can be rationalized by plotting the creep rate in an Arrhenius plot (logarithm of the creep rate vs. inverse

temperature). The activation energy is then the slope obtained in this plot. It can be seen in **Figure 42** that for low temperatures, the creep activation temperature, Q/R, is very low, between 2000 and 5000 K [288] [301]. The irradiation creep at low temperature is therefore nearly athermal. At higher temperatures, the dependence increases rapidly toward values of Q/R of 25 000–30 000 K.

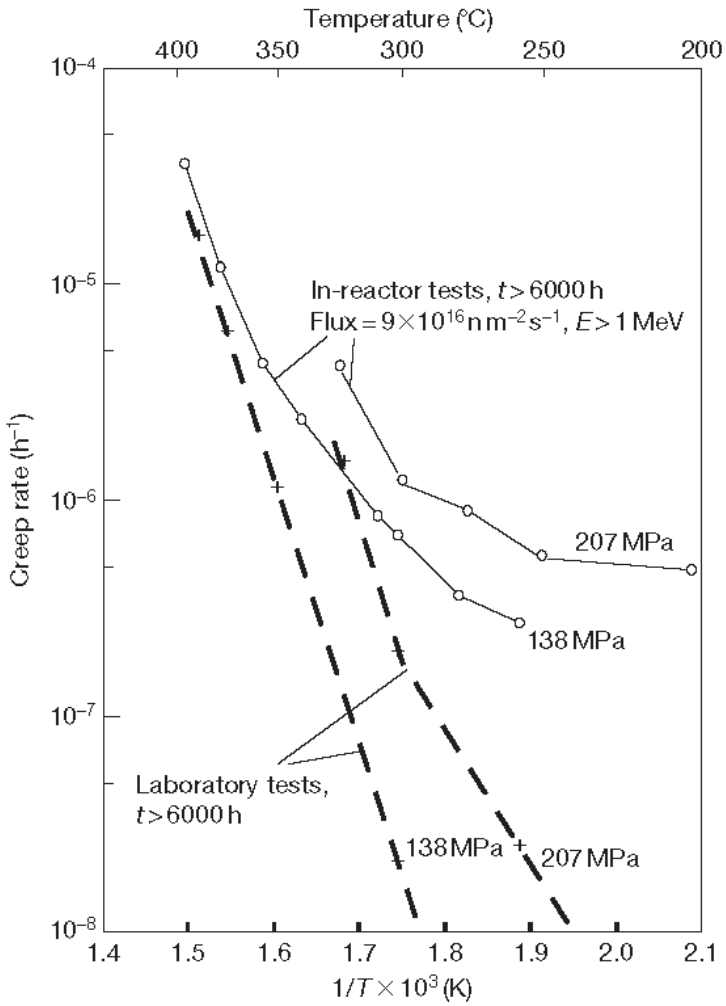

Figure 42 Temperature dependence of laboratory and in-reactor creep rates of cold-worked Zircaloy-2. Adapted from Fidleris, V. *J. Nucl. Mater.* **1988**, *159*, 22–42

These last values are close to the activation temperature measured for thermal creep. These observations prove that for low-temperature regime, mainly 'pure' irradiation creep mechanisms are activated. As the temperature increases, the thermal creep mechanisms become activated,

yielding to activation energy close to the thermal creep values. It is also noticed that the activation energy is higher for RXA Zy-4 than for SRA Zy-4 in the experiments done by Soniak et al [291].

It has also been shown by several authors that while the thermal creep of zirconium alloys is anisotropic, because of the plastic anisotropy of the HCP structure and the strong texture of the material, the irradiation creep remains significantly anisotropic [288]. According to Holt, [312] the anisotropy of irradiation creep is nevertheless slightly lower than that of thermal creep. The irradiation creep rates are usually higher in the direction of working [288]. In the case of rolled thin tubes and thin sheets this leads to a creep rate higher in the axial direction than the transverse direction by a factor of 1.7 to 2.5 [17]. It is also shown by Walters et al. [343] that irradiation anisotropy of Zr2.5Nb cold-worked micro-pressure tubes varies with temperature. Indeed, diametral irradiation creep increases with temperature whereas axial irradiation creep is nearly constant with temperature.

It has been shown by Foster and Baranwal [16] that for a SRA zirconium alloy, the in-reactor creep compliance is the same in tension and compression.

Recently, a very interesting study has been conducted in the Halden reactor [359], allowing the in situ measurement of the deformation of the sample under uniaxial tensile load. In this unique device, the applied load can also be changed during in-reactor operation. Two alloys have been tested all in recrystallization annealed (RXA) state. Using various load histories, the authors have been able to measure the creep rate under a wide range of applied stress.

As reported by several authors [269] [288] [291] [345] the metallurgical state of the zirconium alloy has a significant effect on the in-reactor creep resistance. Indeed, while cold working may improve the thermal creep resistance of Zircaloy in certain test directions and stress range, it increases the in-reactor creep rate appreciably [288] [291]. Nevertheless, the creep sensitivity to the initial dislocation density is significantly lower than the growth sensitivity to the initial dislocation density [312]. Walters et al. [343] also show no clear effect of cold work in the range of 6-26% cold-work strain.

The grain size does not seem to have a significant effect on the creep strength in the range from 1 to 70 μm [288]. However, according to Walters et al. [343] there is a strong dependence on the

mean grain aspect ratio especially when one of the dimension of the grain becomes lower than 1 µm.

In general, the creep strength is increased by solid solution strengthening with oxygen, iron, tin and niobium [288]. The role of tin on the increased resistance of zirconium alloys on thermal creep has been well established by many authors (see for instance [172]). Niobium and oxygen also contribute to the enhanced thermal creep resistance. This has been rationalized by Seibold and Garzarolli [346] who proposed to use a 'SNO' parameter (wt%Sn+2×wt%Nb+6×wt%O) to illustrate the effect of these alloying element on creep. Concerning in-reactor creep, the dependence in this SNO parameter appears to be lower than that of thermal creep. Soniak et al. [291] compared the irradiation creep behavior of RXA Zircaloy-4 and a recrystallized Zr-1%Nb alloy (M5) and found that there is no significant difference in the creep rate. They also showed that by increasing the sulfur content up to 10 ppm in the Zr1%Nb alloy, the irradiation creep strain is slightly reduced, especially for the primary creep.
The effect of hydrogen on irradiation creep has also been studied by Foster et al. [344]. They showed that hydrogen has no significant effect on irradiation creep of the SRA zirconium alloy (Zirlo).

5.01.6.2.2 Irradiation creep: Mechanisms and modelling

Although the creep behavior under irradiation of zirconium alloys is relatively well known, the issue of irradiation creep mechanisms at the origin of this deformation remains an opened question. Many mechanisms for irradiation creep in metals and alloys have been proposed in the literature as reviewed by Nichols [347], Holt [301] [312], Franklin *et al.* [269], Matthews and Finnis [348]. A recent and original critical review of irradiation creep mechanisms can be found in [17]. A nice history of the proposed mechanisms for both zirconium alloys and stainless steels is given by Franklin *et al.* [269]. According to these last authors, irradiation creep mechanisms can fall mainly into two large categories:

1. The mechanisms based on climb-enhanced dislocation glide (or climb-plus-glide) mechanisms, which are essentially a combination of climb of edge dislocations due the absorption of point defects under irradiation and glide resulting in a creep deformation.

For this category of mechanisms, the strain is essentially produced by glide but the strain rate is controlled by the climb.

2. The mechanisms based on stress-induced preferential absorption (SIPA) of point defects by line dislocations arising from different processes. For these mechanisms, the creep deformation results from the climb of edge dislocations under applied stress. The SIPA effect on loops inducing an anisotropic growth of loops, depending on the habit plane, resulting in an additional creep strain, also falls into this last category.

The SIPA mechanism is based on the fact that, under an applied stress, the absorption bias of an edge dislocation becomes dependent on the orientation of the Burgers vector with respect to the direction of the stress [269] [348]. This phenomenon can arise from two distinct elementary processes. The first one is the result of the diffusion that becomes anisotropic under an applied stress. This is often referred to as elasto-diffusion or SIPA-AD, for Anisotropic Diffusion. The second one, which can be referred to as SIPA-I, is the effect the applied stress on the elastic interaction difference (EID) between a point defect, either vacancy or interstitial and a dislocation. Indeed, as described previously, due to a higher relaxation volume, the sink strength of an edge dislocation toward SIAs is higher than toward vacancies. This difference in sink strength is the bias of the edge dislocation. It can be shown that a dislocation with a Burgers vector parallel to the applied stress exhibits a higher bias toward SIAs than a dislocation with a Burgers vector perpendicular to the applied stress. Therefore, under irradiation, the net flux of SIAs (SIA flux minus vacancy flux) toward dislocations, with Burgers vector parallel to the applied stress, is higher than the net flux of SIAs toward dislocations with Burgers vector perpendicular to the applied stress. This difference in the absorption of point defects by different types of dislocations leads to dislocation climb, resulting in a creep strain. The SIPA creep rate is thus insensitive to the grain size but is sensitive to the dislocation network.
Recently, Adamson et al. [17] consider that the SIPA-I mechanism on dislocations is not relevant to zirconium alloys. They prefer to separate irradiation creep mechanisms into two broader families: i) climb-enhanced dislocation glide, for which strain is the result of dislocation glide, and ii) mass transport based mechanisms, that is, all the mechanisms for which strain arises from point defect diffusion, such as SIPA-AD (or elasto-diffusion). These two types of mechanisms

are probably simultaneously active with relative proportion depending on the applied stress, the neutron flux and the irradiation temperature.

It is difficult to assess which mechanism is actually relevant based only on macroscopic data since the same data set can be interpreted using different assumed mechanisms. This is why detailed studies with controlled initial microstructural parameters, fine post-irradiation examinations at nano-scale, by TEM, or even in situ experiments at nano-scale are needed. Unfortunately, this type of studies are very scarce in the literature. In the following, some experimental evidences that could help to choose between one of these mechanisms, have been listed.

Experimental evidence for the SIPA-AD (elasto-diffusion) on grain boundaries in zirconium alloys

According to Fidleris [288], for RXA Zy-2 with grain size from 6 to 20 µm there is very little effect of grain size on irradiation creep. This suggest that for this grain size range, the SIPA-AD mechanism is not effective. Similar studies have been done for cold worked Zy-2 and Zr2.5Nb under in-reactor stress relaxation. These materials have small grains but also contain a high dislocation density. In that case, it is shown that there is little effect on grain size in the range 1 to 70 µm. Recently, the work of Walters et al. [343] shows that the grain shape, for submicronic grain thickness, in one direction, has a strong influence on diametral (transverse) creep of Zr2.5Nb alloy. Indeed, for radial grain thickness ranging between 0.25 to 0.4 µm and transverse grain thickness larger than 1 µm, with aspect ratio ranging between 0.25 up to 0.45 (the aspect ratio being the radial thickness divided by the transverse thickness), the lower the aspect ratio (smaller grain thickness in the transverse direction), the higher is the diametral strain rate. According to the authors, this is well explained by the SIPA-AD mechanism on grain boundaries. Furthermore, the authors do not see any significant effect of the dislocation density. The fact that the diametral (transverse) irradiation creep rate of SRA Zy-4 is higher than the creep rate of RXA Zy-4, as shown by Soniak et al. [291] could be well explained by the SIPA-AD mechanism. Indeed, the grain thickness along the transverse direction of SRA Zy-4 is submicronic, whereas it is typically of 6 µm for RXA Zy-4.

Experimental evidence for the SIPA mechanism on loops in zirconium alloys:
Usually, no significant effect of stress under irradiation on the <a>-loop microstructure can be noticed. From our knowledge, the <a>-loop size and density, during in-reactor irradiation conducted at 350°C under an applied stress, are the same as the one conducted without applied stress. However, early experiments conducted at 260°C on crystal bar zirconium using proton irradiation by Faulkner and McElroy [349], have shown that an applied stress increases the mean diameter of $\langle a \rangle$ loops without affecting the density. From this observation, they suggest that the SIPA (AD or I) mechanism is efficient in their experiment. This deformation mechanism is supported by the evidence of strain recovery measured during post-irradiation annealing [350]. Indeed, when the loops anneal out, the associated strain is recovered. According to Nichols [350] this is thus a likely deformation mechanism for zirconium alloys under low applied stress. However, the growth of $\langle a \rangle$ loops under an applied stress could explain the measured creep strain only for low strain levels. This creep strain should remain limited since the $\langle a \rangle$ loop density and mean loop diameter saturate at relatively low doses. Similar discussion is given by MacEwen and Fidleris [351]. These authors have analyzed the irradiation creep strain rate of zirconium single crystal and compared it to the <a>-loop density measured by TEM. They showed that the strain rate resulting directly from the growth of prismatic loops is not a significant portion of the observed creep rate.
Recently, the role of an applied stress on <c>-loop growth has also been investigated using heavy ion irradiation [122]. Only a small effect of stress, probably within the scatter of experimental data, is noticed, proving that the SIPA effect on <c>-loops is very small. This may shed doubts about SIPA type mechanisms.

Experimental evidence for the SIPA effect on dislocations in zirconium alloys:
The climb of edge dislocations under irradiation by the SIPA mechanism could be a likely mechanism to explain irradiation creep deformation. The fact that the creep strain rate increases, slightly, as the initial dislocation density increases can be considered as a hint for this mechanism. However, in RXA zirconium alloys, the initial dislocation density is very low. The generation of a dislocation network is therefore needed to account for the measured deformation. It is possible that $\langle a \rangle$ loops coalescence occurs, resulting in the creation of a dislocation network that is able to climb under stress [348] [352]. However, this network is clearly observed

only after irradiation at 400 °C [70]. At lower temperatures, it is very difficult to observe this network due to the high density of loops. Other types of dislocation sources, such as Bardeen–Herring sources [283], can also be activated under both irradiation and applied stress, leading to the creation of a dislocation network that undergoes a SIPA mechanism. For cold-worked zirconium alloys, such as SRA Zircaloys or cold-worked Zr–2.5Nb alloy [301], the SIPA mechanism on the initial dislocations is a likely mechanism for irradiation creep. It should also be pointed out that, since dislocations climb toward grain boundaries or toward other dislocations, recovery of the initial dislocation network occurs. In order to maintain a steady-state creep rate, multiplication of dislocations should occur either via loop coalescence or via dislocation sources, as discussed previously.
It must also be recalled that there is a very high loop density. These loops act as obstacles against dislocation climb. Dislocations must therefore overcome these obstacles to explain the measured strain.

Experimental evidence for climb-enhanced glide of dislocations:
In the case of zirconium alloys, climb-enhanced glide has long been the preferred mechanism [269] [312]. According to Holt [312], the creep anisotropy of cold-worked zirconium alloys computed from the SIPA mechanism assuming only $\langle a \rangle$ type dislocations is not in agreement with the experimental anisotropy. The anisotropy computed from the climb-enhanced glide mechanism assuming 80% prism slip and 20% basal slip is in good agreement with the experimental anisotropy, demonstrating that climb-enhanced glide mechanism is probably the effective mechanism. Holt also claims that the low sensitivity of irradiation creep to network dislocation density agrees with a climb-plus-glide model in which dislocations, released from the cell walls by climb, glide a distance equal to the cell size [312]. The transient increase in creep rate, observed during reactor shut-down by MacEwen and Fidleris [353], has also been considered as a proof that flux-enhanced dislocation climb is the rate controlling mechanism for in-reactor creep.

Experimental evidence for interactions between dislocation and loops during irradiation creep
It should also be pointed out that in order to explain the observed creep rate, some mechanisms must be activated that allow the dislocations to overcome the high density of dislocation loops

during their climb or glide motion, even for low applied stress. It is possible, as observed by MacEwen and Fidleris [351] in the case of Zr single crystal, that the gliding dislocations are able to clear the loops during in-pile deformation, leading to the dislocation channeling mechanism. Recently, Gaumé et al. [354] have shown, using in situ straining in a TEM under heavy ion irradiation of RXA Zircaloy-4, that under a high applied stress, dislocations can glide under irradiation. Furthermore, they proved that when the ion beam is off the dislocations are pinned on irradiation defects, such as small loops, but when the ion beam is on, the dislocations are released from their pinning points. This release occurs either by a direct effect of the cascade on the pinning point or by the climb of dislocations to overcome the pinning points.

All these mechanisms probably occur in series, as proposed by Nichols [355], explaining the evolution of the stress dependency as the stress increases. Indeed, according to this author, for zero applied stress, growth of zirconium occurs, and then as the stress increases, ⟨ *a*⟩ loop alignment occurs (SIPA on loops). For higher stress, the climb of line dislocations via the SIPA mechanism takes place, and then the dislocation climb and glide process occurs at even higher stress. It is also possible that for small grains, with thickness smaller than 1 µm in one direction, elasto-diffusion (SIPA-AD) occurs toward grain boundaries. For very high stress, just below the YS of the irradiated material, dislocations glide assisted by the release from obstacles under cascade. Loops may also be cleared out by gliding dislocations leading to dislocation channeling.

In the case of the SIPA mechanism applied to dislocation climb (and not to loop growth), it has been assessed that it is a different mechanism than the thermal climb of dislocations under stress [348] [356] [357] [358]. However, in the general case, it is in fact difficult to clearly distinguished thermal creep mechanisms from irradiation creep mechanisms, especially the radiation-enhanced mechanisms. Thus, irradiation creep is usually strongly coupled to thermal creep. Indeed, these mechanisms all imply dislocation loops, slip and climb of line dislocations, and point-defect bulk diffusion toward these defects. For the same reason, irradiation growth is also probably coupled to irradiation creep [269] [300], as swelling and irradiation creep are coupled in stainless steel [348]. Nevertheless, the simple assumption of two separable deformation components, at the macroscopic scale, has proved to hold correctly for the results given in the literature [338] [301].

The coupling between irradiation creep and growth also arises at the polycrystalline scale, since when growth occurs at the grain scale, strain incompatibilities between grains appear, leading to internal stresses and thus to creep at the grain scale. As discussed in the growth section, this has been studied by using polycrystalline models using simple irradiation creep single-crystal behavior [327] [333]. Other authors have proposed complex rate theory based models for irradiation creep, sometimes coupled with polycrystalline models [323] [343]. However, none of these models has met a general agreement in the community, presumably because of the lack of experimental evidences available especially from a microscopic point of view.

5.01.7 Outlook

Concerning damage creation and point-defect cluster formation, improvement in the knowledge of anisotropic diffusion of SIAs as well as better understanding of the microstructure of vacancy and interstitial $\langle a \rangle$ loops and basal $\langle c \rangle$ vacancy loops has to be aimed at. Redistribution of alloying elements and the formation of Nb nano-precipitates under irradiation are also issues of interest. Charged particle irradiation associated with fine experimental analyses of the irradiation microstructure (in situ irradiation in TEM, high-resolution TEM, synchrotron radiation analyses, atom probe tomography, etc.) should bring new insight on the aforementioned points. These advanced experimental techniques should be combined with multiscale modeling, from ab initio calculations to more mesoscopic modeling tools. However, detailed experiments on neutron irradiated samples are still needed since extrapolation of results obtained in charged particle experiments is not always simple.

Concerning the mechanical behavior of Zr alloys after irradiation, small-scale experiments after charged particle irradiation are probably one of the best way to gain easily a better understanding. Furthermore, multiscale modeling of the postirradiation deformation with a better understanding of the dislocation channeling are needed. Moreover, better understanding of the postirradiation creep deformation mechanisms is also needed. However, for all these issues, neutron irradiated samples must remain the reference and efforts must be made to conduct advanced testing, involving for instance non-monotonous tests, and microstructural characterizations on neutron irradiated samples.

The last point concerns the deformation mechanisms under irradiation. The mechanisms responsible for growth are still not well understood. Only the correlation between <c>-loop density and accelerated growth strain is qualitatively well established. Further efforts are therefore needed in that field. As for irradiation creep, the basic questions are still without answer: What are the irradiation creep deformation mechanisms? What is the coupling between the deformation under irradiation and the thermal creep and growth? Progress has to be made especially using in situ deformation devices under irradiation, coupled with modeling approaches.

Another point that has not been mentioned all along this chapter concerns the coupling between the radiation effects and the environment. For instance, how the radiation effects affect the hydrogen embrittlement, especially when considering the transportation and storage of the spent fuel assemblies? How the radiation effects influence the stress corrosion cracking during pellet-cladding interaction?

What about the radiation effects in the context of an accidental scenario such as Loss of Coolant Accident or Reactivity Initiated Accident? These are also interesting and important questions worth to be looked at from the application point of view.

Change History Statement – “December 2019. F. Onimus updated the text of this entire chapter, trying to achieve comprehensiveness for these past ten years of research on this subject. F. Onimus added figures 7, 8, 11, 27, 28, 37, 40, 41. S. Doriot updated the text of section 4 and added figures 15, 16, 17, 18, 19, 20, 21, 22, 23, 24, 25. J.-L Béchade and R. Konings provided careful readings and corrections to this entire article”.

References

[1] J. R. Beyster, M. Walt, and E. W. Salmi, "Interaction of 1.0-, 1.77-, 2.5-, 3.25-, and 7.0-Mev Neutrons with Nuclei," *Phys. Rev.*, vol. 104, no. 5, pp. 1319–1331, Dec. 1956.

[2] P. Guenther, A. Smith, and J. Whalen, "Zr90andZr92: Neutron total and scattering cross sections," *Phys. Rev. C*, vol. 12, no. 6, pp. 1797–1808, Dec. 1975.

[3] H. H. Neely, "Damage rate and recovery measurements on zirconium after electron irradiation at low temperatures," *Radiat. Eff.*, vol. 3, no. 2, pp. 189–201, Jan. 1970.

[4] M. Biget, F. Maury, P. Vajda, A. Lucasson, and P. Lucasson, "Production and mutual annihilation of frenkel pairs in low temperature irradiated zirconium," *Radiat. Eff.*, vol. 7, no. 3–4, pp. 223–229, Feb. 1971.

[5] M. Griffiths, "Displacement energies for Zr measured in a HVEM," *J. Nucl. Mater.*, vol. 165, no. 3, pp. 315–317, Jun. 1989.

[6] G. J. Ackland, S. J. Wooding, and D. J. Bacon, "Defect, surface and displacement-threshold properties of α-zirconium simulated with a many-body potential," *Philos. Mag. A*, vol. 71, no. 3, pp. 553–565, Mar. 1995.

[7] F. Gao, D. J. Bacon, L. M. Howe, and C. B. So, "Temperature-dependence of defect creation and clustering by displacement cascades in α-zirconium," *J. Nucl. Mater.*, vol. 294, no. 3, pp. 288–298, Apr. 2001.

[8] G. S. Was, *Fundamentals of Radiation Materials Science: Metals and Alloys*. New York: Springer, 2007.

[9] M. J. Norgett, M. T. Robinson, and I. M. Torrens, "A proposed method of calculating displacement dose rates," *Nucl. Eng. Des.*, vol. 33, no. 1, pp. 50–54, Aug. 1975.

[10] S. J. Zinkle and B. N. Singh, "Analysis of displacement damage and defect production under cascade damage conditions," *J. Nucl. Mater.*, vol. 199, no. 3, pp. 173–191, Feb. 1993.

[11] E. Balanzat and S. Bouffard, "Basic Phenomena of the Particle-Matter Interaction," *Solid State Phenom.*, vol. 30–31, pp. 7–74, Jan. 1992.

[12] L. R. Greenwood and R. K. Smither, "SPECTER: neutron damage calculations for materials irradiations," Office of Scientific and Technical Information (OSTI), Jan. 1985.

[13] L. Walters, S. R. Douglas, and M. Griffiths, "Equivalent Radiation Damage in Zirconium Irradiated in Various Reactors," *Zircon. Nucl. Ind. 18th Int. Symp.*, vol. ASTM STP 1597, pp. 676–690, Jan. 2018.

[14] V. Shishov *et al.*, "Influence of Structure—Phase State of Nb Containing Zr Alloys on Irradiation-Induced Growth," *J. ASTM Int.*, vol. 2, no. 8, p. 12431, 2005.

[15] S. Doriot *et al.*, "Microstructural Evolution of Q12TM Alloy Irradiated in PWRs and Comparison with Other Zr Base Alloys," *Zircon. Nucl. Ind. 18th Int. Symp.*, vol. ASTM STP 1597, pp. 823–856, Jan. 2018.

[16] J. P. Foster, R. Baranwal, P. Barberis, and S. W. Dean, "ZIRLO® Irradiation Creep Stress Dependence in Compression and Tension," *J. ASTM Int.*, vol. 8, no. 3, p. 103297, 2011.

[17] R. B. Adamson, C. E. Coleman, and M. Griffiths, "Irradiation creep and growth of zirconium alloys: A critical review," *J. Nucl. Mater.*, vol. 521, pp. 167–244, Aug. 2019.

[18] C. H. Woo and B. N. Singh, "Production bias due to clustering of point defects in irradiation-induced cascades," *Philos. Mag. A*, vol. 65, no. 4, pp. 889–912, Apr. 1992.

[19] C. H. Woo, A. A. Semenov, and B. N. Singh, “Analysis of microstructural evolution driven by production bias,” *J. Nucl. Mater.*, vol. 206, no. 2–3, pp. 170–199, Nov. 1993.
[20] V. G. Kapinos, Y. N. Osetskii, and P. A. Platonov, “Simulation of defect cascade collapse in hcp zirconium,” *J. Nucl. Mater.*, vol. 184, no. 2, pp. 127–143, Sep. 1991.
[21] S. . Wooding, L. . Howe, F. Gao, A. . Calder, and D. . Bacon, “A molecular dynamics study of high-energy displacement cascades in α-zirconium,” *J. Nucl. Mater.*, vol. 254, no. 2–3, pp. 191–204, Apr. 1998.
[22] S. R. Macewen, R. H. Zee, R. C. Birtcher, and C. Abkomeit, “Point defect production and annihilation in neutron-irradiated zirconium,” *J. Nucl. Mater.*, vol. 123, no. 1–3, pp. 1036–1040, May 1984.
[23] R. E. Voskoboinikov, Y. N. Osetsky, and D. J. Bacon, “Identification and morphology of point defect clusters created in displacement cascades in α-zirconium,” *Nucl. Instrum. Methods Phys. Res. Sect. B Beam Interact. Mater. At.*, vol. 242, no. 1–2, pp. 530–533, Jan. 2006.
[24] M. Christensen *et al.*, “Diffusion of point defects, nucleation of dislocation loops, and effect of hydrogen in hcp-Zr: Ab initio and classical simulations,” *J. Nucl. Mater.*, vol. 460, pp. 82–96, May 2015.
[25] G. M. Hood, “Point defect diffusion in α-Zr,” *J. Nucl. Mater.*, vol. 159, pp. 149–175, Oct. 1988.
[26] W. Frank, “Rapid-pair-enhanced diffusion in α-Zr and its integration into the point-defect scenario in h.c.p. metals,” *Philos. Mag. A*, vol. 63, no. 5, pp. 897–913, May 1991.
[27] J. Horváth, F. Dyment, and H. Mehrer, “Anomalous self-diffusion in a single crystal of α-zirconium,” *J. Nucl. Mater.*, vol. 126, no. 3, pp. 206–214, Nov. 1984.
[28] D. L. Douglass, *The Metallurgy of Zirconium*, Atomic Energy Review. Vienna: IAEA, 1971.
[29] G. . Hood and R. . Schultz, “Tracer diffusion in α-Zr,” *Acta Metall.*, vol. 22, no. 4, pp. 459–464, Apr. 1974.
[30] G. M. Hood, R. J. Schultz, and J. A. Jackman, “The recovery of single crystal α-Zr from low temperature electron irradiation — a positron annihilation spectroscopy study,” *J. Nucl. Mater.*, vol. 126, no. 1, pp. 79–82, Sep. 1984.
[31] G. M. Hood, “Diffusion and vacancy properties of α-Zr,” *J. Nucl. Mater.*, vol. 139, no. 3, pp. 179–184, Jul. 1986.
[32] W. Frank, “Intrinsic point defects in hexagonal close-packed metals,” *J. Nucl. Mater.*, vol. 159, pp. 122–148, Oct. 1988.
[33] M. Lubbehusen, K. Vieregge, G. M. Hood, H. Mehrer, and C. Herzig, “Self-diffusion in α-Zr single crystals,” *J. Nucl. Mater.*, vol. 182, pp. 164–169, May 1991.
[34] G. M. Hood, H. Zou, D. Gupta, and R. J. Schultz, “α-Zr self-diffusion anisotropy,” *J. Nucl. Mater.*, vol. 223, no. 2, pp. 122–125, May 1995.
[35] D. J. Bacon, “A review of computer models of point defects in hcp metals,” *J. Nucl. Mater.*, vol. 159, pp. 176–189, Oct. 1988.
[36] D. J. Bacon, “Point defects and clusters in the hcp metals: their role in the dose transition,” *J. Nucl. Mater.*, vol. 206, no. 2–3, pp. 249–265, Nov. 1993.
[37] O. Le Bacq, F. Willaime, and A. Pasturel, “Unrelaxed vacancy formation energies in group-IV elements calculated by the full-potential linear muffin-tin orbital method: Invariance with crystal structure,” *Phys. Rev. B*, vol. 59, no. 13, pp. 8508–8515, Apr. 1999.

[38] R. C. Pasianot and A. M. Monti, “A many body potential for α-Zr. Application to defect properties,” *J. Nucl. Mater.*, vol. 264, no. 1–2, pp. 198–205, Jan. 1999.
[39] R. . Pasianot, A. . Monti, G. Simonelli, and E. . Savino, “Computer simulation of SIA migration in bcc and hcp metals,” *J. Nucl. Mater.*, vol. 276, no. 1–3, pp. 230–234, Jan. 2000.
[40] Y. N. Osetsky, D. J. Bacon, and N. de Diego, “Anisotropy of point defect diffusion in alpha-zirconium,” *Metall. Mater. Trans. A*, vol. 33, no. 3, pp. 777–782, Mar. 2002.
[41] C. H. Woo and X. Liu, “Atomistic calculation of point-defect diffusion anisotropy and irradiation growth in α-zirconium,” *Philos. Mag.*, vol. 87, no. 16, pp. 2355–2369, Jun. 2007.
[42] F. Willaime, “Ab initio study of self-interstitials in hcp-Zr,” *J. Nucl. Mater.*, vol. 323, no. 2–3, pp. 205–212, Dec. 2003.
[43] C. Domain and A. Legris, “Ab initio atomic-scale determination of point-defect structure in hcp zirconium,” *Philos. Mag.*, vol. 85, no. 4–7, pp. 569–575, Feb. 2005.
[44] C. Domain, “Ab initio modelling of defect properties with substitutional and interstitials elements in steels and Zr alloys,” *J. Nucl. Mater.*, vol. 351, no. 1–3, pp. 1–19, Jun. 2006.
[45] G. Vérité, F. Willaime, and C. C. Fu, “Anisotropy of the Vacancy Migration in Ti, Zr and Hf Hexagonal Close-Packed Metals from First Principles,” *Solid State Phenom.*, vol. 129, pp. 75–81, Nov. 2007.
[46] G. D. Samolyuk, A. V. Barashev, S. I. Golubov, Y. N. Osetsky, and R. E. Stoller, “Analysis of the anisotropy of point defect diffusion in hcp Zr,” *Acta Mater.*, vol. 78, pp. 173–180, Oct. 2014.
[47] C. Varvenne, O. Mackain, and E. Clouet, “Vacancy clustering in zirconium: An atomic-scale study,” *Acta Mater.*, vol. 78, pp. 65–77, Oct. 2014.
[48] R. A. Pérez and M. Weissmann, “Ab-initio approach to the effect of Fe on the diffusion in hcp Zr,” *J. Nucl. Mater.*, vol. 374, no. 1–2, pp. 95–100, Feb. 2008.
[49] R. C. Pasianot, R. A. Pérez, V. P. Ramunni, and M. Weissmann, “Ab initio approach to the effect of Fe on the diffusion in hcp Zr II: The energy barriers,” *J. Nucl. Mater.*, vol. 392, no. 1, pp. 100–104, Jul. 2009.
[50] R. Johnson, J. Beeler, and J. Lee, “Interatomic Potentials and Crystalline Defects,” *AIME N. Y.*, p. 165, 1981.
[51] G. Vérité, C. Domain, C.-C. Fu, P. Gasca, A. Legris, and F. Willaime, “Self-interstitial defects in hexagonal close packed metals revisited: Evidence for low-symmetry configurations in Ti, Zr, and Hf,” *Phys. Rev. B*, vol. 87, no. 13, Apr. 2013.
[52] C. H. Woo, H. Huang, and W. J. Zhu, “Low-dimension self-interstitial diffusion in α-Zr,” *Appl. Phys. Mater. Sci. Process.*, vol. 76, no. 1, pp. 101–106, Jan. 2003.
[53] M. Christensen *et al.*, “Effect of Hydrogen on Dimensional Changes of Zirconium and the Influence of Alloying Elements: First-Principles and Classical Simulations of Point Defects, Dislocation Loops, and Hydrides,” *Zircon. Nucl. Ind. 17th Vol.*, vol. ASTM STP 1543, pp. 55–92, Jun. 2014.
[54] A. Barbu and G. Martin, “Radiation Effects in Metals and Alloys,” *Solid State Phenom.*, vol. 30–31, pp. 179–228, Jan. 1992.
[55] C. H. Woo, “Theory of irradiation deformation in non-cubic metals: Effects of anisotropic diffusion,” *J. Nucl. Mater.*, vol. 159, pp. 237–256, Oct. 1988.
[56] A. V. Barashev, S. I. Golubov, and R. E. Stoller, “Theoretical investigation of microstructure evolution and deformation of zirconium under neutron irradiation,” *J. Nucl. Mater.*, vol. 461, pp. 85–94, Jun. 2015.

[57] D. O. Northwood *et al.*, “Characterization of neutron irradiation damage in zirconium alloys — an international ‘round-robin’ experiment,” *J. Nucl. Mater.*, vol. 79, no. 2, pp. 379–394, Feb. 1979.
[58] M. Griffiths, “A review of microstructure evolution in zirconium alloys during irradiation,” *J. Nucl. Mater.*, vol. 159, pp. 190–218, Oct. 1988.
[59] T. D. Gulden and I. M. Bernstein, “Dislocation loops in irradiated zirconium,” *Philos. Mag.*, vol. 14, no. 131, pp. 1087–1091, Oct. 1966.
[60] P. M. Kelly and R. G. Blake, “The characterization of dislocation loops in neutron irradiated zirconium,” *Philos. Mag.*, vol. 28, no. 2, pp. 415–426, Aug. 1973.
[61] D. O. Northwood, V. Fidleris, R. W. Gilbert, and G. J. C. Carpenter, “Dislocation loop generation and irradiation growth in a zirconium single crystal,” *J. Nucl. Mater.*, vol. 61, no. 2, pp. 123–130, Aug. 1976.
[62] A. Jostsons, P. M. Kelly, and R. G. Blake, “The nature of dislocation loops in neutron irradiated zirconium,” *J. Nucl. Mater.*, vol. 66, no. 3, pp. 236–256, May 1977.
[63] D. Northwood, “Irradiation damage in zirconium and its alloys,” *At. Energy Rev.*, vol. 15, no. 4, pp. 547–610, 1977.
[64] R. W. Gilbert, K. Farrell, and C. E. Coleman, “Damage structure in zirconium alloys neutron irradiated at 573 to 923 k,” *J. Nucl. Mater.*, vol. 84, no. 1–2, pp. 137–148, Oct. 1979.
[65] M. Griffiths, R. W. Gilbert, V. Fidleris, R. P. Tucker, and R. B. Adamson, “Neutron damage in zirconium alloys irradiated at 644 to 710 k,” *J. Nucl. Mater.*, vol. 150, no. 2, pp. 159–168, Oct. 1987.
[66] M. Griffiths, “Microstructure evolution in h.c.p. metals during irradiation,” *Philos. Mag. A*, vol. 63, no. 5, pp. 835–847, May 1991.
[67] M. Griffiths, “Evolution of microstructure in hcp metals during irradiation,” *J. Nucl. Mater.*, vol. 205, pp. 225–241, Oct. 1993.
[68] M. Griffiths, J. Mecke, and J. Winegar, “Evolution of Microstructure in Zirconium Alloys During Irradiation,” *Zircon. Nucl. Ind. Elev. Int. Symp.*, vol. ASTM STP 1295, pp. 580–602, 1996.
[69] T. Seymour *et al.*, “Evolution of dislocation structure in neutron irradiated Zircaloy-2 studied by synchrotron x-ray diffraction peak profile analysis,” *Acta Mater.*, vol. 126, pp. 102–113, Mar. 2017.
[70] A. Jostsons, R. G. Blake, J. G. Napier, P. M. Kelly, and K. Farrell, “Faulted loops in neutron-irradiated zirconium,” *J. Nucl. Mater.*, vol. 68, no. 3, pp. 267–276, Nov. 1977.
[71] A. Jostsons, P. Kelly, R. Blake, and K. Farrell, “Neutron Irradiation-Induced Defect Structures in Zirconium,” *Eff. Radiat. Struct. Mater.*, vol. ASTM STP 683, pp. 46–61, 1979.
[72] B. V. Cockeram, R. W. Smith, K. J. Leonard, T. S. Byun, and L. L. Snead, “Development of microstructure and irradiation hardening of Zircaloy during low dose neutron irradiation at nominally 358°C,” *J. Nucl. Mater.*, vol. 418, no. 1–3, pp. 46–61, Nov. 2011.
[73] S. Doriot *et al.*, “Microstructural Evolution of M5 Alloy Irradiated in PWRs up to High Fluences—Comparison With Other Zr-Based Alloys,” *Zircon. Nucl. Ind. 17th Vol.*, vol. ASTM STP 1543, pp. 759–799, Sep. 2014.
[74] V. Shishov *et al.*, “Influence of Zirconium Alloy Chemical Composition on Microstructure Formation and Irradiation Induced Growth,” *Zircon. Nucl. Ind. 13th Int. Symp.*, vol. ASTM STP 1423, pp. 758–779, 2002.
[75] W. . Bell, “Corduroy contrast observations in neutron-irradiated zirconium and zircaloy,” *J. Nucl. Mater.*, vol. 55, no. 1, pp. 14–22, Jan. 1975.

[76] P. M. Kelly, R. G. Blake, and A. Jostsons, “An interpretation of corduroy contrast in neutron irradiated zirconium,” *J. Nucl. Mater.*, vol. 59, no. 3, pp. 307–315, Mar. 1976.
[77] G. J. C. Carpenter and J. F. Watters, “A study of electron irradiation damage in Zirconium using a high voltage electron microscope,” *J. Nucl. Mater.*, vol. 96, no. 3, pp. 213–226, Feb. 1981.
[78] C. Hellio, C. H. de Novion, and L. Boulanger, “Influence of alloying elements on the dislocation loops created by Zr+ ion or by electron irradiation in α-zirconium,” *J. Nucl. Mater.*, vol. 159, pp. 368–378, Oct. 1988.
[79] M. Griffiths, M. H. Loretto, and R. E. Smallman, “Electron damage in zirconium - II,” *J. Nucl. Mater.*, vol. 115, no. 2–3, pp. 313–322, Apr. 1983.
[80] M. Griffiths, M. H. Loretto, and R. E. Smallman, “Electron damage in zirconium - I,” *J. Nucl. Mater.*, vol. 115, no. 2–3, pp. 323–330, Apr. 1983.
[81] S. N. Buckley and S. A. Manthorpe, “Dislocation loop nucleation and growth in zirconium-2.5 wt% niobium alloy during 1 MeV electron irradiation,” *J. Nucl. Mater.*, vol. 90, no. 1–3, pp. 169–174, May 1980.
[82] M. Griffiths, R. C. Styles, C. H. Woo, F. Phillipp, and W. Frank, “Study of point defect mobilities in zirconium during electron irradiation in a high-voltage electron microscope,” *J. Nucl. Mater.*, vol. 208, no. 3, pp. 324–334, Feb. 1994.
[83] H. NAKAMICHI, C. KINOSHITA, K. YASUDA, and S. FUKADA, “Formation and Growth Process of Dislocation Loops in Zircaloys under Electron Irradiation.,” *J. Nucl. Sci. Technol.*, vol. 34, no. 11, pp. 1079–1086, 1997.
[84] M. Gaumé, F. Onimus, L. Dupuy, O. Tissot, C. Bachelet, and F. Mompiou, “Microstructure evolution of recrystallized Zircaloy-4 under charged particles irradiation,” *J. Nucl. Mater.*, vol. 495, pp. 516–528, Nov. 2017.
[85] D. Lee and E. F. Koch, “Irradiation damage in Zircaloy-2 produced by high-dose ion bombardment,” *J. Nucl. Mater.*, vol. 50, no. 2, pp. 162–174, Mar. 1974.
[86] R. Adamson, W. Bell, and D. Lee, “Use of Ion Bombardment to Study Irradiation Damage in Zirconium Alloys,” *Zircon. Nucl. Appl.*, pp. 215–228, 1974.
[87] F. Onimus, L. Dupuy, and F. Mompiou, “In situ TEM observation of interactions between gliding dislocations and prismatic loops in Zr-ion irradiated zirconium alloys,” *Prog. Nucl. Energy*, vol. 57, pp. 77–85, May 2012.
[88] Y. Idrees, Z. Yao, M. A. Kirk, and M. R. Daymond, “In situ study of defect accumulation in zirconium under heavy ion irradiation,” *J. Nucl. Mater.*, vol. 433, no. 1–3, pp. 95–107, Feb. 2013.
[89] L. Fournier, A. Serres, Q. Auzoux, D. Leboulch, and G. S. Was, “Proton irradiation effect on microstructure, strain localization and iodine-induced stress corrosion cracking in Zircaloy-4,” *J. Nucl. Mater.*, vol. 384, no. 1, pp. 38–47, Jan. 2009.
[90] A. Harte *et al.*, “The effect of matrix chemistry on dislocation evolution in an irradiated Zr alloy,” *Acta Mater.*, vol. 130, pp. 69–82, May 2017.
[91] M. Topping *et al.*, “The effect of irradiation temperature on damage structures in proton-irradiated zirconium alloys,” *J. Nucl. Mater.*, vol. 514, pp. 358–367, Feb. 2019.
[92] L. Mansur, “Theory of transitions in dose dependence of radiation effects in structural alloys,” *J. Nucl. Mater.*, vol. 206, no. 2–3, pp. 306–323, 1993.
[93] M. Topping *et al.*, “The Effect of Iron on Dislocation Evolution in Model and Commercial Zirconium Alloys,” *Zircon. Nucl. Ind. 18th Int. Symp.*, vol. ASTM STP 1597, pp. 796–822, Jan. 2018.

[94] C. Dai, P. Saidi, M. Topping, L. K. Béland, Z. Yao, and M. R. Daymond, "A mechanism for basal vacancy loop formation in zirconium," *Scr. Mater.*, vol. 172, pp. 72–76, Nov. 2019.
[95] H. Föll and M. Wilkens, "Transmission electron microscope studies of dislocation loops in heavy-ion irradiated H.C.P. cobalt," *Phys. Status Solidi A*, vol. 39, no. 2, pp. 561–571, Feb. 1977.
[96] V. G. Kapinos, Y. N. Osetsky, and P. A. Platonov, "Computer simulation of vacancy loops and stacking faults in zirconium," *J. Nucl. Mater.*, vol. 195, no. 1–2, pp. 83–101, Oct. 1992.
[97] N. de Diego, Y. N. Osetsky, and D. J. Bacon, "Structure and properties of vacancy and interstitial clusters in α-zirconium," *J. Nucl. Mater.*, vol. 374, no. 1–2, pp. 87–94, Feb. 2008.
[98] C. Dai, L. Balogh, Z. Yao, and M. R. Daymond, "The habit plane of ⟨a⟩ -type dislocation loops in α-zirconium: an atomistic study," *Philos. Mag.*, vol. 97, no. 12, pp. 944–956, Feb. 2017.
[99] V. Dubinko, A. Turkin, A. Abyzov, M. Griffiths, and S. Dean, "Modeling of the Simultaneous Evolution of Vacancy and Interstitial Dislocation Loops in hcp Metals Under Irradiation," *J. ASTM Int.*, vol. 3, no. 1, p. 12323, 2006.
[100] F. Christien and A. Barbu, "Effect of self-interstitial diffusion anisotropy in electron-irradiated zirconium: A cluster dynamics modeling," *J. Nucl. Mater.*, vol. 346, no. 2–3, pp. 272–281, Nov. 2005.
[101] C. Arévalo, M. J. Caturla, and J. M. Perlado, "Temperature dependence of damage accumulation in α-zirconium," *J. Nucl. Mater.*, vol. 367–370, pp. 338–343, Aug. 2007.
[102] R. A. Holt and R. W. Gilbert, "c-Component dislocations in neutron irradiated zircaloy-2," *J. Nucl. Mater.*, vol. 116, no. 1, pp. 127–130, May 1983.
[103] R. A. Holt and R. W. Gilbert, "c-Component dislocations in annealed Zircaloy irradiated at about 570 K," *J. Nucl. Mater.*, vol. 137, no. 3, pp. 185–189, Feb. 1986.
[104] R. A. Holt, "Mechanisms of irradiation growth of alpha-zirconium alloys," *J. Nucl. Mater.*, vol. 159, pp. 310–338, Oct. 1988.
[105] M. Griffiths and R. W. Gilbert, "The formation of c-component defects in zirconium alloys during neutron irradiation," *J. Nucl. Mater.*, vol. 150, no. 2, pp. 169–181, Oct. 1987.
[106] M. Griffiths, R. Gilbert, and V. Fidleris, "Accelerated Irradiation Growth of Zirconium Alloys," *Zircon. Nucl. Ind. Eighth Int. Symp.*, vol. ASTM STP 1023, pp. 658–677, 1989.
[107] L. Balogh, F. Long, Z. Yao, M. Preuss, and M. R. Daymond, "Quantifying Irradiation Defects in Zirconium Alloys: A Comparison between Transmission Electron Microscopy and Whole-Pattern Diffraction Line-Profile Analysis," *Zircon. Nucl. Ind. 18th Int. Symp.*, vol. ASTM STP 1597, pp. 691–724, Jan. 2018.
[108] J. Ribis *et al.*, "Experimental study and numerical modelling of the irradiation damage recovery in zirconium alloys," *J. Nucl. Mater.*, vol. 403, no. 1–3, pp. 135–146, 2010.
[109] M. Griffiths, D. Gilbon, C. Regnard, and C. Lemaignan, "HVEM study of the effects of alloying elements and impurities on radiation damage in Zr-alloys," *J. Nucl. Mater.*, vol. 205, pp. 273–283, Oct. 1993.
[110] D. Gilbon and C. Simonot, "Effect of Irradiation on the Microstructure of Zircaloy-4," *Zircon. Nucl. Ind. Tenth Int. Symp.*, vol. ASTM STP 1245, pp. 521–548, 1994.
[111] Y. de Carlan, C. Regnard, M. Griffiths, D. Gilbon, and C. Lemaignan, "Influence of Iron in the Nucleation of ⟨c⟩ Component Dislocation Loops in Irradiated Zircaloy-4," *Zircon. Nucl. Ind. Elev. Int. Symp.*, vol. ASTM STP 1295, pp. 638–653, 1996.

[112] M. Griffiths, R. A. Holt, and A. Rogerson, “Microstructural aspects of accelerated deformation of Zircaloy nuclear reactor components during service,” *J. Nucl. Mater.*, vol. 225, pp. 245–258, Aug. 1995.
[113] S. Doriot, D. Gilbon, J.-L. Béchade, M.-H. Mathon, L. Legras, and J.-P. Mardon, “Microstructural Stability of M5^{TM} Alloy Irradiated up to High Neutron Fluences,” *Zircon. Nucl. Ind. Fourteenth Int. Symp.*, vol. ASTM STP 1467, pp. 175-175–27, 2005.
[114] P. Bossis *et al.*, “In PWR Comprehensive Study of High Burn-Up Corrosion and Growth Behavior of M5® and Recrystallized Low-Tin Zircaloy-4,” *Zircon. Nucl. Ind. 15th Int. Symp.*, vol. ASTM STP 1505, pp. 430–456, 2009.
[115] G. Kobylyansky *et al.*, “Irradiation-induced growth and microstructure of recrystallized, cold worked and quenched zircaloy-2, NSF, and E635 alloys,” *J. ASTM Int.*, vol. 5, no. 4, pp. 1–19, 2008.
[116] G. Sundell, M. Thuvander, P. Tejland, M. Dahlbäck, L. Hallstadius, and H.-O. Andrén, “Redistribution of alloying elements in Zircaloy-2 after in-reactor exposure,” *J. Nucl. Mater.*, vol. 454, no. 1–3, pp. 178–185, Nov. 2014.
[117] V. N. Shishov, “The Evolution of Microstructure and Deformation Stability in Zr–Nb–(Sn,Fe) Alloys Under Neutron Irradiation,” *Zircon. Nucl. Ind. 16th Int. Symp.*, vol. ASTM STP 1529, pp. 37–66, 2011.
[118] S. Yagnik *et al.*, “Effect of Alloying Elements, Cold Work, and Hydrogen on the Irradiation-Induced Growth Behavior of Zirconium Alloy Variants,” *Zircon. Nucl. Ind. 18th Int. Symp.*, vol. ASTM STP 1597, pp. 748–795, Jan. 2018.
[119] L. Tournadre *et al.*, “Experimental study of the nucleation and growth of c-component loops under charged particle irradiations of recrystallized Zircaloy-4,” *J. Nucl. Mater.*, vol. 425, no. 1–3, pp. 76–82, Jun. 2012.
[120] L. Tournadre *et al.*, “Impact of Hydrogen Pick-Up and Applied Stress on C-Component Loops: Toward a Better Understanding of the Radiation Induced Growth of Recrystallized Zirconium Alloys,” *Zircon. Nucl. Ind. 17th Vol.*, vol. ASTM STP 1543, pp. 853–894, Jun. 2014.
[121] L. Tournadre *et al.*, “Toward a better understanding of the hydrogen impact on the radiation induced growth of zirconium alloys,” *J. Nucl. Mater.*, vol. 441, no. 1–3, pp. 222–231, Oct. 2013.
[122] N. Gharbi, F. Onimus, D. Gilbon, J.-P. Mardon, and X. Feaugas, “Impact of an applied stress on c-component loops under Zr ion irradiation in recrystallized Zircaloy-4 and M5 ®,” *J. Nucl. Mater.*, vol. 467, pp. 785–801, Dec. 2015.
[123] S. Yamada and T. Kameyama, “Observation of c-component dislocation structures formed in pure Zr and Zr-base alloy by self-ion accelerator irradiation,” *J. Nucl. Mater.*, vol. 422, no. 1–3, pp. 167–172, 2012.
[124] R. M. Hengstler-Eger *et al.*, “Heavy ion irradiation induced dislocation loops in AREVA’s M5® alloy,” *J. Nucl. Mater.*, vol. 423, no. 1–3, pp. 170–182, Apr. 2012.
[125] Y. Idrees *et al.*, “Effects of alloying elements on the formation of C-component loops in Zr alloy Excel under heavy ion irradiation,” *J. Mater. Res.*, vol. 30, no. 9, pp. 1310–1334, Apr. 2015.
[126] D. Hull and D. J. Bacon, *Introduction to dislocations*. Butterworth-Heinemann, 2001.
[127] B. Christiaen, C. Domain, L. Thuinet, A. Ambard, and A. Legris, “A new scenario for‹ c› vacancy loop formation in zirconium based on atomic-scale modeling,” *Acta Mater.*, vol. 179, pp. 93–106, 2019.

[128] C. Varvenne, O. Mackain, L. Proville, and E. Clouet, “Hydrogen and vacancy clustering in zirconium,” *Acta Mater.*, vol. 102, pp. 56–69, Jan. 2016.
[129] F. Christien and A. Barbu, “Cluster Dynamics modelling of irradiation growth of zirconium single crystals,” *J. Nucl. Mater.*, vol. 393, no. 1, pp. 153–161, Aug. 2009.
[130] S. I. Choi, G.-G. Lee, J. Kwon, and J. H. Kim, “Modeling of sink-induced irradiation growth of single-crystal and polycrystal zirconiums in nuclear reactors,” *J. Nucl. Mater.*, vol. 468, pp. 56–70, Jan. 2016.
[131] H. Rouchette, L. Thuinet, A. Legris, A. Ambard, and C. Domain, “Influence of shape anisotropy of self-interstitials on dislocation sink efficiencies in Zr: Multiscale modeling,” *Phys. Rev. B*, vol. 90, no. 1, Jul. 2014.
[132] C. Woo and E. Savino, “Stress-induced preferred absorption due to saddle-point anisotropy: The case of an infinitesimal dislocation loop,” *J. Nucl. Mater.*, vol. 116, no. 1, pp. 17–28, 1983.
[133] D. Carpentier, T. Jourdan, Y. Le Bouar, and M.-C. Marinica, “Effect of saddle point anisotropy of point defects on their absorption by dislocations and cavities,” *Acta Mater.*, vol. 136, pp. 323–334, Sep. 2017.
[134] M. Christensen *et al.*, “Understanding Irradiation Growth through Atomistic Simulations: Defect Diffusion and Clustering in α-Zirconium and the Influence of Alloying Elements,” *Zircon. Nucl. Ind. 18th Vol.*, vol. ASTM STP 1597, pp. 645–675, 2018.
[135] R. Adamson, “Effects of Neutron Irradiation on Microstructure and Properties of Zircaloy,” *Zircon. Nucl. Ind. Twelfth Int. Symp.*, vol. ASTM STP 1354, pp. 15–31, 2000.
[136] D. Faulkner and C. H. Woo, “Void swelling in zirconium,” *J. Nucl. Mater.*, vol. 90, no. 1–3, pp. 307–316, May 1980.
[137] J. H. Evans, A. J. E. Foreman, and R. J. McElroy, “Anisotropic diffusion of self-interstitials in zirconium,” *J. Nucl. Mater.*, vol. 168, no. 3, pp. 340–342, Dec. 1989.
[138] M. A. Tunes, R. W. Harrison, G. Greaves, J. A. Hinks, and S. E. Donnelly, “Effect of He implantation on the microstructure of zircaloy-4 studied using in situ TEM,” *J. Nucl. Mater.*, vol. 493, pp. 230–238, Sep. 2017.
[139] W. J. S. Yang, “Precipitate stability in neutron-irradiated Zircaloy-4,” *J. Nucl. Mater.*, vol. 158, pp. 71–80, Aug. 1988.
[140] A. Motta, F. Lefebvre, and C. Lemaignan, “Amorphization of Precipitates in Zircaloy under Neutron and Charged-Particle Irradiation,” *Zircon. Nucl. Ind. Ninth Int. Symp.*, vol. ASTM STP 1132, pp. 718–739, 1991.
[141] A. Harte *et al.*, “Nano-scale chemical evolution in a proton-and neutron-irradiated Zr alloy,” *J. Nucl. Mater.*, vol. 487, pp. 30–42, Apr. 2017.
[142] M. Griffiths, “Comments on precipitate stability in neutron-irradiated Zircaloy-4,” *J. Nucl. Mater.*, vol. 170, no. 3, pp. 294–300, Mar. 1990.
[143] A. Harte *et al.*, “Advances in synchrotron x-ray diffraction and transmission electron microscopy techniques for the investigation of microstructure evolution in proton- and neutron-irradiated zirconium alloys,” *J. Mater. Res.*, vol. 30, no. 9, pp. 1349–1365, Apr. 2015.
[144] M. Griffiths, R. W. Gilbert, and G. J. C. Carpenter, “Phase instability, decomposition and redistribution of intermetallic precipitates in Zircaloy-2 and -4 during neutron irradiation,” *J. Nucl. Mater.*, vol. 150, no. 1, pp. 53–66, Sep. 1987.

[145] R. W. Gilbert, M. Griffiths, and G. J. C. Carpenter, “Amorphous intermetallics in neutron irradiated zircaloys after high fluences,” *J. Nucl. Mater.*, vol. 135, no. 2–3, pp. 265–268, Oct. 1985.
[146] F. Garzarolli, W. Goll, A. Seibold, and I. Ray, “Effect of In-PWR Irradiation on Size, Structure, and Composition of Intermetallic Precipitates of Zr Alloys,” *Zircon. Nucl. Ind. Elev. Int. Symp.*, vol. ASTM STP 1295, pp. 541–556, 1996.
[147] A. T. Motta and C. Lemaignan, “A ballistic mixing model for the amorphization of precipitates in Zircaloy under neutron irradiation,” *J. Nucl. Mater.*, vol. 195, no. 3, pp. 277–285, Nov. 1992.
[148] C. Rodriguez, D. A. Barbiric, M. E. Pepe, J. A. Kovacs, J. A. Alonso, and R. Hojvat de Tendler, “Metastable phase stability in the ternary Zr–Fe–Cr system,” *Intermetallics*, vol. 10, no. 2, pp. 205–216, Feb. 2002.
[149] H. H. Shen, S. M. Peng, X. Xiang, F. N. Naab, K. Sun, and X. T. Zu, “Proton irradiation effects on the precipitate in a Zr–1.6Sn–0.6Nb–0.2Fe–0.1Cr alloy,” *J. Nucl. Mater.*, vol. 452, no. 1–3, pp. 335–342, Sep. 2014.
[150] D. Gilbon, A. Soniak, S. Doriot, and J.-P. Mardon, “Irradiation Creep and Growth Behavior, and Microstructural Evolution of Advanced Zr-Base Alloys,” *Zircon. Nucl. Ind. Twelfth Int. Symp.*, vol. ASTM STP 1354, pp. 51–73, 2000.
[151] D. Pêcheur, F. Lefebvre, A. T. Motta, C. Lemaignan, and D. Charquet, “Effect of irradiation on the precipitate stability in Zr alloys,” *J. Nucl. Mater.*, vol. 205, pp. 445–451, Oct. 1993.
[152] A. T. Motta, “Amorphization of intermetallic compounds under irradiation — A review,” *J. Nucl. Mater.*, vol. 244, no. 3, pp. 227–250, Apr. 1997.
[153] B. V. Cockeram, P. D. Edmondson, K. J. Leonard, B. F. Kammenzind, and J. L. Hollenbeck, “Atom probe examinations of Zircaloy irradiated at nominally 358 °C,” *Nucl. Mater. Energy*, vol. 19, pp. 416–432, May 2019.
[154] A. Motta, J. Faldowski, L. Howe, and P. Okamoto, “In Situ Studies of Phase Transformations in Zirconium Alloys and Compounds Under Irradiation,” *Zircon. Nucl. Ind. Elev. Int. Symp.*, no. ASTM STP 1295, pp. 557-557–23, 1996.
[155] X. T. Zu *et al.*, “Effect of proton and Ne irradiation on the microstructure of Zircaloy 4,” *Philos. Mag.*, vol. 85, no. 4–7, pp. 649–659, Feb. 2005.
[156] S. Doriot, F. Onimus, D. Gilbon, J.-P. Mardon, and F. Bourlier, “Transmission electron microscopy study of second phase particles irradiated by 2 MeV protons at 350 °C in Zr alloys,” *J. Nucl. Mater.*, vol. 494, pp. 398–410, Oct. 2017.
[157] A. Harte, M. Griffiths, and M. Preuss, “The characterisation of second phases in the Zr-Nb and Zr-Nb-Sn-Fe alloys: A critical review,” *J. Nucl. Mater.*, vol. 505, pp. 227–239, Jul. 2018.
[158] F. Lefebvre and C. Lemaignan, “Heavy ion-induced amorphlsation of Zr(Fe, Cr)2 precipitates in Zircaloy-4,” *J. Nucl. Mater.*, vol. 165, no. 2, pp. 122–127, May 1989.
[159] A. T. Motta, L. Howe, and P. Okamoto, “Amorphization kinetics of Zr3Fe under electron irradiation,” *J. Nucl. Mater.*, vol. 205, pp. 258–266, 1993.
[160] L. M. Howe, D. Phillips, A. T. Motta, and P. R. Okamoto, “Irradiation-induced phase transformations in zirconium alloys,” *Surf. Coat. Technol.*, vol. 66, no. 1–3, pp. 411–418, Aug. 1994.

[161] A. T. Motta and C. Lemaignan, “A ballistic mixing model for the amorphization of precipitates in Zircaloy under neutron irradiation,” *J. Nucl. Mater.*, vol. 195, no. 3, pp. 277–285, Nov. 1992.
[162] E. M. Francis *et al.*, “Iron redistribution in a zirconium alloy after neutron and proton irradiation studied by energy-dispersive X-ray spectroscopy (EDX) using an aberration-corrected (scanning) transmission electron microscope,” *J. Nucl. Mater.*, vol. 454, no. 1–3, pp. 387–397, Nov. 2014.
[163] V. N. Shishov *et al.*, “Structure-Phase State, Corrosion and Irradiation Properties of Zr-Nb-Fe-Sn System Alloys,” *Zircon. Nucl. Ind. 15th Int. Symp.*, vol. ASTM STP 1505, pp. 724–743, 2008.
[164] A. Nikulina, V. Shishov, M. Peregud, A. Tselischev, V. Shamardin, and G. Kobylyansky, “Irradiation Induced Growth and Microstructure Evolution of Zr-1.2Sn-1Nb-0.4Fe Under Neutron Irradiation to High Doses,” *Eff. Radiat. Mater. 18th Int. Symp.*, pp. 1045–1061, 1999.
[165] S. Averin, V. Panchenko, A. Kozlov, L. Sinelnikov, V. Shishov, and A. Nikulina, “Evolution of Dislocation and Precipitate Structure in Zr Alloys Under Long-Term Irradiation,” *Zircon. Nucl. Ind. Twelfth Int. Symp.*, vol. ASTM STP 1354, pp. 105–122, 2000.
[166] V. Markelov *et al.*, “Preliminary Irradiation Effect on Corrosion Resistance of Zirconium Alloys,” *Zircon. Nucl. Ind. 18th Int. Symp.*, vol. ASTM STP 1597, pp. 857–880, Jan. 2018.
[167] G. Sabol, R. Comstock, R. Weiner, P. Larouere, and R. Stanutz, “In-Reactor Corrosion Performance of ZIRLO™ and Zircaloy-4,” *Zircon. Nucl. Ind. Tenth Int. Symp.*, pp. 724–744, ASTM STP 1245.
[168] W. G. Burgers, “On the process of transition of the cubic-body-centered modification into the hexagonal-close-packed modification of zirconium,” *Physica*, vol. 1, no. 7–12, pp. 561–586, May 1934.
[169] V. Shishov *et al.*, “Influence of Neutron Irradiation on Dislocation Structure and Phase Composition of Zr-Base Alloys,” *Zircon. Nucl. Ind. 11th Int. Symp.*, vol. ASTM STP 1295, pp. 603–622, 1996.
[170] C. Toffolon *et al.*, “Experimental Study and Preliminary Thermodynamic Calculations of the Pseudo-Ternary Zr-Nb-Fe-(O,Sn) System,” *Zircon. Nucl. Ind. Thirteen. Int. Symp.*, vol. ASTM STP 1423, pp. 361–383, 2002.
[171] R. A. Perez, H. Nakajima, and F. Dyment, “Diffusion in α-Ti and Zr,” *Mater. Trans.*, vol. 44, no. 1, pp. 2–13, 2003.
[172] V. Chabretou *et al.*, “Ultra Low Tin Quaternary Alloys PWR Performance—Impact of Tin Content on Corrosion Resistance, Irradiation Growth, and Mechanical Properties,” *Zircon. Nucl. Ind. 16th Int. Symp.*, vol. ASTM STP 1529, pp. 801–826, Jun. 2011.
[173] E. Francis *et al.*, “Effect of Nb and Fe on damage evolution in a Zr-alloy during proton and neutron irradiation,” *Acta Mater.*, vol. 165, pp. 603–614, Feb. 2019.
[174] V. V. Novikov *et al.*, “Investigation of the Microstructure of Zirconium Alloys Irradiated by Zirconium Ions in an Accelerator,” *At. Energy*, vol. 115, no. 5, pp. 307–312, Feb. 2014.
[175] Y. Matsukawa *et al.*, “The effect of crystallographic mismatch on the obstacle strength of second phase precipitate particles in dispersion strengthening: bcc Nb particles and nanometric Nb clusters embedded in hcp Zr,” *Acta Mater.*, vol. 102, pp. 323–332, Jan. 2016.
[176] J. Parker, V. Perovic, M. Leger, and R. Fleck, “Microstructural Effects on the Irradiation Growth of Zr-2.5Nb,” *Zircon. Nucl. Ind. 7th Int. Symp.*, pp. 86-86–15, 1987.

[177] Z. Yu *et al.*, "Microstructure and microchemistry study of irradiation-induced precipitates in proton irradiated ZrNb alloys," *Acta Mater.*, vol. 178, pp. 228–240, 2019.
[178] G. He *et al.*, "Investigating the stability of second phase particles in Zr-Nb alloys under irradiation," *J. Nucl. Mater.*, vol. 526, p. 151738, Dec. 2019.
[179] C. Toffolon-Masclet, P. Barberis, J.-C. Brachet, J.-P. Mardon, and L. Legras, "Study of Nb and Fe Precipitation in α-Phase Temperature Range (400 to 550°C) in Zr-Nb-(Fe-Sn) Alloys," *J. ASTM Int.*, vol. 2, no. 5, p. 12321, 2005.
[180] V. Perovic *et al.*, "Microstructural and microchemical studies of Zr-2.5Nb pressure tube alloy," *J. Nucl. Mater.*, vol. 205, pp. 251–257, Oct. 1993.
[181] C. Coleman, R. Gilbert, G. Carpenter, and G. Weatherly, "Precipitation in Zr--2. 5 Wt.-% Nb During Neutron Irradiation," *Phase Stab. Irradiat.*, pp. 587–599, 1980.
[182] G. Brebec, "Diffusion and Precipitation Under Irradiation," *Diffus. Mater.*, pp. 339–356, 1990.
[183] A. Sarce, "Stability of precipitates in the anisotropic α-Zr matrix under irradiation," *J. Nucl. Mater.*, vol. 185, no. 2, pp. 214–223, Nov. 1991.
[184] A. A. Turkin, A. V. Buts, and A. S. Bakai, "Construction of radiation-modified phase diagrams under cascade-producing irradiation: application to Zr–Nb alloy," *J. Nucl. Mater.*, vol. 305, no. 2–3, pp. 134–152, Oct. 2002.
[185] B. A. Gurovich, A. S. Frolov, E. A. Kuleshova, D. A. Maltsev, D. V. Safonov, and E. V. Alekseeva, "TEM-studies of the dislocation loops and niobium-based precipitates in E110 alloy after operation in VVER-type reactor conditions," *Mater. Charact.*, vol. 150, pp. 22–30, Apr. 2019.
[186] J. Ribis, S. Doriot, and F. Onimus, "Shape, orientation relationships and interface structure of beta-Nb nano-particles in neutron irradiated zirconium alloy," *J. Nucl. Mater.*, vol. 511, pp. 18–29, 2018.
[187] O. T. Woo, R. M. Hutcheon, and C. E. Coleman, "Precipitation in Zr-2.5Nb During 10 MeV Electron Irradiation," *MRS Proc.*, vol. 373, 1994.
[188] C. D. Cann, C. B. So, R. C. Styles, and C. E. Coleman, "Precipitation in Zr-2.5Nb enhanced by proton irradiation," *J. Nucl. Mater.*, vol. 205, pp. 267–272, Oct. 1993.
[189] W. C. Burgers, "On the process of transition of the cubic-body-centered modification into the hexagonal-close-packed modification of zirconium," *Physica 1*, pp. 561–586.
[190] G. Ayrault, "Radiation-induced precipitation in single- and dual-ion irradiated Ti-6AI-4V," *J. Nucl. Mater.*, vol. 113, no. 1, pp. 1–13, Jan. 1983.
[191] S. Doriot *et al.*, "Evolution of defects in Ti6-4 under Ti2+ ion irradiation: Focus on radiation-induced precipitates," *J. Nucl. Mater.*, vol. 511, pp. 264–276, Dec. 2018.
[192] D. L. Plumton, G. L. Kulcinski, and R. A. Dodd, "Radiation induced precipitation in 9 MeV Al ion irradiated Ti-6A1-4V," *J. Nucl. Mater.*, vol. 144, no. 3, pp. 264–274, Feb. 1987.
[193] S. Tähtinen, P. Moilanen, B. N. Singh, and D. J. Edwards, "Tensile and fracture toughness properties of unirradiated and neutron irradiated titanium alloys," *J. Nucl. Mater.*, vol. 307–311, pp. 416–420, Dec. 2002.
[194] P. Wilkes and G. L. Kulcinski, "Heavy ion irradiation of a Ti-6Al-4V alloy," *J. Nucl. Mater.*, vol. 78, no. 2, pp. 427–430, Dec. 1978.
[195] L. M. Howe and W. R. Thomas, "The effect of neutron irradiation on the tensile properties of zircaloy-2," *J. Nucl. Mater.*, vol. 2, no. 3, pp. 248–260, Sep. 1960.

[196] D. Hardy, “The Effect of Neutron Irradiation on the Mechanical Properties of Zirconium Alloy Fuel Cladding in Uniaxial and Biaxial Tests,” *Irradiat. Eff. Struct. Alloys Nucl. React. Appl.*, vol. ASTM STP 484, pp. 215–257, 1970.
[197] H. R. Higgy and F. H. Hammad, “Effect of neutron irradiation on the tensile properties of zircaloy-2 and zircaloy-4,” *J. Nucl. Mater.*, vol. 44, no. 2, pp. 215–227, Aug. 1972.
[198] G. Rieger and D. Lee, “Strength and Ductility of Neutron Irradiated and Textured Zircaloy-2,” *Zircon. Nucl. Appl.*, vol. ASTM STP 551, pp. 355–369, 1974.
[199] C. Baroch, “Effect of Irradiation at 130, 650, and 775°F on Tensile Properties of Zircaloy-4 at 70, 650, and 775°F,” *Eff. Radiat. Struct. Mater.*, vol. ASTM STP 570, pp. 129–142, 1975.
[200] K. Pettersson, G. Vesterlund, and T. Andersson, “Effect of Irradiation on the Strength, Ductility, and Defect Sensitivity of Fully Recrystallized Zircaloy Tube,” *Zircon. Nucl. Ind.*, vol. ASTM STP 681, pp. 155–173, 1979.
[201] T. Onchi, H. Kayano, and Y. Higashiguchi, “The inhomogeneous deformation behaviour of neutron irradiated Zircaloy-2,” *J. Nucl. Mater.*, vol. 88, no. 2–3, pp. 226–235, Feb. 1980.
[202] T. Yasuda, M. Nakatsuka, and K. Yamashita, “Deformation and Fracture Properties of Neutron-Irradiated Recrystallized Zircaloy-2 Cladding under Uniaxial Tension,” *Zircon. Nucl. Ind.*, pp. 734-734–14, 1985.
[203] P. Morize, J. Baicry, and J. Mardon, “Effect of Irradiation at 588 K on Mechanical Properties and Deformation Behavior of Zirconium Alloy Strip,” *Zircon. Nucl. Ind.*, vol. ASTM STP 939, pp. 101–119, 1987.
[204] T. . Byun and K. Farrell, “Irradiation hardening behavior of polycrystalline metals after low temperature irradiation,” *J. Nucl. Mater.*, vol. 326, no. 2–3, pp. 86–96, Mar. 2004.
[205] B. Cheadle, C. Ellis, and J. van der Kuur, “Plastic Instability in Irradiated Zr-Sn and Zr-Nb Alloys,” *Zircon. Nucl. Appl.*, pp. 370-370–15, 1974.
[206] K. Farrell, T. S. Byun, and N. Hashimoto, “Deformation mode maps for tensile deformation of neutron-irradiated structural alloys,” *J. Nucl. Mater.*, vol. 335, no. 3, pp. 471–486, Dec. 2004.
[207] F. Onimus, J. L. Béchade, C. Duguay, D. Gilbon, and P. Pilvin, “Investigation of neutron radiation effects on the mechanical behavior of recrystallized zirconium alloys,” *J. Nucl. Mater.*, vol. 358, no. 2–3, pp. 176–189, Nov. 2006.
[208] R. S. Daum, S. Majumdar, and M. C. Billone, “Experimental and Analytical Investigation of the Mechanical Behavior of High-Burnup Zircaloy-4 Fuel Cladding,” *Zircon. Nucl. Ind. 15th Int. Symp.*, pp. 119-119–22, 2009.
[209] X. Wei, J. R. Theaker, and M. Griffiths, “Deformation Anisotropy of Annealed Zircaloy-2 as a Function of Fast Neutron Fluence,” *Zircon. Nucl. Ind. 15th Int. Symp.*, pp. 583-583–11, 2007.
[210] B. Bourdiliau *et al.*, “Impact of Irradiation Damage Recovery During Transportation on the Subsequent Room Temperature Tensile Behavior of Irradiated Zirconium Alloys,” *Zircon. Nucl. Ind. 16th Int. Symp.*, pp. 929–953, Sep. 2010.
[211] B. V. Cockeram, K. J. Leonard, T. S. Byun, L. L. Snead, and J. L. Hollenbeck, “Development of microstructure and irradiation hardening of Zircaloy during low dose neutron irradiation at nominally 377–440°C,” *J. Nucl. Mater.*, vol. 449, no. 1–3, pp. 69–87, Jun. 2014.

[212] C. Lemaignan and A. T. Motta, “Zirconium Alloys in Nuclear Applications,” in *Materials Science and Technology Series*, vol. 10B, Wiley-VCH Verlag GmbH & Co. KGaA, 2006.
[213] R. Adamson and W. Bell, “Effects of neutron irradiation and oxygen content on the microstructure and mechanical properties of Zircaloy,” in *Microstructure and Mechanical Behaviour of Materials.*, Xian, China, 1985, vol. 1, pp. 237–246.
[214] T. Torimaru, T. Yasuda, and M. Nakatsuka, “Changes in mechanical properties of irradiated Zircaloy-2 fuel cladding due to short term annealing,” *J. Nucl. Mater.*, vol. 238, no. 2–3, pp. 169–174, Nov. 1996.
[215] M. NAKATSUKA and M. NAGAI, “Reduction of plastic anisotropy of zircaloy cladding by neutron irradiation. (I). Yield loci obtained from knoop hardness.,” *J. Nucl. Sci. Technol.*, vol. 24, no. 10, pp. 832–838, 1987.
[216] J. Ribis *et al.*, “Experimental and Modeling Approach of Irradiation Defects Recovery in Zirconium Alloys: Impact of an Applied Stress,” *J. ASTM Int.*, vol. 5, no. 3, p. 101118, 2008.
[217] R. O. Oviasuyi and R. J. Klassen, “Anisotropic deformation of Zr ion irradiated Zr–2.5%Nb micro-pillars at 25°C,” *J. Nucl. Mater.*, vol. 421, no. 1–3, pp. 54–57, Feb. 2012.
[218] Q. Wang, C. Cochrane, F. Long, H. Yu, and M. R. Daymond, “Micropillar compression study on heavy ion irradiated Zr-2.5Nb pressure tube alloy,” *J. Nucl. Mater.*, vol. 511, pp. 487–495, Dec. 2018.
[219] H. L. Yang *et al.*, “Surface orientation dependence of irradiation-induced hardening in a polycrystalline zirconium alloy,” *Scr. Mater.*, vol. 162, pp. 209–213, Mar. 2019.
[220] Q. Wang, F. Long, Z. Wang, N. Guo, and M. R. Daymond, “Orientation dependent evolution of plasticity of irradiated Zr-2.5Nb pressure tube alloy studied by nanoindentation and finite element modeling,” *J. Nucl. Mater.*, vol. 512, pp. 371–384, Dec. 2018.
[221] Q. Wang, C. Cochrane, T. Skippon, Z. Wang, H. Abdolvand, and M. R. Daymond, “Orientation-dependent irradiation hardening in pure Zr studied by nanoindentation, electron microscopies, and crystal plasticity finite element modeling,” *Int. J. Plast.*, Aug. 2019.
[222] F. Kroupa and P. B. Hirsch, “Elastic interaction between prismatic dislocation loops and straight dislocations,” *Discuss. Faraday Soc.*, vol. 38, p. 49, 1964.
[223] M. J. Makin, “The long-range forces between dislocation loops and dislocations,” *Philos. Mag. J. Theor. Exp. Appl. Phys.*, vol. 10, no. 106, pp. 695–711, Oct. 1964.
[224] G. Saada and J. Washburn, “INTERACTION BETWEEN PRISMATIC AND GLISSILE DISLOCATIONS,” Office of Scientific and Technical Information (OSTI), Aug. 1962.
[225] A. J. E. Foreman and J. V. Sharp, “A mechanism for the sweeping-up of loops by glide dislocations during deformation,” *Philos. Mag.*, vol. 19, no. 161, pp. 931–937, May 1969.
[226] P. Hirsch, “Point defect cluster hardening,” presented at the Vacancies’ 76. Proceedings of a conference on’point defect behaviour and diffusional processes’, The Royal Fort, University of Bristol, 1977.
[227] G. J. C. Carpenter, “Dislocation channeling by prism slip in HCP metals,” *Scr. Metall.*, vol. 10, no. 5, pp. 411–413, May 1976.
[228] M. Fregonese, C. Régnard, L. Rouillon, T. Magnin, F. Lefebvre, and C. Lemaignan, “Failure Mechanisms of Irradiated Zr Alloys Related to PCI: Activated Slip Systems, Localized Strains, and Iodine-Induced Stress Corrosion Cracking,” *Zircon. Nucl. Ind. Twelfth Int. Symp.*, vol. ASTM STP 1354, pp. 377–398, 2000.

[229] F. Onimus, I. Monnet, J. . Béchade, C. Prioul, and P. Pilvin, “A statistical TEM investigation of dislocation channeling mechanism in neutron irradiated zirconium alloys,” *J. Nucl. Mater.*, vol. 328, no. 2–3, pp. 165–179, Jul. 2004.
[230] R. E. Voskoboynikov, Y. N. Osetsky, and D. J. Bacon, “Self-interstitial atom clusters as obstacles to glide of edge dislocations in α-zirconium,” *Mater. Sci. Eng. A*, vol. 400–401, pp. 54–58, Jul. 2005.
[231] A. Serra and D. J. Bacon, “Atomic-level computer simulation of the interaction between $\frac{1}{3}\langle 1\,1\,\bar{2}\,0 \rangle\{1\,\bar{1}\,0\,0\}$ dislocations and $\frac{1}{3}\langle 1\,1\,\bar{2}\,0 \rangle$ interstitial loops inα-zirconium,” *Model. Simul. Mater. Sci. Eng.*, vol. 21, no. 4, p. 45007, Apr. 2013.
[232] K. Ghavam and R. Gracie, “Simulations of reactions between irradiation induced ⟨a⟩ -loops and mixed dislocation lines in zirconium,” *J. Nucl. Mater.*, vol. 462, pp. 126–134, Jul. 2015.
[233] T. Nogaret, C. Robertson, and D. Rodney, “Atomic-scale plasticity in the presence of Frank loops,” *Philos. Mag.*, vol. 87, no. 6, pp. 945–966, Feb. 2007.
[234] J. Drouet, L. Dupuy, F. Onimus, F. Mompiou, S. Perusin, and A. Ambard, “Dislocation dynamics simulations of interactions between gliding dislocations and radiation induced prismatic loops in zirconium,” *J. Nucl. Mater.*, vol. 449, no. 1–3, pp. 252–262, Jun. 2014.
[235] J. Drouet, L. Dupuy, F. Onimus, and F. Mompiou, “A direct comparison between in-situ transmission electron microscopy observations and Dislocation Dynamics simulations of interaction between dislocation and irradiation induced loop in a zirconium alloy,” *Scr. Mater.*, vol. 119, pp. 71–75, Jul. 2016.
[236] M. J. Makin and J. V. Sharp, “A Model of ‘Lattice’ Hardening in Irradiated Copper Crystals with the External Characteristics of ‘Source’ Hardening,” *Phys. Status Solidi B*, vol. 9, no. 1, pp. 109–118, 1965.
[237] M. J. Makin and F. J. Minter, “Irradiation hardening in copper and nickel,” *Acta Metall.*, vol. 8, no. 10, pp. 691–699, Oct. 1960.
[238] K. H. Westmacott, “Hardening in quenched aluminium,” *Philos. Mag.*, vol. 14, no. 128, pp. 239–254, Aug. 1966.
[239] A. J. E. Foreman and M. J. Makin, “Dislocation movement through random arrays of obstacles,” *Philos. Mag.*, vol. 14, no. 131, pp. 911–924, Oct. 1966.
[240] L. Brown and R. Ham, *Dislocation-Particle Interactions in: Strengthening Methods in Crystals*, Applied Science Publishers Ltd. Barking, Essex, England: A. Kelly, R.B. Nicholson, 1971.
[241] T. ONCHI, H. KAYANO, and Y. HIGASHIGUCHI, “Effect of Neutron Irradiation on Deformation Behavior of Zirconium,” *J. Nucl. Sci. Technol.*, vol. 14, no. 5, pp. 359–369, 1977.
[242] A. Garde, “Effects of Irradiation and Hydriding on the Mechanical Properties of Zircaloy-4 at High Fluence,” *Zircon. Nucl. Ind. Eighth Int. Symp.*, vol. ASTM STP 1023, pp. 548–569, 1989.
[243] C. Williams, R. Adamson, and K. Olshausen, “Effects of boiling water reactor irradiation on tensile properties of Zircaloy,” in *European Conference on Irradiation Behaviour of Fuel Cladding and Core Component Materials*, Karlsruhe, Germany, 1974.
[244] R. Adamson, S. Wisner, R. Tucker, and R. Rand, “Failure Strain for Irradiated Zircaloy Based on Subsized Specimen Testing and Analysis,” *Use Small-Scale Specim. Test. Irradiat. Mater.*, vol. ASTM STP 888, pp. 171–184, 1986.

[245] C. Regnard, B. Verhaeghe, F. Lefebvre-Joud, and C. Lemaignan, “Activated Slip Systems and Localized Straining of Irradiated Zr Alloys in Circumferential Loadings,” *Zircon. Nucl. Ind. Thirteen. Int. Symp.*, vol. ASTM STP 1423, pp. 384–399, 2002.
[246] C. E. Coleman, D. Mills, and J. van der Kuur, “Deformation parameters of neutron irradiated Zircaloy-4 at 300°C,” *Can. Metall. Q.*, vol. 11, no. 1, pp. 91–100, Jan. 1972.
[247] D. Tomalin, “Localized Ductility of Irradiated Zircaloy-2 Cladding in Air and Iodine Environments,” *Zircon. Nucl. Ind.*, vol. ASTM STP 633, pp. 557–572, 1977.
[248] H. S. Rosenbaum, G. F. Rieger, and D. Lee, “Localized Deformation and Fracture in Neutron Irradiated Zircaloy-2,” *Metall. Trans.*, vol. 5, no. 8, pp. 1867–1874, Aug. 1974.
[249] T. S. Byun and K. Farrell, “Plastic instability in polycrystalline metals after low temperature irradiation,” *Acta Mater.*, vol. 52, no. 6, pp. 1597–1608, Apr. 2004.
[250] C. Chow, C. Coleman, R. Hosbons, P. Davies, M. Griffiths, and R. Choubey, “Fracture Toughness of Irradiated Zr-2.5Nb Pressure Tubes from CANDU Reactors,” *Zircon. Nucl. Ind. Ninth Int. Symp.*, pp. 246-246–30, 1991.
[251] D. K. Rodgers *et al.*, “In-reactor performance of pressure tubes in CANDU reactors,” *J. Nucl. Mater.*, vol. 383, no. 1–2, pp. 22–27, Dec. 2008.
[252] P. Delobelle, P. Robinet, P. Geyer, and P. Bouffioux, “A model to describe the anisotropic viscoplastic behaviour of Zircaloy-4 tubes,” *J. Nucl. Mater.*, vol. 238, no. 2–3, pp. 135–162, Nov. 1996.
[253] W. J. O’Donnell and B. F. Langer, “Fatigue Design Basis for Zircaloy Components,” *Nucl. Sci. Eng.*, vol. 20, no. 1, pp. 1–12, Sep. 1964.
[254] K. Pettersson, “Low-cycle fatigue properties of Zircaloy-2 cladding,” *J. Nucl. Mater.*, vol. 56, no. 1, pp. 91–102, Apr. 1975.
[255] M. Nakatsuka, T. Kubo, and Y. Hayashi, “Fatigue Behavior of Neutron Irradiated Zircaloy-2 Fuel Cladding Tubes,” *Zircon. Nucl. Ind. Ninth Int. Symp.*, pp. 230-230–16, 1991.
[256] A. Soniak, S. Lansiart, J. Royer, J.-P. Mardon, and N. Waeckel, “Irradiation Effect on Fatigue Behavior of Zircaloy-4 Cladding Tubes,” *Zircon. Nucl. Ind. Tenth Int. Symp.*, pp. 549-549–10, 1994.
[257] S. Wisner, M. Reynolds, and R. Adamson, “Fatigue Behavior of Irradiated and Unirradiated Zircaloy and Zirconium,” *Zircon. Nucl. Ind. Tenth Int. Symp.*, pp. 499-499–22, 1994.
[258] K. Petterson, “Evidence for basal or near-basal slip in irradiated Zircaloy,” *J. Nucl. Mater.*, vol. 105, pp. 341–344, 1982.
[259] F. Onimus *et al.*, “Plastic Deformation of Irradiated Zirconium Alloys: TEM Investigations and Micro-Mechanical Modeling,” *J. ASTM Int.*, vol. 2, no. 8, p. 12424, 2005.
[260] F. Onimus, J. L. Béchade, and D. Gilbon, “Experimental Analysis of Slip Systems Activation in Neutron-Irradiated Zirconium Alloys and Comparison with Polycrystalline Model Simulations,” *Metall. Mater. Trans. A*, vol. 44, no. S1, pp. 45–60, Oct. 2012.
[261] M. Wechsler, “The Inhomogeneity of Plastic Deformation,” *Am. Soc. Met.*, 1973.
[262] A. Luft, “Microstructural processes of plastic instabilities in strengthened metals,” *Prog. Mater. Sci.*, vol. 35, no. 2, pp. 97–204, Jan. 1991.
[263] J. V. Sharp, “Deformation of neutron-irradiated copper single crystals,” *Philos. Mag.*, vol. 16, no. 139, pp. 77–96, Jul. 1967.
[264] J. V. Sharp, “Correlation between cleared channels and surface slip steps in neutron irradiated copper crystals,” *Radiat. Eff.*, vol. 14, no. 1–2, pp. 71–75, May 1972.

[265] M. J. Makin, “The mechanism of slip band growth in irradiated crystals,” *Philos. Mag.*, vol. 21, no. 172, pp. 815–817, Apr. 1970.
[266] T. Nogaret, D. Rodney, M. Fivel, and C. Robertson, “Clear band formation simulated by dislocation dynamics: Role of helical turns and pile-ups,” *J. Nucl. Mater.*, vol. 380, no. 1–3, pp. 22–29, Oct. 2008.
[267] R. Thomas *et al.*, “Characterisation of irradiation enhanced strain localisation in a zirconium alloy,” *Materialia*, vol. 5, p. 100248, Mar. 2019.
[268] D. Lee and R. Adamson, “Modeling of Localized Deformation in Neutron Irradiated Zircaloy-2,” *Zircon. Nucl. Ind.*, vol. ASTM STP 633, pp. 385–401, 1977.
[269] D. G. Franklin, G. E. Lucas, and A. L. Bement, *Creep of zirconium alloys in nuclear reactors*, vol. ASTM STP 815. ASTM International, 1983.
[270] F. Onimus and J.-L. Béchade, “A polycrystalline modeling of the mechanical behavior of neutron irradiated zirconium alloys,” *J. Nucl. Mater.*, vol. 384, no. 2, pp. 163–174, Feb. 2009.
[271] T. O. Erinosho and F. P. E. Dunne, “Strain localization and failure in irradiated zircaloy with crystal plasticity,” *Int. J. Plast.*, vol. 71, pp. 170–194, Aug. 2015.
[272] C. Coleman, P. Chow, C. Ells, M. Griffiths, E. Ibrahim, and S. Sagat, “Rejuvenation of Fracture Properties of Irradiated Zr-2.5 Nb by Heat Treatment,” *Eff. Radiat. Mater. 15th Int. Symp.*, vol. ASTM STP 1125, pp. 318–336, 1992.
[273] B. V. Cockeram, K. J. Leonard, T. S. Byun, L. L. Snead, and J. L. Hollenbeck, “The recovery of irradiation damage for Zircaloy-2 and Zircaloy-4 following low dose neutron irradiation at nominally 358 °C,” *J. Nucl. Mater.*, vol. 461, pp. 244–264, Jun. 2015.
[274] C. C. Dollins, “Post irradiation recovery of irradiation damage,” *Radiat. Eff.*, vol. 16, no. 3–4, pp. 271–280, Oct. 1972.
[275] K. U. Snowden and K. Veevers, “Radiation hardening in Zircaloy-2,” *Radiat. Eff.*, vol. 20, no. 3, pp. 169–174, Jan. 1973.
[276] G. Carpenter and J. Watters, “Irradiation Damage Recovery in Some Zirconium Alloys,” *Zircon. Nucl. Appl.*, vol. ASTM STP 551, pp. 400–415, 1974.
[277] K. Ito, K. Kamimura, and Y. Tsukuda, “Evaluation of irradiation effect on spent fuel cladding creep properties,” presented at the Proc. 2004 International Meeting on LWR Fuel Performance, Orlando, 2004.
[278] K. Veevers and W. B. Rotsey, “Effect of irradiation on strain ageing in annealed zircaloy-2,” *J. Nucl. Mater.*, vol. 27, no. 1, pp. 108–111, Jul. 1968.
[279] C. Williams and R. Gilbert, “Radiation Damage in reactor materials,” in *Proceedings of a Symposium, Vienna, June 2-6, 1969*, 1969, vol. Vol. I, p. 235.
[280] D. O. Northwood and A. R. Causey, “Microstructural changes during thermally induced strain recovery in irradiated zircaloy-4 stress relaxation specimens,” *J. Nucl. Mater.*, vol. 64, no. 3, pp. 308–312, Feb. 1977.
[281] M. Topping *et al.*, “Investigating the thermal stability of irradiation-induced damage in a zirconium alloy with novel in situ techniques,” *Acta Mater.*, vol. 145, pp. 255–263, Feb. 2018.
[282] B. L. Eyre and D. M. Maher, “Neutron irradiation damage in molybdenum,” *Philos. Mag.*, vol. 24, no. 190, pp. 767–797, Oct. 1971.
[283] J. P. Hirth and J. Lothe, *Theory of Dislocations (2nd ed.)*, vol. 50. 1983.
[284] B. Burton and M. V. Speight, “The coarsening and annihilation kinetics of dislocation loop,” *Philos. Mag. A*, vol. 53, no. 3, pp. 385–402, Mar. 1986.

[285] P. B. Hirsch, J. Silcox, R. E. Smallman, and K. H. Westmacott, “Dislocation loops in quenched aluminium,” *Philos. Mag.*, vol. 3, no. 32, pp. 897–908, Aug. 1958.
[286] C. A. Johnson, “The growth of prismatic dislocation loops during annealing,” *Philos. Mag.*, vol. 5, no. 60, pp. 1255–1265, Dec. 1960.
[287] M. Peehs and J. Fleisch, “LWR Spent Fuel Storage Behaviour,” *J. Nucl. Mater.*, vol. 137, no. 3, pp. 190–202, Feb. 1986.
[288] V. Fidleris, “The irradiation creep and growth phenomena,” *J. Nucl. Mater.*, vol. 159, pp. 22–42, Oct. 1988.
[289] M. Mayuzumi and K. Murai, “Post irradiation creep and rupture of irradiated PWR fuel cladding,” presented at the International conference on nuclear waste management and environmental remediation., 1993.
[290] I. Schaffler, P. Geyer, P. Bouffioux, and P. Delobelle, “Thermomechanical Behavior and Modeling Between 350°C and 400°C of Zircaloy-4 Cladding Tubes From an Unirradiated State to High Fluence (0 to 85s˙1024nm−2,E>1MeV),” *J. Eng. Mater. Technol.*, vol. 122, no. 2, pp. 168–176, Jul. 1999.
[291] A. Soniak, N. L’Hullier, J.-P. Mardon, V. Rebeyrolle, P. Bouffioux, and C. Bernaudat, “Irradiation Creep Behavior of Zr-Base Alloys,” *Zircon. Nucl. Ind. Thirteen. Int. Symp.*, vol. ASTM STP 1423, pp. 837–862, 2002.
[292] C. Cappelaere *et al.*, “Impact of Irradiation Defects Annealing on Long-Term Thermal Creep of Irradiated Zircaloy-4 Cladding Tube,” *Zircon. Nucl. Ind. Thirteen. Int. Symp.*, vol. ASTM STP 1423, pp. 720–739, 2002.
[293] R. Limon and S. Lehmann, “A creep rupture criterion for Zircaloy-4 fuel cladding under internal pressure,” *J. Nucl. Mater.*, vol. 335, no. 3, pp. 322–334, Dec. 2004.
[294] T. Yasuda, M. Nakatsuka, and M. Mayuzumi, “Creep characteristics of irradiated Zircaloy-2 cladding tubes under dry storage conditions,” *Trans. Am. Nucl. Soc.*, vol. 61, 1990.
[295] K. Murty and S. Mahmood, “Effects of Recrystallization and Neutron Irradiation on Creep Anisotropy of Zircaloy Cladding,” *Zircon. Nucl. Ind. Ninth Int. Symp.*, vol. ASTM STP 1132, pp. 198–217, 1991.
[296] H. Tsai, M. Billone, and S. Dean, “Thermal Creep of Irradiated Zircaloy Cladding,” *J. ASTM Int.*, vol. 3, no. 1, p. 12425, 2006.
[297] V. Fidleris, R. Tucker, and R. Adamson, “An Overview of Microstructural and Experimental Factors That Affect the Irradiation Growth Behavior of Zirconium Alloys,” *Zircon. Nucl. Ind.*, vol. ASTM STP 939, pp. 49–85, 1987.
[298] A. Rogerson, “Irradiation growth in zirconium and its alloys,” *J. Nucl. Mater.*, vol. 159, pp. 43–61, Oct. 1988.
[299] G. J. C. Carpenter, R. H. Zee, and A. Rogerson, “Irradiation growth of zirconium single crystals: A review,” *J. Nucl. Mater.*, vol. 159, pp. 86–100, Oct. 1988.
[300] R. A. Holt, “In-Reactor Deformation of Zirconium Alloy Components,” *J. ASTM Int.*, vol. 5, no. 6, p. 101354, 2008.
[301] R. A. Holt, “In-reactor deformation of cold-worked Zr–2.5Nb pressure tubes,” *J. Nucl. Mater.*, vol. 372, no. 2–3, pp. 182–214, Jan. 2008.
[302] G. J. C. Carpenter, R. A. Murgatroyd, A. Rogerson, and J. F. Watters, “Irradiation growth of zirconium single crystals,” *J. Nucl. Mater.*, vol. 101, no. 1–2, pp. 28–37, Oct. 1981.
[303] J. Williams, E. Darby, and D. Minty, “Irradiation Growth of Annealed Zircaloy-2,” *Zircon. Nucl. Ind.*, pp. 376-376–18, 1984.

[304] F. Garzarolli, P. Dewes, G. Maussner, and H.-H. Basso, “Effects of High Neutron Fluences on Microstructure and Growth of Zircaloy-4,” *Zircon. Nucl. Ind. Eighth Int. Symp.*, vol. ASTM STP 1023, pp. 641–657, 1989.
[305] U. F. Kocks, C. N. Tomé, and H.-R. Wenk, *Texture and anisotropy: preferred orientations in polycrystals and their effect on materials properties*. Cambridge university press, 1998.
[306] J. L. Baron *et al.*, “Interlaboratories Tests of Textures of Zircaloy-4 Tubes. Part 1: Pole Figure Measurements and Calculation of Kearns Coefficients,” *Textures Microstruct.*, vol. 12, no. 1–3, pp. 125–140, 1990.
[307] J. E. Harbottle and F. Herbillon, “Shape and volume changes during irradiation growth of Zircaloy-2,” *J. Nucl. Mater.*, vol. 90, no. 1–3, pp. 249–255, May 1980.
[308] R. A. Holt and A. R. Causey, “Volume conservation during irradiation growth of Zr–2.5Nb,” *J. Nucl. Mater.*, vol. 335, no. 3, pp. 529–533, Dec. 2004.
[309] D. G. Franklin and R. B. Adamson, “Implications of Zircaloy creep and growth to light water reactor performance,” *J. Nucl. Mater.*, vol. 159, pp. 12–21, Oct. 1988.
[310] J.-P. Mardon, D. Charquet, and J. Senevat, “Influence of Composition and Fabrication Process on Out-of-Pile and In-Pile Properties of M5 Alloy,” *Zircon. Nucl. Ind. Twelfth Int. Symp.*, pp. 505-505–20, 2000.
[311] E. F. Ibrahim and R. A. Holt, “Anisotropy of irradiation creep and growth of zirconium alloy pressure tubes,” *J. Nucl. Mater.*, vol. 91, no. 2–3, pp. 311–321, Jul. 1980.
[312] R. A. Holt, “Microstructure dependence of irradiation creep and growth of zirconium alloys,” *J. Nucl. Mater.*, vol. 90, no. 1–3, pp. 193–204, May 1980.
[313] R. H. Zee, A. Rogerson, G. J. C. Carpenter, and J. Watters, “Effect of tin on the irradiation growth of polycrystalline zirconium,” *J. Nucl. Mater.*, vol. 120, no. 2–3, pp. 223–229, Apr. 1984.
[314] S. Buckley, “Properties of reactor materials and effects of irradiation damage,” *Butterworths Lond.*, pp. 413–416, 1962.
[315] D. Northwood, “Irradiation Growth in Zirconium and Its Alloys,” *Eff. Radiat. Struct. Mater.*, vol. ASTM STP 683, pp. 62–76, 1979.
[316] C. H. Woo and U. Gösele, “Dislocation bias in an anisotropic diffusive medium and irradiation growth,” *J. Nucl. Mater.*, vol. 119, no. 2–3, pp. 219–228, Dec. 1983.
[317] A. M. Monti, A. Sarce, N. Smetniansky-De Grande, E. J. Savino, and C. N. Tomé, “Point defects and sink strength in h.c.p. metals,” *Philos. Mag. A*, vol. 63, no. 5, pp. 925–936, May 1991.
[318] C. J. Ball, “The contribution of the intrinsic anisotropy of point defect diffusion rates to irradiation growth of zirconium,” *J. Nucl. Mater.*, vol. 101, no. 1–2, pp. 147–149, Oct. 1981.
[319] R. G. Fleck, R. A. Holt, V. Perovic, and J. Tadros, “Effects of temperature and neutron fluence on irradiation growth of Zr-2.5 wt% Nb,” *J. Nucl. Mater.*, vol. 159, pp. 75–85, Oct. 1988.
[320] D. Fainstein-Pedraza, E. J. Savino, and A. J. Pedraza, “Irradiation-growth of zirconium-base alloys,” *J. Nucl. Mater.*, vol. 73, no. 2, pp. 151–168, May 1978.
[321] S. R. MacEwen and G. J. C. Carpenter, “Calculations of irradiation growth in zirconium,” *J. Nucl. Mater.*, vol. 90, no. 1–3, pp. 108–132, May 1980.
[322] A. J. Pedraza and D. Fainstein-Pedraza, “Irradiation growth of zirconium-base alloys,” *J. Nucl. Mater.*, vol. 88, no. 2–3, pp. 236–248, Feb. 1980.

[323] E. J. Savino and C. E. Laciana, “Radiation induced creep and growth of zirconium alloys,” *J. Nucl. Mater.*, vol. 90, no. 1–3, pp. 89–107, May 1980.
[324] R. Bullough and M. H. Wood, “Mechanisms of radiation induced creep and growth,” *J. Nucl. Mater.*, vol. 90, no. 1–3, pp. 1–21, May 1980.
[325] N. Sadaoka and M. Fuse, “Effects of Microstructural Factors on Irradiation Growth in Zirconium-Niobium Alloys,” *Zircon. Nucl. Ind. Eighth Int. Symp.*, pp. 692-692–13, 1989.
[326] R. Holt, A. Causey, N. Christodoulou, M. Griffiths, E. Ho, and C. Woo, “Non-Linear Irradiation Growth of Cold-Worked Zircaloy-2,” *Zircon. Nucl. Ind. Elev. Int. Symp.*, pp. 623-623–15, 1996.
[327] C. H. Woo, “Polycrystalline effects on irradiation creep and growth in textured zirconium,” *J. Nucl. Mater.*, vol. 131, no. 2–3, pp. 105–117, Apr. 1985.
[328] S. Golubov, A. Barashev, R. Stoller, and B. Singh, “Breakthrough in understanding radiation growth of zirconium,” *Zircon. Nucl. Ind. 17th Vol.*, 2015.
[329] C. H. Woo, “Modeling irradiation growth of zirconium and its alloys,” *Radiat. Eff. Defects Solids*, vol. 144, no. 1–4, pp. 145–169, Jun. 1998.
[330] C. N. Tomé *et al.*, “Role of internal stresses in the transient of irradiation growth of Zircaloy-2,” *J. Nucl. Mater.*, vol. 227, no. 3, pp. 237–250, Jan. 1996.
[331] B. . Adams, G. S. Clevinger, and J. P. Hirth, “An upper-bound evaluation of interactive creep and growth in textured Zircaloy,” *J. Nucl. Mater.*, vol. 90, no. 1–3, pp. 75–88, May 1980.
[332] E. J. Savino and S. Harriague, “Micro-Macrostructural Mechanical Behavior of Anisotropic Zirconium Alloys Under Irradiation,” *Eff. Radiat. Mater. 12th Int. Symp. Vol. II*, pp. 667–689, Nov. 1985.
[333] C. N. Tomé, C. B. So, and C. H. Woo, “Self-consistent calculation of steady-state creep and growth in textured zirconium,” *Philos. Mag. A*, vol. 67, no. 4, pp. 917–930, Apr. 1993.
[334] P. A. Turner, C. N. Tomé, and C. H. Woo, “Self-consistent modelling of nonlinear visco-elastic polycrystals: An approximate scheme,” *Philos. Mag. A*, vol. 70, no. 4, pp. 689–711, Oct. 1994.
[335] A. Patra, C. N. Tomé, and S. I. Golubov, “Crystal plasticity modeling of irradiation growth in Zircaloy-2,” *Philos. Mag.*, vol. 97, no. 23, pp. 2018–2051, May 2017.
[336] G. Field, “Problems caused by irradiation deformation in CANDU reactors,” *J. Nucl. Mater.*, vol. 159, pp. 3–11, 1988.
[337] F. Tinti, “Uniaxial In-Reactor Creep of Zircaloy-2: Stress, Flux, and Temperature Dependence,” *Nucl. Technol.*, vol. 60, no. 1, pp. 104–113, Jan. 1983.
[338] N. Christodoulou *et al.*, “Modeling In-Reactor Deformation of Zr-2.5Nb Pressure Tubes in CANDU Power Reactors,” *Zircon. Nucl. Ind. Elev. Int. Symp.*, vol. ASTM STP 1295, pp. 518–537, 1996.
[339] A. Causey, “In—Reactor Stress Relaxation of Zirconium Alloys,” *Zircon. Nucl. Appl.*, pp. 263-263–11, 1974.
[340] S. Carassou *et al.*, “REFLET Experiment in OSIRIS: Relaxation under Flux as a Method for Determining Creep Behavior of Zircaloy Assembly Components,” *Zircon. Nucl. Ind. 16th Int. Symp.*, pp. 899–928, Jul. 2010.
[341] C. E. Coleman, A. R. Causey, and V. Fidleris, “In-reactor creep of zirconium-2.5 wt% niobium at 570 K,” *J. Nucl. Mater.*, vol. 60, no. 2, pp. 185–194, May 1976.
[342] R. F. DeAbreu *et al.*, “Temperature and Neutron Flux Dependence of In-Reactor Creep for Cold-Worked Zr-2.5Nb,” *Zircon. Nucl. Ind. 18th Int. Symp.*, pp. 938–964, Jan. 2018.

[343] L. Walters, G. A. Bickel, and M. Griffiths, “The Effects of Microstructure and Operating Conditions on Irradiation Creep of Zr-2.5Nb Pressure Tubing,” *Zircon. Nucl. Ind. 17th Vol.*, pp. 693–725, Sep. 2014.
[344] J. P. Foster, G. Pan, L. Cai, and A. R. Atwood, “Effect of Hydrogen on Irradiation Creep and Growth for ZIRLO Alloy and Zr-1.0Nb,” *Zircon. Nucl. Ind. 18th Int. Symp.*, pp. 725–747, Jan. 2018.
[345] A. Garde, P. Smerd, F. Garzarolli, and R. Manzel, “Influence of Metallurgical Condition on the In-Reactor Dimensional Changes of Zircaloy Fuel Rods,” *Zircon. Nucl. Ind.*, vol. ASTM STP 824, pp. 289–305, 1984.
[346] A. Seibold and F. Garzarolli, “Influence of composition and condition on in-PWR behavior of Zr-Sn-Nb-FeCrV alloys,” *Zircon. Nucl. Ind. Thirteen. Int. Symp. ASTM Int.*, vol. STP 1423, pp. 743–757, 2002.
[347] F. A. Nichols, “Theory of the creep of zircaloy during neutron irradiation,” *J. Nucl. Mater.*, vol. 30, no. 3, pp. 249–270, Apr. 1969.
[348] J. R. Matthews and M. W. Finnis, “Irradiation creep models — an overview,” *J. Nucl. Mater.*, vol. 159, pp. 257–285, Oct. 1988.
[349] D. Faulkner and R. McElroy, “Irradiation Creep and Growth in Zirconium During Proton Bombardment,” *Eff. Radiat. Struct. Mater.*, vol. ASTM STP 683, pp. 329–345, 1979.
[350] F. Nichols, “Mechanistic modeling of Zircaloy deformation and fracture in fuel element analysis,” *Zircon. Nucl. Ind. Seventh Int. Symp.*, vol. ASTM STP 939, pp. 5–22, 1987.
[351] S. R. MacEwen and V. Fidleris, “Irradiation creep in Zr single crystals,” *J. Nucl. Mater.*, vol. 65, pp. 250–257, Mar. 1977.
[352] F. A. Garner and D. S. Gelles, “Irradiation creep mechanisms: An experimental perspective,” *J. Nucl. Mater.*, vol. 159, pp. 286–309, Oct. 1988.
[353] S. MacEwen and V. Fidleris, “Verification of a model for in-reactor creep transients in zirconium,” *Philos. Mag.*, vol. 31, no. 5, pp. 1149–1157, 1975.
[354] M. Gaumé, P. Baldo, F. Mompiou, and F. Onimus, “In-situ observation of an irradiation creep deformation mechanism in zirconium alloys,” *Scr. Mater.*, vol. 154, pp. 87–91, 2018.
[355] F. A. Nichols, “On the mechanisms of irradiation creep in zirconium-base alloys,” *J. Nucl. Mater.*, vol. 37, no. 1, pp. 59–70, Oct. 1970.
[356] G. Martin and J. Poirier, “Considerations sur la relation entre le fluage sous irradiation et les dommages crees par l’irradiation en l’absence de contrainte,” *J. Nucl. Mater.*, vol. 39, no. 1, pp. 93–101, 1971.
[357] Mosedale, D. (1962). Influence of Irradiation on Creep. Journal of Applied Physics, 33(10), 3142-3143.
[358] Duffin, W. J., & Nichols, F. A. (1973). The effect of irradiation on diffusion controlled creep processes. Journal of Nuclear Materials, 45(4), 302-316.
[359] Kozar, R. W., Jaworski, A. W., Webb, T. W., & Smith, R. W. (2014). In situ monitored in-pile creep testing of zirconium alloys. *Journal of Nuclear Materials*, *444*(1-3), 14-22.